# CHALMERS
## UNIVERSITY OF TECHNOLOGY



*Cell model*

# Electro-Thermal modelling of LFP Prismatic cell with SOC estimation model

Master of Science thesis in Electric Power Engineering

SHRISHA BALKUR

# Electro-Thermal modelling of LFP Prismatic cell with SOC estimation model

## SHRISHA BALKUR

Department of Energy and Environment
*Division of Electric Power Engineering*
Chalmers University of Technology
Gothenburg, Sweden 2020

Electro-Thermal modelling of LFP Prismatic cell with SOC estimation model
SHRISHA BALKUR
Department of Energy and Environment
Chalmers University of Technology

# Abstract

The battery is an electrochemical device and having a model which predicts the electrical and thermal behaviour of the cell is beneficial for the development of battery systems, especially for load analysis and battery management systems. In this thesis, the electro-thermal model of the LFP prismatic cell is developed. The cell is characterized for both electrical and thermal properties by tests which can be done with simple and easily available equipment in a standard battery laboratory, making it a cost-effective method. By taking the current and the ambient temperature as inputs, the model can predict the surface temperature of the cell and the open-circuit voltage, and the state of charge ($SOC$) is determined using coulomb counting.

First, to have an electrical model, An Equivalent Electric Circuit Model (EECM) is developed. The electrical parameters of the circuit model are extracted from pulse discharge and charge tests, the extracted parameters are further optimized using the parameter estimation method. All these parameters are dependant on both the $SOC$ and the temperature. A 3-D look-up table for all these parameters is made, capturing a wide range of $SOC$ and temperature. The RMS error between the experiment and the model is found to be as low as $1.29\,\mathrm{mV}$.

Next, a new methodology to determine both the specific heat capacity and the thermal resistance of the cell without using a calorimeter is proposed. A second-order lumped parameter thermal model is used to find these two thermal properties. The values of specific heat capacity of the cell is found to be $1035.67\,\mathrm{JK^{-1}kg^{-1}}$ and through plane thermal resistance from the core to the surface of the cell is $0.79\,\mathrm{K\,W^{-1}}$. The setup for the experiment is simple, and a single experiment is sufficient to get both the parameters. Both the Joule heating and the heat generation due to change in entropy is considered for the heat generation losses in the cell. Finally, to estimate the surface temperature of the cell, a first-order lumped parameter thermal model is used.

The surface temperature and the open-circuit voltage of the model show good agreement with that of the experiment when validated with NEDC and WLTC drive cycles. State of Charge estimation model is developed using the Extended Kalman filter(EKF) and the Unscented Kalman filter(UKF) to demonstrate the model's application in the battery management system.

Keywords: Battery model, LFP, EECM/ECM, parameter estimation, Lumped Parameter model, specific heat capacity, thermal resistance, Entropic coefficient, SOC estimation model, Drive cycle.

# Acknowledgements

# Contents

# Contents

# 1

# Introduction

In recent decades the focus has been to reduce the $CO_2$ emissions to the atmosphere and to reduce global warming. Around 30% of the total EU's $CO_2$ emission is from transportation, and road transport alone contributes with 72% of it [1]. Lorries, buses, and coaches contribute with around 6% of the emissions [2] and the regulations setting $CO_2$ emission standards for heavy-duty vehicles came into force on 14 August 2019 [3]. By 2050, the EU has the goal to reduce emissions from transportation by 60% compared to 1990 [4]. Hence, adaptation of the battery electric vehicle (BEV) and the plug-in hybrid vehicle (PHEV) are on the rise [5] and is a popular choice for automotive industry and consumers.

## 1.1 Background

Conventionally, a lead-acid battery is used for starting, lighting and ignition in vehicles, this could soon be replaced in the future by Li-ion technologies [6]. In recent decades vast improvement in battery technology has led to the Li-ion battery technology in traction applications because of its higher energy density, low self-discharge and longer life span [7, 8, 9].

Battery, electric control, power electronic inverters, and electric motors are the major sub-systems of an electric power train [10]. Hence, the need for a battery model for simulation purposes serves as an important tool for the development of battery-powered systems [11] to optimise the design at the system level, for load analysis, for better algorithm development for estimating State of charge(SOC), State of Health(SOH) and temperature for better thermal management.

## 1.2 Previous work

In [12, 13], mathematical models based on chemical reactions are considered to be poor in practical application as they are more complex with many parameters [10]. The data-driven approaches such as the Neural network-based model [14, 15] can model high non-linearities of Li-ion batteries with a large set of training data and is computationally costly [10]. The equivalent circuit-based models [16, 17, 18, 19, 20]

are used widely in online applications as they do not consider the chemical composition of the battery and work with simple electrical components which are computationally less costly compared to the two methods mentioned before [10].

In [21, 22, 23], the thermal model is coupled with an electrochemical model of the battery. Three dimension based thermal models are developed to investigate the abuse conditions [24], and to predict heat generation during charging and discharging of the cell for better thermal management [25], etc. Many methodologies propose to estimate the internal temperature of the cell using various forms of Kalman filtering techniques [26, 27], but in all of them, the thermal properties of the cell such as specific heat capacity and thermal resistance of the cell need to be determined. They are not usually available from manufacturer. In [28], a method is proposed which does not require deconstruction of the cell or expensive calorie-meters to determine specific heat capacity, instead it can be determined with the help of most commonly available lab equipment. Determination of the entropic coefficient of the battery with a simple experimental setup, and the method has been proposed by [29].

A direct measurement technique of estimating SOC by measuring terminal voltage, impedance and impedance spectroscopy method is proposed by [30, 31]. The coulomb counting method [32] is a form of bookkeeping method, which is one of the simple methods to estimate SOC, but it is found to accumulate small errors as it is dependant on initial SOC. There are many methodologies for indirect measurement for SOC estimation such as the neural network method [33], support vector method [34], fuzzy logic [35] and various forms of Kalman filters [36, 37].

## 1.3   Purpose

The goal of this thesis is to develop the high fidelity cell model of the LFP prismatic cell which incorporates the electrical and thermal behaviour of the cell. In order to achieve this, equivalent electrical circuit model and thermal model is to be developed and need to be validated with the drive cycle. One application of the model is also to be demonstrated.

## 1.4   Scope

As discussed in earlier sections, the Matlab-Simulink environment would be used for the modeling of the cell.

- The parameters for the Equivalent electrical circuit model (EECM) are found according to [38] and later optimized further according to [39]. The parameters are extracted for both charging and discharging circuit models from pulse charge and discharge test. The electrical model is designed to estimate the terminal voltage of the cell from $10\,°C$ to $40\,°C$.
- In the thermal model, irreversible and reversible thermal effects are taken into account by the model. Radiation effects are ignored.

- A first-order lumped parameter model is used to do thermal modelling. A new methodology is proposed to find the specific heat capacity $C_{p_{cell}}$ and thermal resistance $R_{cell}$. A look-up table of entropy coeffecients $\frac{dU}{dT}$ is found using potentiometric test [29].
- In the SOC estimation model, Extended Kalman filter and Unscented Kalman filtering techniques would be investigated to model.

## 1.5 Outline

This report is structured in the following chapters:
- **Theory**: Relevant theoretical background for the case setup and analysis used in the work will be presented.
- **Methods**: This chapter focuses to explain the experimental setup, relevant steps and methodologies implemented to model the battery.
- **Results**: Focuses on the results of the tests and the post processes mentioned in case setup.
- **Discussion**: A brief discussion on the model and its uncertainties, and also to discuss the sustainability aspects.
- **Conclusions**: A final commentary on the model and future work will be proposed.

# 2

# Theory

In this chapter, the theoretical concepts used in this thesis will be discussed. This section will help in understanding the further chapters. It will also discuss the common terminologies which will be used in further chapters.

## 2.1  Basics of Lithium-ion cell

The electrochemical cell is the smallest unit of the battery. The materials inside the cell influence all the performance characteristics of the cell. But, some general principles govern all the cells irrespective of its materials used [40]. The electrochemical cell is a rechargeable cell, that is it can convert chemical energy to electrical energy and vice versa. The cell's components consist of anode, cathode, separator, electrolyte, current collectors and the casing for the cell. In general, the anode is the negative electrode and cathode is the positive electrode [40].

The electrochemical oxidation and reduction known as *Redox* reactions are the chemical reactions that take place during the charging and discharging of the cell. The **electrodes** for rechargeable cells are of insertion type. The *redox* reactions take place both at the surface of the electrode and at the bulk of the electrode. The main task of the **electrolyte** is to conduct the lithium ions and not electrons. The conductivity must be fast and should not limit the *redox* reactions. The **separator** is placed between two electrodes to avoid unintentional short circuit of the cell. Its main purpose is to give a high ionic conductivity in the electrolyte in its pores and provide good insulation properties. Mechanical stability, strength, chemical stability, wetting of electrolyte and porosity are also the desired properties of the separator [40]. During the charging or discharging process, the electrons are transferred in an external circuit which is what an user is mainly interested in. For this purpose, **current collectors** in the form of foils or grids are used for both the electrodes. These current collectors display high electrical conductivity and should not take part in *redox* reactions taking place inside the cell. These are usually Copper or Aluminium. The current collectors provide mechanical strength and act as a heat sink to remove the heat generated inside the cell [40]. The electrochemical cell is placed in a **casing** to provide further mechanical strength and to avoid evaporation of the electrolyte.

It is important to note that in a typical battery pack several individual cells are arranged either in series, parallel or in the combination of both. The cells are said

to be connected in series if the positive terminal of one cell is connected to the negative terminal of another cell. If the positive terminal of the cell is connected to the positive terminal of the second cell, and the negative terminal of the cell is connected to the negative terminal of the second cell, then it is said to be in parallel connection. The individual battery cells, therefore, will be referred to as cell from here on wards. In this thesis all the analysis is done on the cell and not the battery level.

### 2.1.1 State of Charge ($SOC$)

It is the representation for the present capacity of the battery with respect to its maximum capacity [41]. It shows how much capacity of the battery that is remaining, it is generally shown in percentage. Many cell parameters and behaviours are dependent on $SOC$. The cell capacity is expressed as $Amp-hour$ or A h units. The effects of the temperature, ageing and discharge current rates on the capacity of the battery will not be considered in this thesis.

### 2.1.2 Open circuit voltage($OCV$)

It is the difference in potential between the two terminals when no load is connected. There is a non-linear relationship of open-circuit voltage with respect to $SOC$. The terminal voltage of the cell decreases non-linearly as the $SOC$ decreases. It is also affected by the load, temperature and ageing. Since the cell investigated in this thesis is new, thus the effect of ageing is not considered.

**Cell voltage under load**

The terminal voltage of the cell under operation differs from $OCV$. During the discharging of the cell, due to *redox* reactions, the cell converts the chemical energy to electrical energy. Simultaneously, the cell voltage decreases below $OCV$. This is due to the losses in the cell. There are various types of polarisation or overpotential inside the cell when current flows through it. It is generally classified as the activation overpotential, concentration overpotential and ohmic losses[40].

- *Activation polarization or over-potential* is referred to the extra energy required by the reactant species to start the chemical reaction to overcome the barrier potential at the electrode and solution interface. It is the overpotential required for the charge-transfer reactions at both cathode and anode [42], and loss due to the charge transfer is given as $\eta_{ct}$ [40].


- *Concentration polarization or overpotential* is due to the difference in the concentration of charged species between the electrode surface and the bulk of the electrolyte. It is mainly due to ionic conductivity and mass transport properties of the electrolyte. The losses due to concentration polarization is given as $\eta_c$ [40]. Ionic conductivity is also a function of temperature. As the temperature increases, ionic conductivity increases and losses due to conductivity decreases.

- *Resistive losses* is the sum of various resistances due to the current collector, electrode, separator, ionic resistance of the electrolyte, the interface of current collector/electrode, electrode/electrolyte, electrolyte/separator. The losses due to these ohmic resistances are dependant on the applied current.

The variation of cell voltage with respect to current can be shown as in figure 2.1. The above effects can be captured by an Equivalent Electrical Circuit Model(EECM), and it is explained in section 2.3.
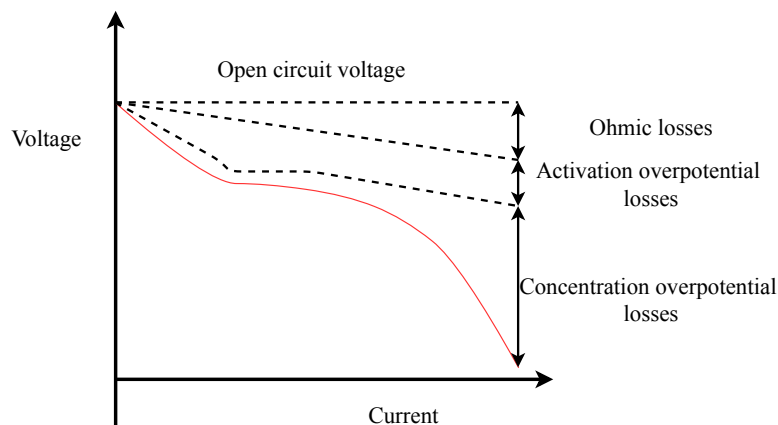


**Figure 2.1:** Voltage of the cell with respect to the current [40]

**Hysteresis**

During the charging and discharging operations of the cell, all electrochemical processes are delayed and have different time scales. This is due to the external load current and is observed as the voltage difference or voltage hysteresis $\Delta V$.

**Effect of different current rates on the cell voltage**

**C-rate** is related to the value of discharge current in its normalised form against its battery capacity [41]. For example, if the cell is having a capacity of $10\,A\,h$, then the value of 1C-rate is $10\,A$. This value of the discharge current can discharge the cell completely in one hour. At higher C-rate, the cell reaches the cut-off voltage faster and the capacity utilisation of the cell decreases, as shown in figure 2.2. At higher C-rates, ohmic losses are higher and thus the terminal voltage of the cell decreases much faster. This is also one of the main reasons for the increase in temperature of the cell, which will be discussed in further sections.
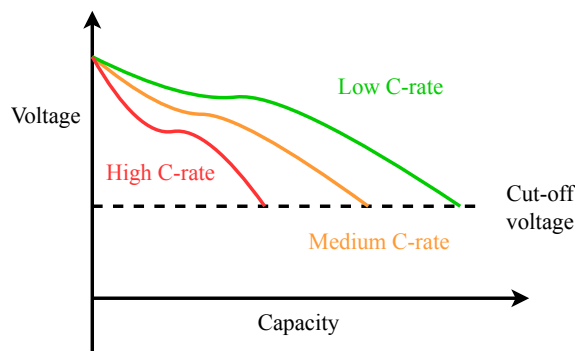
**Figure 2.2:** Effect on cell voltage and capacity due to different C-rates [40]

### 2.1.3 Materials of Lithium-ion cell

The lithium ions during the charging of the cell are extracted from the positive electrode(or cathode) and inserted to the negative electrode(or anode) via the organic solvents called the electrolyte. The electrons flow from cathode to anode through the external circuit. During the discharging of the cell, the reverse of the same process is followed. The performance of the lithium-ion cells is dependant on the material properties and how well it can extract and insert lithium ions [40].

**Positive electrode**

In a *Li-Ion* cell, for better cycling of *Li* ions, the positive electrode must have Lithium. The material chosen should be chemically stable and non-toxic. There are few positive electrode materials which satisfy these criteria example: LMO ($LiMn_2O_4$), NMC ($LiNi_{0.8}Co_{0.15}Al_{0.05}O_2$), NCA ($LiNi_{0.33}M_{0.33}C_{0.33}O_2$),and LFP ($LiFePO_4$). All these electrode materials have porous structures. Depending on the performance needs, these electrodes must be chosen. None of the different cathode materials exhibits all the desired requirements. According to [43], **LFP** score high on cost, specific power, safety, performance and lifespan. This is the cathode chemistry used in this thesis.

**Negative electrode**

The two types of mainly used active materials used for negative electrodes are metallic lithium and insertion type. **Graphite** is the most widely used negative electrode and it is an insertion type. It is mainly used due to its ability to extract and insert lithium ions and it has a lower potential of 0.1 V [40].

### 2.1.4 Different types of cell formats

In automotive applications, the cell design used are mainly of three formats and they are *cylindrical, prismatic and pouch*, as shown in figure 2.3. The diameter of the **cyclindrical cells** indicates the capacity of the cell. The larger the diameter

the higher is the capacity of the cell. It has a metallic casing with a jelly roll inside. A jelly roll is having different layers consisting of cathode, anode, separator and electrolyte. A **Prismatic cell** also has a metallic casing generally made up of aluminium, produced in either of the two ways. It either has wound or stacked layers inside the casing. Z-folded layered arrangement can also be used. **Pouch cells** are also referred to as coffee bag cells [40] because of its flexible and soft casing. The polymer laminated aluminium foil is used for the packaging.



Cylindrical          Prismatic                          Pouch
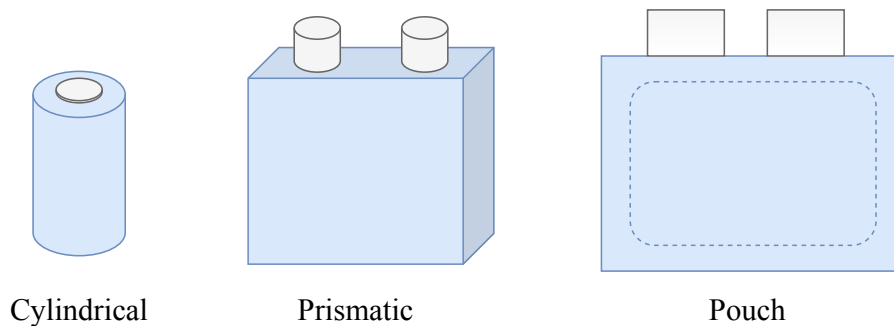
**Figure 2.3:** Different formats of the cell

There are both advantages and limitations of using different cell designs. Cylindrical cells are easy to construct, provides good safety and robustness but need good cooling options as its core heats up higher compared to its shell. Due to the construction of the prismatic cell, it offers good safety, robustness, ease in manufacturing battery packs and also easier thermal management solutions. Pouch cell offers higher energy density since its weight is reduced due to the absence of a metallic casing. But needs better thermal management when compared to the other two cell designs [40].

## 2.2 Temperature effects on the cell

The temperature is an important factor which affects the performance of the battery. Temperature affects both the capacity and internal resistance of the cell. The initiation of dendrite formation increases when the cell is charged at $-10\,°C$ to $0\,°C$ [44]. Dendrites formed at the anode can pierce or block the separator and this might lead to the internal short circuit of the cell. The conductivity of the electrolyte is lower at low temperature and thus increases the internal resistance. This causes the cell to reach the cut off voltage faster and thus reducing the capacity. At higher temperatures, the rate of chemical reactions and side reactions increases. Very high temperature causes the decomposition of the materials and exhibits the abuse conditions [40]. Therefore, for better performance of the cell, the temperature should be neither very low nor very high. Thus, it is preferable to keep the operating temperature at $20\,°C$ - $40\,°C$ [40].

### 2.2.1 Heat generation inside the cell

The electrochemical reactions and joule heating are the main reasons for heat generation inside the cell. Total heat generation can be written as the sum of both irreversible and reversible heat generation. Where irreversible heat generation is due to joule heating and it is an exothermic reaction. Reversible heat generation can be both the exothermic or endothermic reaction. It is due to change in entropic coefficient and the direction of the current. A simplified form for the heat generation is given by [45] and it is given as,

$$\dot{Q} = \dot{Q_{irr}} + \dot{Q_{rev}} \tag{2.1}$$

$$\dot{Q} = I|(V - OCV)| + IT\frac{dU}{dT} \tag{2.2}$$

## 2.3 Equivalent circuit model

The equivalent circuit-based models are given in [16, 17, 18, 19, 20]. Conventionally, a simple Thevenin based model with a DC voltage source and a resistor in series to represent the internal resistance of the cell is used for quick calculations. It is called a $R0$ model. This model is simple and cannot represent the dynamic characteristics such as different overpotentials due to charge transfer and diffusion of the cell. For this purpose, the multiple $RC$ links in series are used, as shown in figure 2.4. The number of $RC$ links are selected based on how good the circuit can represent the dynamic behaviour of the cell and it is explained in section 3.3.3.1. All the circuit elements are dependant on both $SOC$ and the temperature $T$ of the cell.
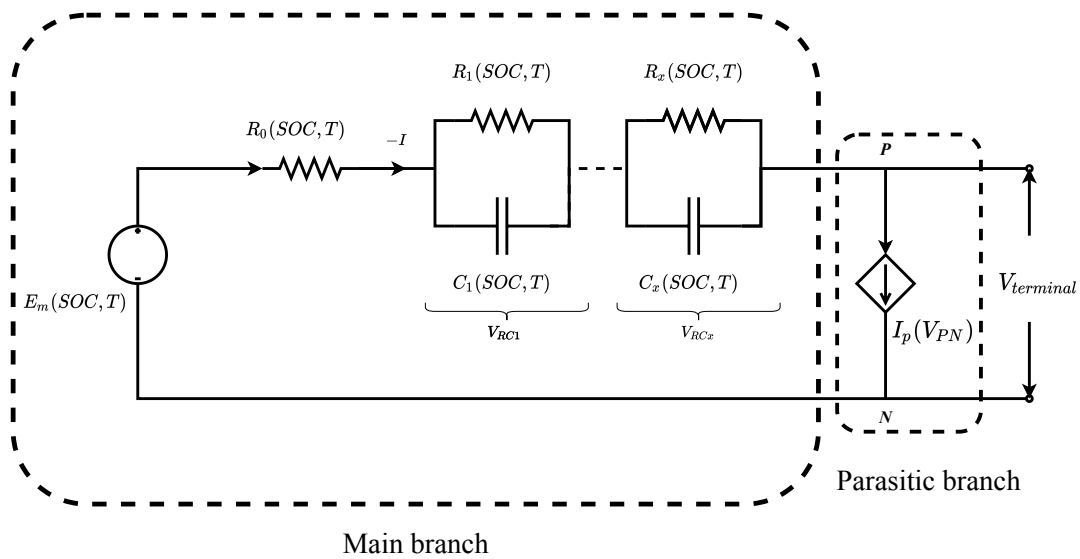


**Figure 2.4:** Equivalent electrical circuit model of the cell [19][20]. The parasitic branch is ignored for the modelling.

The parasitic branch of the EECM is ignored in this thesis as it is often ignored while modelling $Li - ion$ cells as they are considered to have low self-discharge and high Coulombic efficiency [39] and this effect is mainly observed in lead acid batteries. The parasitic branches were conventionally modelled to represent the parasitic reactions which draw current that does not participate in reversible reactions [19]. The parasitic current $I_p$ is dependant on the voltage across the positive $P$ and negative $N$ terminal of the cell $V_{PN}$.

## 2.4 Lumped parameter model

A lumped parameter network is a simplified representation to describe the heat transfer in an electrical system using simple circuit elements. Simple analogies for the thermal and electrical elements exist as shown in table 2.1 and it is given in many heat transfer textbooks. In [46], the procedure to build an electrical network to build thermal system is presented.

**Table 2.1:** Analogy between thermal and electrical quantities.

| Thermal parameter | Electrical parameter |
|---|---|
| $\dot{Q}$ - Rate of heat(W) | $I$ - Current(A) |
| $T$ - Temperature (K) | $V$ - Voltage(V) |
| $mC_p$ - Heat capacity($\mathrm{J\,K^{-1}}$) | $C$ - Capacitor(F) |
| $R_t$ - Thermal resistance($\mathrm{K\,W^{-1}}$) | $R$ - Resistor($\Omega$) |

An example, shown in figure 2.5 is used to illustrate the method to build the circuit. In this example, a heating element heats three materials *A, B and C*. A perfect insulator insulates the sides of the three materials. Two assumptions are made. That no heat escapes from the insulation to the ambient, and heat flows in only one direction. Heat generation distribution is assumed to be uniform.

Heat transfers from one side of the material $A$, it flows through to material $B$ and $C$. Initially, a fraction of the heat is stored temporarily due to the mass of the material and a fraction of heat escapes from material $C$ to the ambient, this is identified as the **transient region**. After a long time, all the heat is transferred either by conduction or convection out to the air and is identified as the **steady-state region**.

Each of the material have different thermal properties and has its own mass (kg). The product of the material's mass and specific heat capacities gives the heat capacities ($\mathrm{J\,K^{-1}}$) for the three materials $C_A, C_B$ and $C_C$ respectively. The temperature at the core of the respective materials is represented as $T_A, T_B$ and $T_C$.
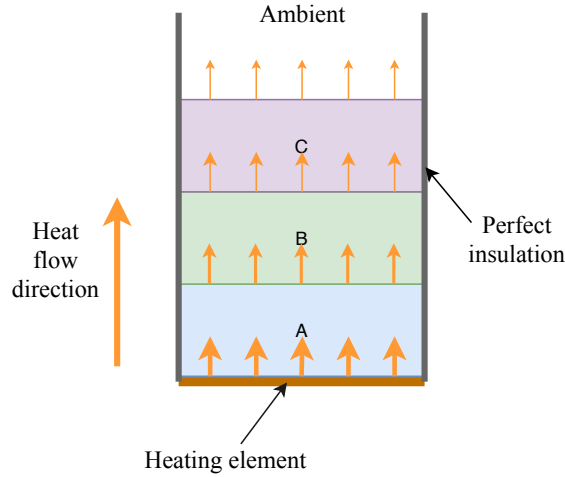
**Figure 2.5:** illustration for thermal modelling

The rate of heat supplied to the material $A$ is represented as $P$. The radiation phenomenon is not considered in this thesis. The heat transfer coefficient due to the conduction and convection are given as $h_{cond}$ and $h_{conv}$. The thermal resistance due to conduction and convection is given as,

$$R_{conduction} = \frac{L}{h_{cond}A} \tag{2.3}$$

$$R_{convection} = \frac{1}{h_{cond}A} \tag{2.4}$$

where, $L$ and $A$ are the thickness and cross-sectional area of the material. The electrical circuit representing the heat transfer by using the circuit elements as described in table 2.1 is given in figure 2.6. $R_A$, $R_B$ and $R_C$ are the thermal resistance due to the conduction heat transfer coefficient and $R_{air}$ is due to the convection heat transfer coefficient.
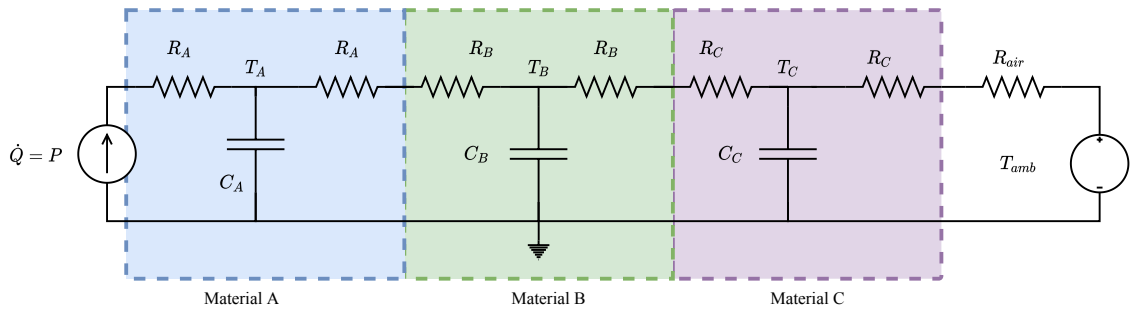


**Figure 2.6:** Thermal circuit model for figure 2.5.

The heat rate flow $P$ is represented as the current source. During the transient region the heat is partly stored by $C_A$ at $T_A$ and the part of it flows through $R_A$ to the material $B$. Similar temporary heat storage and heat transfer occurs at material $B$ and $C$ before transferring heat to the ambient which is modelled as the DC voltage source. At steady state operations the effect of $C_A$, $C_B$ and $C_C$ are minimal and can be ignored. All the heat generated is transferred to the ambient. In this manner, the

electrical circuit can be made for representing heat transfer. This type of thermal circuit modelling is called Cauer model. In this thesis, the lumped parameter model is used to estimate the surface temperature of the cell.

## 2.5 Curve fitting

This section is there to explain the main principle behind curve fitting and it is done with the help of Matlab Curve fitting toolbox [47]. The curve fitting involves finding the curve or a line which best fits the observed experimental data. Linear and non-linear least-square fitting is used in this thesis to fit the experimental curve. In both of these methods, the sum of the squares of the error between the experimental curve $y_{curve}$ and the model curve $y_{model}$ is minimised to find the best fit by finding the optimal value of the parameters.

### 2.5.1 Linear least square method

The data in the $x$ axis is considered to be the independent variable and the $y$ axis of the graph is the dependant variable. The linear regression is valid when the linear relationship between $x$ and $y$ is present. This method is non-recursive, simple and the result returns the slope and the intercept. The slope and intercept are the parameters of interest [48]. The objective function to be minimised is given as,

$$J = \sum_{x=1}^{m} \left[ y_{curve}(x) - y_{model}(x) \right]^2 \tag{2.5}$$

Since the errors are squared, linear regression is prone to the outliers in the data which are far away from the regressed line and are not statistically optimal.

### 2.5.2 Non-linear least square methods

This method is applicable for obtaining the non-linear models. The '$m$'experimentally observed data points $(x_1, y_1), (x_2, y_2), ..., (x_m, y_m)$ are dependant on the $n$ model parameters. It gives the model function as $y = f(x, \beta)$ where, $\beta$ is the collection of the model parameters. Thus the objective function to be minimized is given as,

$$J = \sum_{x=1}^{m} \left[ y_{curve}(x) - y_{model}(x, \beta) \right]^2 \tag{2.6}$$

This method is recursive, unlike in the linear least square method. The optimal value of the model parameters cannot be found in a single step [48]. It needs the initial values, the solver updates the initial values of all the parameters such that it gives the best fit. Lower and upper bounds are specified for all the parameters that the physical meaning of the parameters remains intact. By using robust-nonlinear regression, the effect of the outliers can be minimised [48].

## 2.6 Observer based estimation models

In any system, not all quantities are measurable or observable. This needs to be achieved indirectly, and in the control system, the unknown states can be estimated based on the observed inputs $u$ and the outputs $y$ of the system with the help of an observer [49]. For this application, the Kalman filter is widely used.

### State space form

The system can be described in the state space form. The system having $p$ inputs and $q$ outputs can be represented in the form,

$$x(k+1) = Ax(k) + Bu(k) + Nv_1(k) \tag{2.7}$$

$$y(k) = Cx(k) + Du(k) + v_2(k) \tag{2.8}$$

where,
$x(k)$ is the **state vector** having the dimensions $n \times 1$
$A$ is the **system matrix** having the dimensions $n \times n$
$B$ is the **input matrix** having the dimensions $n \times p$
$u(k)$ are the **inputs** having dimensions $p \times 1$
$C$ is the **output matrix** having the dimensions $q \times n$ and,
$N$ is the **disturbance matrix** having the dimensions $n \times r$
$D$ is the **feed forward** matrix having the dimensions $q \times p$. It is normally a zero matrix if the system does not have a direct feedback and whereas, (2.7) is called as the **state equation or process equation**, and (2.8) is called as the **measurement equation**.

It is common to have noise in the sensors and it is assumed that the process noise $v_1$ ($r \times 1$) and measurement noise $v_2$ are 'white noise', following the Gaussian distribution having zero mean and variances $P$ and $Q$ respectively. This noise propagates through the system and it is considered as the inputs to the system. The intensities of process and measurement noise are represented as $R_1$ and $R_2$ respectively. Its cross-spectrum noise between $R_1(n \times 1)$ and $R_2(q \times 1)$ is given as $R_{12}$. Hence the noise covariance matrix is given as,

$$R = \begin{bmatrix} R_1 & R_{12} \\ R_{12}^T & R_2 \end{bmatrix} \tag{2.9}$$

The state equation for the estimated states $\widehat{x}$ is given as,

$$\widehat{x(k+1)} = A\hat{x}(k) + Bu(k) + K[y(k) - \underbrace{C\widehat{x(k)} - Du(k)}_{\widehat{y(k)}}] \tag{2.10}$$

and, the main goal of the observer is to correct the estimated states $x(k+1)$ of the next time instant, such that the error between the actual output $y(k)$ and the estimated output $\widehat{y(k)}$ is minimised, by finding the correct value of the Kalman gain

$K$. This can be implemented to the real-time systems and it is a recursive process.

In this algorithm, there are two main steps. In the first step, the predicted values of the states along with their uncertainties are computed, using the present input, and this step is called as **prediction step**. In the next step, the measured output of the next time instant is considered to correct the predicted state variables with the calculated gain $K$. The higher weights are biased to the estimated variables with higher certainty and this is called as **update step**.

The Kalman filter is applicable for the linear systems, where the output and the inputs have a linear relationship. Unfortunately, the behaviour of the cell is non-linear. One of the simpler ways to solve this is to linearise the non-linearity with the help of first-order Taylor series. This is the extension of the Kalman filter called **Extended Kalman Filter**($EKF$) and it is mainly used for partly non-linear systems. Another non-linear based Kalman filter used in this thesis is **Unscented Kalman filter**($UKF$), which uses the unscented transform to select the sigma points around the mean of the Gaussian random variable (GRV) $x$, and gives the weights to these sigma points to determine the correct values of the states by minimising the error between the measured output $y(k)$ and the estimated output $\widehat{y(k)}$ [50][51].

## 2.7   Vehicle mechanics

A Battery Electric Vehicle (BEV) is powered by batteries. Electrical energy is converted to mechanical energy by electric motors. Power electronic converters convert DC from batteries to 3 phase AC to give as input to the motors. $F_t$ is the traction force needed for the propulsion of the vehicle. $F_t$ experiences resistance, mainly due to losses from aerodynamic friction $F_a$, rolling friction $F_r$ and gradient $F_g$ [52]. Other disturbances $F_d$, such as breaking will be ignored in all further analysis.

The longitudinal dynamics of the vehicle, of mass $m_{veh}$, moving with the velocity of $v$ as shown in figure 2.7 is represented as

$$m_{veh}\frac{dv}{dt} = F_t - (F_a + F_r + F_g) \tag{2.11}$$

where, the tractive power is given as

$$P_t = F_t v \tag{2.12}$$

$F_a$ is caused by friction due to the viscous air surrounding the vehicle. It is the air resistance force experienced by the vehicle due to its geometry and speed. The aerodynamic frictional force $F_a$ is simplified and is dependant on the frontal area of the vehicle, air density $\rho$, co-efficient of drag $c_d$, and relative speed of the vehicle $v$. It is given as

$$F_a = \frac{1}{2}\rho c_d A_f v^2 \tag{2.13}$$
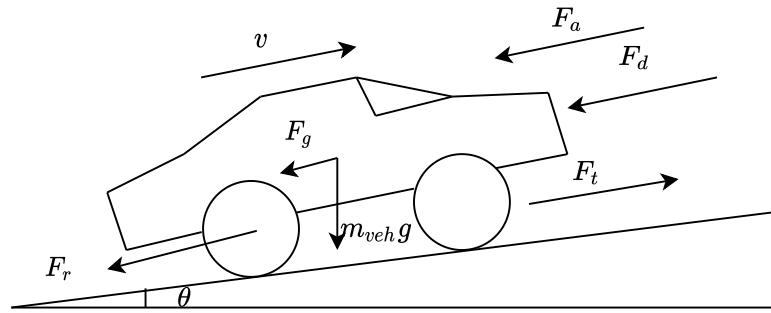
**Figure 2.7:** Equivalent electrical circuit model of the cell [52]

Rolling friction is the resistive force acting against the motion of the wheel. It mainly depends on the mass of the vehicle $m_{veh}$, acceleration due to gravity $g$, and the coefficient of rolling friction $c_r$. The coefficient of rolling friction $c_r$ is dependant on vehicle speed and tyre pressure. $c_r$ is proportional to $1/\sqrt{p}$, where $p$ is the pressure of the tyre. The operating speed of the vehicle and effects due to tyre pressure will be ignored for simplification. $F_r$ is calculated as

$$F_r = c_r m_{veh} g \tag{2.14}$$

In order to maintain the same speed of the vehicle on the flat road as compared to inclination or declination, the requirement of tractive force would be different. Vehicle experiences the resistance due to its mass $m_{veh}$, acceleration due to gravity $g$, and angle of inclination or declination $\theta$. This frictional force is called frictional force due to gradient and is given as,

$$F_g = m_v g sin(\theta) \tag{2.15}$$

# 3

# Case setup

In this chapter, experiment setup, implementation and methods used in equivalent circuit modelling, thermal modelling, and state of charge estimation are presented.

## 3.1 Specification of LFP-cell

The cell selected for this project is a LFP prismatic cell purchased from GWL POWER. The cell is rated to provide high current continuous discharge up to 3C and 1C maximum continuous charging current. It has a flat voltage area (3.10 V to 3.30 V). The specification of the cell, important for the model, is mentioned in table 3.1.

**Table 3.1:** Specification of the cell ZG-LFP020AH

| Parameter | Value |
|---|---|
| Nominal capacity | 20 A h |
| Nominal voltage | 3.2 V |
| Maximum voltage | 3.8 V |
| Minimum voltage | 2.6 V |
| Operating voltage | 2.8 V to 3.65 V |
| Maximum discharge current | 60 A (3C) |
| Maximum charging current | 20 A(1C) |
| Operating temperature (charging) | 0 to 45 °C |
| Operating temperature (discharging) | -25 to 55 °C |
| Dimensions (WxLxH) | 71 mm x 178 mm x28 mm |

## 3.2 Experimental setup

In all the tests, 4 physical quantities are measured and recorded, these are voltage, current, temperature and time. Depending on the experiment, the cell is charged or discharged in a sequence.

For these tests, a jig is manufactured using a 3D printer using PLA as the material as show in figure 3.1. The jig has a base and a separator to create separation between the two tabs of the cell to avoid unintentional short circuit between the terminals. The cell is placed in the jig, and to avoid movement of the cell in lateral

direction a brown cardboard cut in the shape of the cell is fixed at the other end of the jig.

Power cables are connected to the terminals, voltage sensors are connected to the terminals via 'crocodile clips'and a temperature sensor is fixed on the surface of the cell with the help of Kapton tape. All these wires are part of a harness which is connected to the PEC battery tester[1]. Two K-type thermocouples are used for sensing temperature. One sensor is connected to the positive terminal for sensing terminal temperature and another one for sensing the ambient temperature. It is integrated externally using THC modules which communicate with the PEC battery testing equipment using CAN communication protocol. The sequence for the test is programmed, and all the measurement from the sensors are recorded. In order to prevent over-discharging and overcharging of the cell, voltage limits $V_{min} = 2.8\,\mathrm{V}$ and $V_{max} = 3.8\,\mathrm{V}$ are given in the program.
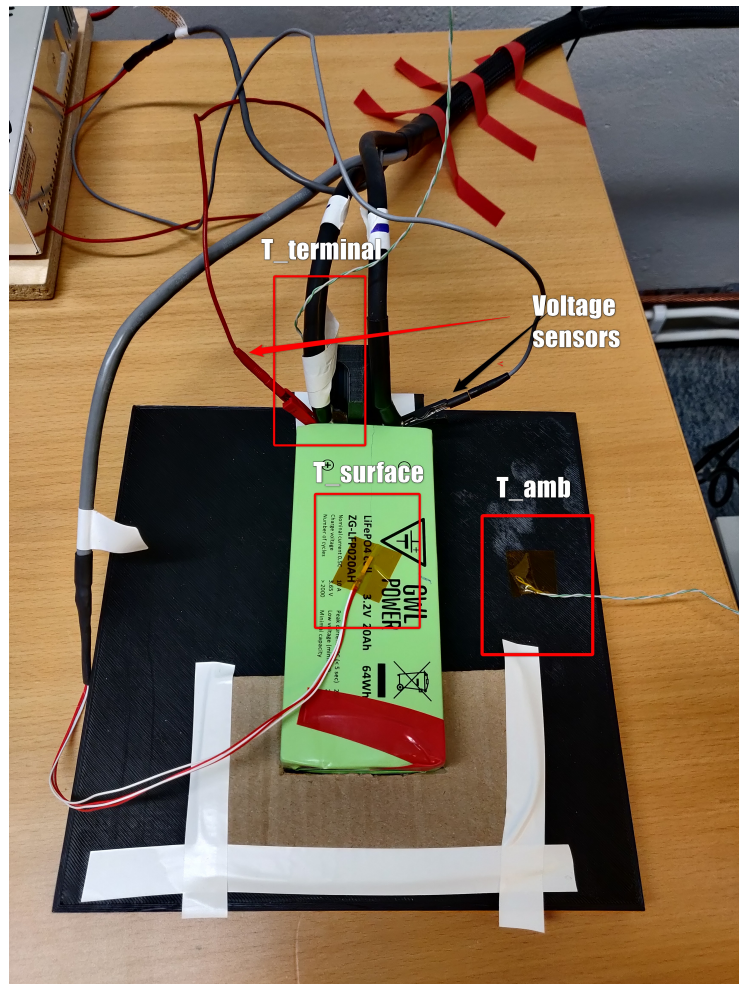


**Figure 3.1:** Test setup placed at room temperature

---

[1]PEC is a company which manufactures HIL based battery testers.

## 3.3 Equivalent Electrical Circuit Modelling (EECM)

In this section, the test procedure and the methods required for modelling are explained. The overview of the steps needed to parameterize for EECM is shown in figure 3.2. In further subsections, all the mentioned steps in the flowchart are explained in detail.
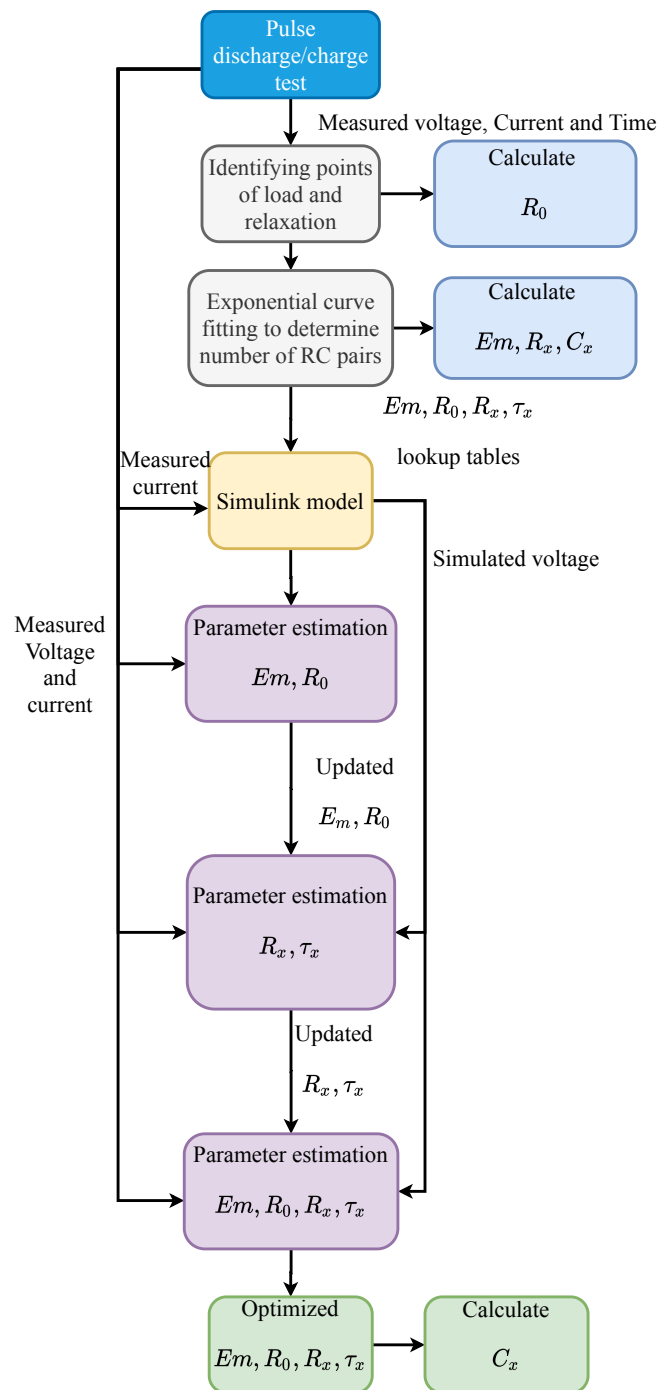


**Figure 3.2:** Flowchart for modelling EECM.

### 3.3.1  Pulse discharge - charge test

In this test, discharge and charge current pulses with defined width and magnitude are applied to the cell at constant ambient temperature conditions. The main aim of this test is to find the values of $Em$, $R_0$, $R_x$, and $C_x$ (in figure 2.4) for the EECM with respect to SOC. Later, 3-D Look-up tables for all the circuit parameters are made with respect to temperature and SOC.

The width of the current pulses are decided based on $1C$ discharge and charge voltage v/s SOC curves of the cell. If the change in voltage is steep, a smaller pulse width is chosen (this is observed at high and low SOC levels). If the change in voltage is almost flat (middle SOC levels) a larger pulse width can be chosen to save time during the test.

All the circuit parameters are dependant on SOC and temperature [53]. The experiment is done at a constant ambient temperature to remove the effects due to variations in temperature. The test is repeated at 4 different temperatures to consider the effects of operating temperature. The test is repeated for $10\,^{\circ}\text{C}$, room temperature, $30\,^{\circ}\text{C}$ and $40\,^{\circ}\text{C}$. The same experiment setup as mentioned in figure 3.1 inside a temperature chamber to maintain ambient temperature is used. Voltage, current, ambient temperature, the surface temperature of the cell and time are recorded.

### 3.3.2  Identifying the points of load and relaxation

The first step in the parameterization is to identify the points of load and relaxation on the voltage measurement for a discharge pulse as shown in figure 3.3 and for a charge pulse in figure 3.4.

- The points in the voltage response when the current goes to $-20\,\text{A}(20\,\text{A}$ for the charging pulse) from $0\,\text{A}$ or when the current goes from $-20\,\text{A}$ to $0\,\text{A}$ are identified as points of load. Alternatively, it marks when the discharging load current (or charging current) is applied.
- When the current goes from $0\,\text{A}$ to $-20\,\text{A}$ ($20\,\text{A}$ for charging pulse) or goes from $-20\,\text{A}(20\,\text{A}$ for the charging pulse) to $0\,\text{A}$, the voltage at these points are identified as points of relaxation. It can also be understood as when the discharging load current (or charging current) is not applied.
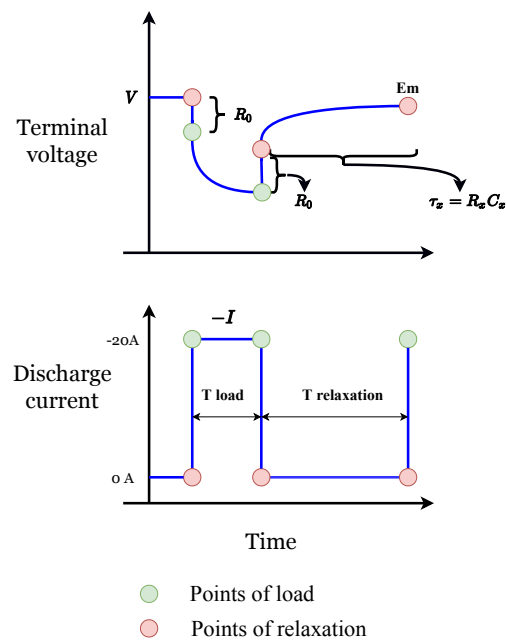
**Figure 3.3:** Points of load and points of relaxation identified on voltage curve needed for parameterization for pulse discharge test
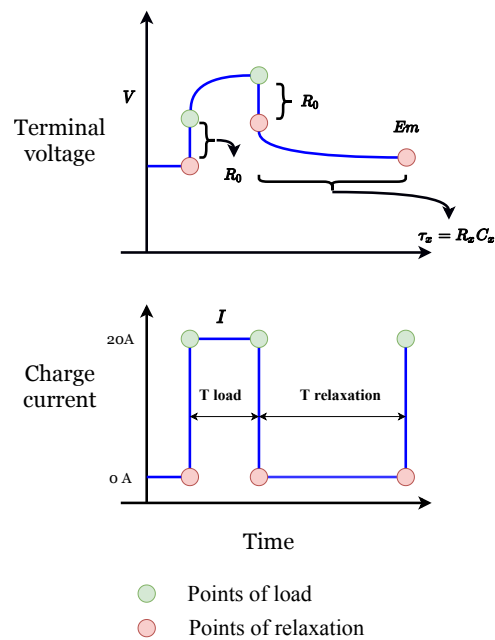


**Figure 3.4:** Points of load and points of relaxation identified on voltage curve needed for parameterization for pulse charge test

Identifying these points is critical, as it helps in the calculation of all the circuit parameters needed for the equivalent electrical circuit model.

### 3.3.3   Calculation of $Em$, $R_0$, $R_x$ and $C_x$ for initialisation

After identifying the points of load and relaxation on voltage response, the parameters required for the EECM from the voltage response curve (as shown in figures 3.3 and 3.4) can be calculated.

#### 3.3.3.1   Selection of RC pairs

Before the extraction of $R_x$ and $C_x$, it is important to select the number of RC pairs required for the model. The extraction of these parameters is done on the voltage response curve during the relaxation period as the SOC is constant when compared to the period during the discharge load current (or charging current) is applied [38].

During the period of relaxation, the voltage response corresponds to exponentially rising curve for pulse discharge test or exponentially falling curve for pulse charge test. A non-linear least square method is used to fit the measurement with an exponential curve using

$$E_{curve}(SOC) = a_0 - \sum_{i=1}^{n} a(i)e^{-t/\tau(i)} \quad \forall i = 1, 2, ..., n \tag{3.1}$$

where, $n$ defines the number of RC pairs needed in the model to best fit the experimental curve. $a_0$ is the steady-state voltage at the end of relaxation period. $a(i)$ is the maximum polarization voltage, $\tau(i)$ is the time constants of the exponential curve [38]. Similarly, for an exponentially falling curve the equation used to fit the measurement is given by,

$$E_{curve}(SOC) = a_0 + \sum_{i=1}^{n} a(i)e^{-t/\tau(i)} \quad \forall i = 1, 2, ..., n \tag{3.2}$$

#### 3.3.3.2   Calculation of $R_0$, $Em$, $R_x$ and $C_x$

All EECM parameters are dependent on the SOC. Circuit parameters are found by the following methods:

- Series resistance $R_0$ can be calculated by the instantaneous voltage drop (or rise) seen when the discharge load current (or charging current) is applied or removed as shown in the voltage response curve. It is calculated using Ohm's law,

$$R_0(SOC) = \frac{\Delta V}{|I|}. \tag{3.3}$$

- $Em(SOC)$ is the voltage at the end of relaxation, hence

$$Em(SOC) = a_0. \tag{3.4}$$

- After finding the time constants $\tau_x$, resistance in the RC pairs is given by,

$$R_{x=i}(SOC) = \frac{a(i)}{I\left[1 - e^{-T_{load}/\tau(i)}\right]} \quad \forall i = 1, 2, ..., n \tag{3.5}$$

where, $I$ is current magnitude having a value of 20 A. $T_{load}$ is the time taken in seconds for the constant discharge current load [38].

- Since, time constant $\tau_x = R_x \cdot C_x$, the value of the capacitance in the RC pairs is given by

$$C_{x=i}(SOC) = \frac{\tau(i)}{R_{x=i}} \quad \forall i = 1, 2, ..., n \tag{3.6}$$

After calculating the values of all the parameters, a look-up table is made with respect to the corresponding SOC breakpoints. These look-up tables will be used in the EECM model and by using a parameter estimation technique, the values of the parameters would be further optimized to minimize the error between measurement and the simulation by using nonlinear least square methods. To achieve this Matlab parameter optimization toolbox[54] is used.

### 3.3.4 EECM model - Simulink

The model is made in the Simulink environment. The model takes magnitude of current $I$ as an input and has terminal voltage $V$ and $SOC$ as outputs.

#### 3.3.4.1 Coulomb counting model

The model uses Coulomb counting or current integration method to calculate the $SOC$. Given by the formula,

$$SOC = SOC_{initial} \pm \int_0^t \frac{|I(t)|}{Capacity} dt \tag{3.7}$$

where, $SOC_{initial} = 1$ for a pulse discharge test when the cell is charged to $100\,\%SOC$ before starting the test and 0 for the pulse charge test when the cell is discharged completely to $0\,\%SOC$ before the start of the test. The $SOC$ value ranges from 0 to 1. *Capacity* is the discharge capacity or charging capacity of the cell in A s. The Coulomb counting model in simulink as shown in figure 3.5 is used for the pulse discharge test and figure 3.6 for the pulse charge test.
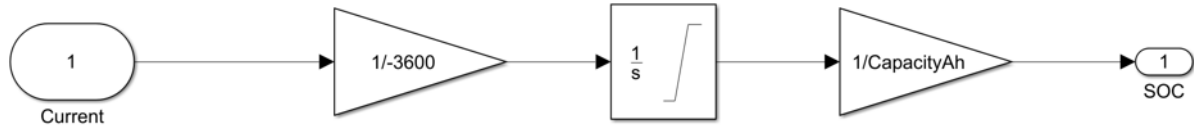
**Figure 3.5:** Coulomb counting model when applying for discharge pulse in Simulink
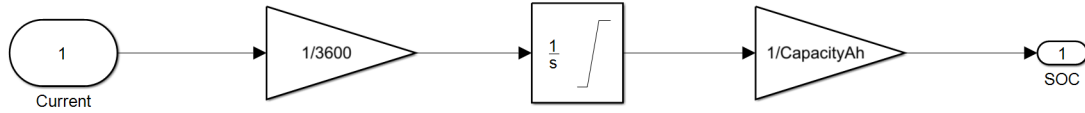


**Figure 3.6:** Coulomb counting model when applying for charging pulse in Simulink

The Coulomb counting model is based on (3.7). The initial capacity of the cell is entered in the integrator block in the Coulomb counting model. The discharge capacity in A h of the cell is given as initial capacity in figure 3.5 and 0 A h as initial capacity in figure 3.6. In (3.7), the $'-'$ sign is used when discharge pulses are used and a $'+'$ sign is used when a charging pulse is used.

### 3.3.4.2  RC pairs model - Simulink

As seen from the equivalent electrical circuit model from figure 2.4, there is a voltage drop across the RC pair $V_{RC}$ and the discharge or charging current $I$ flows through
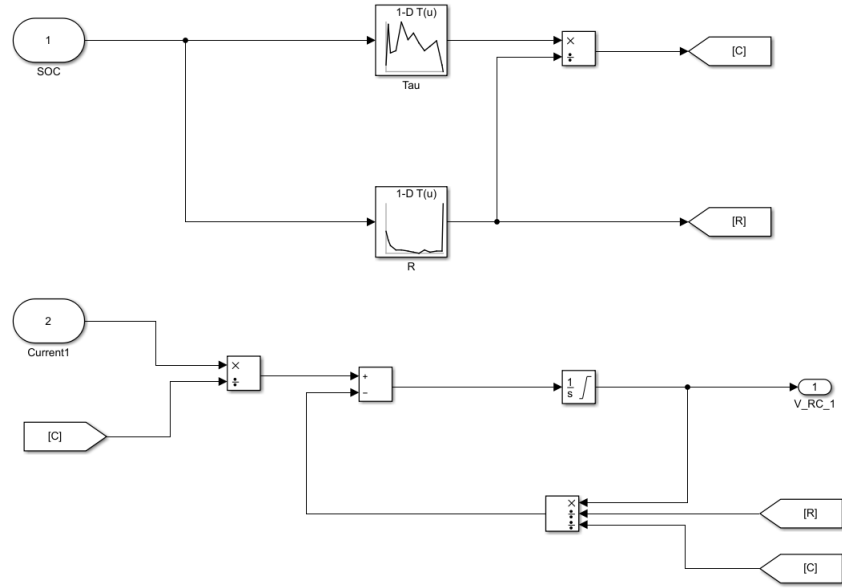
it. Hence, from Kirchoff's current law we can write the following equation for the first RC pair,

$$I = \frac{V_{R_iC_i}}{R_i} + C_i\frac{dV_{R_iC_i}}{dt} \qquad (3.8)$$

$$V_{RCi} = \int_0^t \left(\frac{I}{C_i} - \frac{V_{R_iC_i}}{R_iC_i}\right) dt \qquad (3.9)$$

$\forall i = 1, 2, ..., n$, where $n$ is the number of RC pairs in the model. This can be modelled in Simulink as shown in figure 3.7. From (3.6) $C_i$ is calculated.



**Figure 3.7:** Modelling of the first RC pair in Simulink with look-up tables of $R_1$ and $C_1$

The value of $R_i$ and $C_i$ is chosen from the look-up table with respect to its corresponding SOC breakpoints. These models can be scaled-up based on the selection of number of RC pairs.

### 3.3.4.3  Circuit model - simulink

The final circuit model includes the Coulomb counting method for calculation of SOC, which will give inputs to all the look-up tables of $R_0, R_x, C_x$ and $Em$ in the model, making it possible to choose the correct values based on SOC. By computing the following equation,

$$V(SOC) = Em(SOC) \pm IR_0(SOC) \pm \sum_{i=1}^{n} V_{R_iC_i}(SOC) \quad \forall i = 1, 2, .., n \qquad (3.10)$$

the terminal voltage for the cell can be determined for the corresponding SOC of the cell. In (3.10), a $'-'$ is used for modelling for the pulse discharge test and this is

represented by the simulink model as shown in figure 3.8. For modelling the pulse charge test a ′+′ sign is used instead.
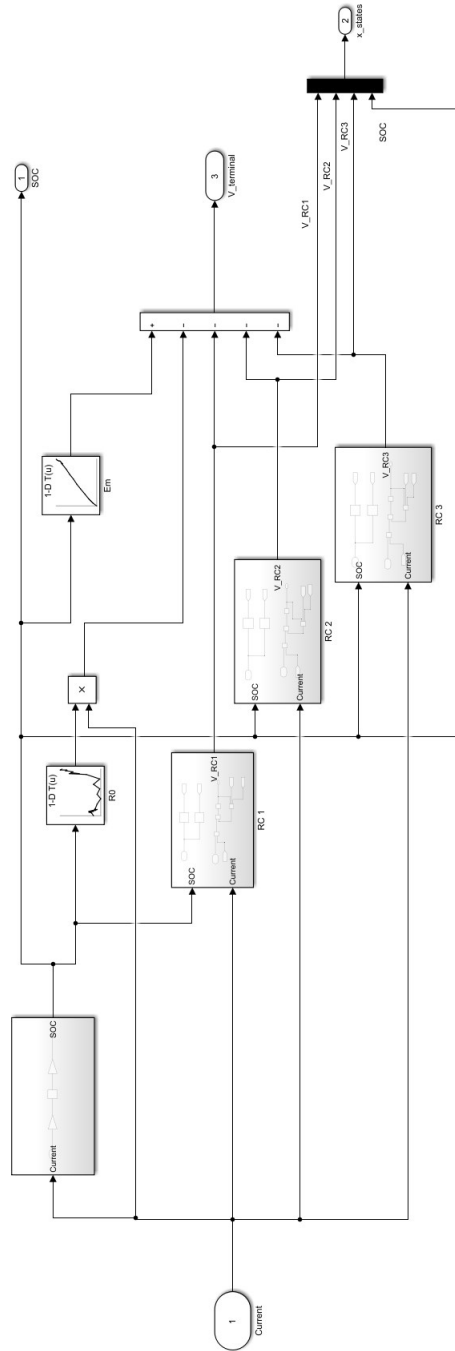


**Figure 3.8:** Equivalent electrical circuit model with coulomb counting for calculation of SOC. In this model 3 RC pairs are used.

### 3.3.5 Parameter estimation

Figure 3.9 shows the procedure for parameter estimation. It is an optimisation algorithm that compares measured with simulated data. It minimises the sum of

squared error using the non-linear least square methods by varying the value of the parameters of interest.



**Figure 3.9:** Parameter estimation procedure [39].

In this case, the measured voltage is compared with the simulated voltage. The parameter estimation algorithm minimises the sum of the squared error between them by varying the parameters $Em$, $R_0$, $R_x$ and $\tau_x$ using the non-linear least square methods [39] [54].

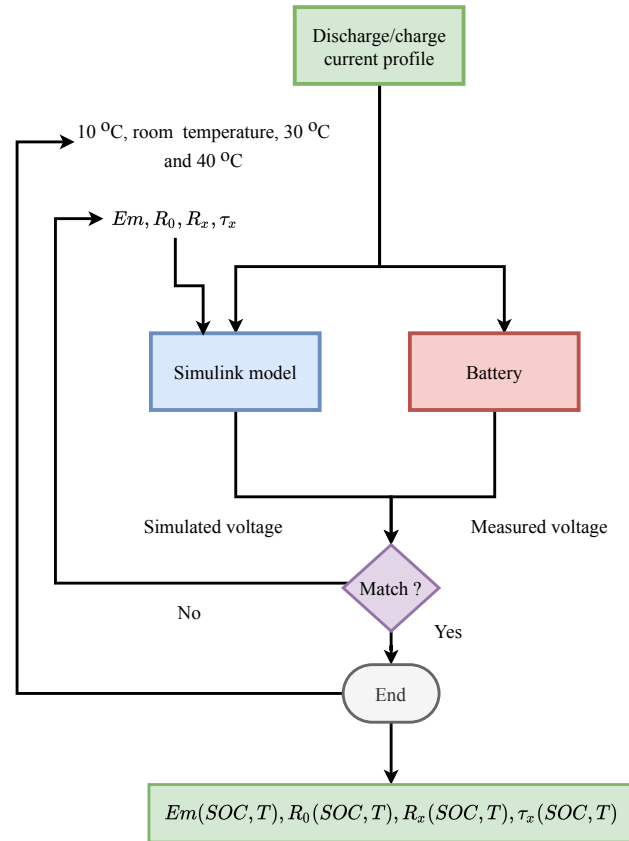This step is repeated in a sequence as mentioned in figure 3.2. Parameter estimation performance is dependant on its initial values. Convergence to the final solution depends on how near the initial values are near to the final values. Calculated values of $Em$, $R_0$, $R_x$ and $\tau_x$ after curve fitting is used as initial values during the first step of parameter estimation. Only two parameters are varied at a time and in the final step of parameter estimation all four circuit parameters are varied to get the best fit. For all the parameters minimum and maximum values are given as an input, so that the value of these parameters stay within their physical limits. To perform the parameter estimation, parameter estimation toolbox [54] available in Simulink is used.

## 3.4 Thermal modelling

The electrical circuit parameters of the EECM model are dependant on the temperature of the cell. Accurate estimation of the temperature of the cell is vital for the model's accuracy. In this section, a novel method for determining the thermal properties of the cell is explained.

### 3.4.1 Thermal characterisation

Thermal properties such as specific heat capacity ($JK^{-1}kg^{-1}$) and thermal resistance ($K\,W^{-1}$) are important parameters irrespective of the thermal model employed. Usually, these two values are not provided by the manufacturer in the data-sheet. A new methodology is proposed in this thesis to determine both the thermal properties of the cell by doing one single experiment and extracting the parameters of interest.

#### 3.4.1.1 Experimental setup

The parameters of interest are extracted using a second-order thermal model. A test is done, where the heating element is sandwiched between the cells. Insulation material with known specific heat capacity is used to cover the setup from all sides as shown in figure 3.10.
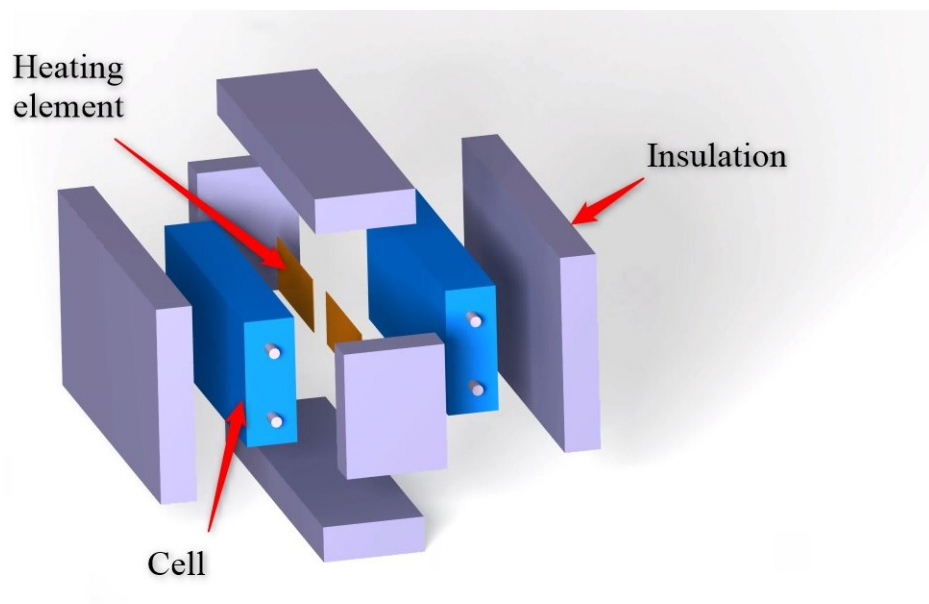


**Figure 3.10:** Exploded view of the setup

In principle, any insulation material with known specific heat capacity can be used for the setup and in this thesis work, polyethylene foam having a volumetric mass density, $\rho = 29.5\,\text{kgm}^{-3}$ and thickness of $10\,\text{mm}$ is used. For polymer's density in the range of 16.7 to $69.5\,\text{kgm}^{-3}$, the specific heat capacity of the insulation material according to [55] is $2450.7\,\text{JK}^{-1}\text{kg}^{-1}$. This value of the specific heat capacity of insulation material is considered and used in further calculations. The insulation material covers the two cells from all sides. Kapton insulated flexible heaters are used as the heating element. It is thin and is useful in this particular application. It is shown in figure 3.11.



**Figure 3.11:** Kapton insulated flexible heater.
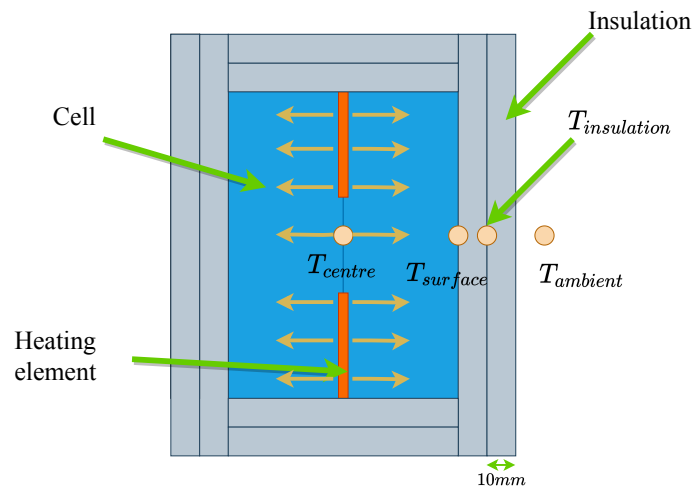


**Figure 3.12:** Top view of the setup and temperature sensors placement.

Four K-type temperature sensors are used in the setup as shown in figure 3.12. Sensors are placed at the **center** in between the cells, one on the **surface** between the cell and the insulation material, one between two layers for **insulation** temperature sensor and finally, one to measure the ambient temperature. The whole

setup is placed inside a thermally insulated box to avoid fluctuations in the external temperature variations on the test.

### 3.4.1.2  Thermal model used for characterisation

The thermal circuit for the setup shown in figure 3.12 is shown in figure 3.13. Two main assumptions of this model are as follows:

- The heating element and the wire of the temperature sensor have some finite thickness. It is small, and it creates a very small air-gap between the two cells. This air-gap is ignored in the thermal circuit. It simplifies the model and makes it symmetric. Hence, it is assumed that the distribution of the rate of change of heat generated is equal in both the direction of the Kapton insulated flexible heater. Therefore, $\dot{Q} = P = \frac{P_W}{2}$ where $P_W$ (W) is the power supplied to the heater.

- Two layers of the insulation material are considered as a single unit. $C_{insulation}$ is heat capacity ($\mathrm{J\,K^{-1}}$) of the insulation material. It is the product of specific heat capacity of the insulation material and the mass of both the layers put together. $R_{insulation}$ is the thermal resistance across the single layer. Ideally the temperature sensor is to be placed in the middle of the insulation layer, but adding it in the middle of the single layer is tricky. This assumption simplifies the problem.

In this thermal model, heat is generated by to the flexible heater, and heat is transferred through the cell and to the other side of the cell to its surface, where there is no mass or specific heat capacity. Heat is then transferred from the cell surface to the ambient through the insulation. Mass and specific heat capacities of the cell and the insulation are lumped together to a point at the centre of their respective bodies.

There are two nodes in the thermal circuit. $T_{centre}, T_{surface}, T_{insulation}$ and $T_{ambient}$ are measurable quantities. $T_{in}$ is the core temperature inside the cell and is not measured. $R_{cell}$ is the thermal resistance of the cell from its core to the surface and $R_{air}$ is the thermal resistance of the air. $C_{cell}$ is the heat capacity of the cell. $C_{cell}$ and $R_{cell}$ are the two unknown quantities to be found.
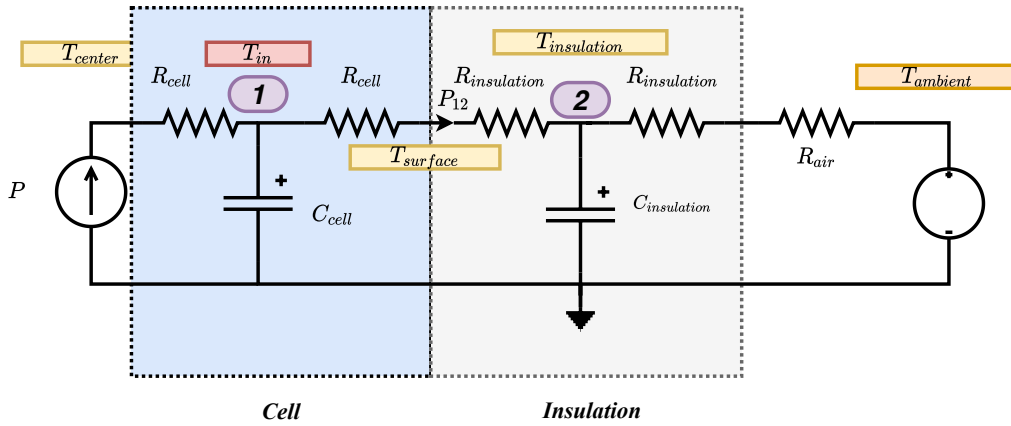
**Figure 3.13:** Thermal circuit model.

The rate of heat generation $P$ in (W) is constant with respect to time and transferred to a point corresponding to $C_{cell}$ in $(\text{J K}^{-1})$ and the change of internal temperature of the cell $T_{in}(\text{K})$ with respect to time $t$ in (s). The heat loss flows away from this point to the surface of the cell. This is dependent on the heat transfer coefficient of the cell, $h_{cell}$ in $(\text{Wm}^{-1}\text{K}^{-1})$ and temperature difference between internal temperature and the surface temperature. The area of the cell $A_{cell}$ in $(\text{m}^2)$ and thickness of the cell $L_{cell}$ in (m) remains constant through out the test and $L_{cell}/h_{cell}A_{cell}$ remains constant. This is referred to the thermal resistance of the cell $R_{cell}$ [28].

Since it is considered that there is no mass at the surface, heat generated is not absorbed at the surface. The heat rate entering this point is equal to the heat rate flowing away. The heat rate that transfers through the insulation is related to the heat coefficient of the insulation, $h_{insulation}$ in $(\text{Wm}^{-2}\text{K}^{-1})$ and temperature difference of the internal temperature of the cell and internal insulation temperature. Area of the insulation $A_{insulation}$ $(\text{m}^2)$ and thickness of the insulation $L_{insulation}$ remains constant throughout the test. Hence, $L_{insulation}/h_{insulation}A_{insulation}$ remains constant and is represented as the inverse of $R_{insulation}$ in $(\text{K W}^{-1})$. In between node 1 and 2,

$$\frac{T_{in}(t) - T_{surface}(t)}{R_{cell}} = \frac{T_{surface}(t) - T_{insulation}(t)}{R_{insulation}} = \frac{T_{in}(t) - T_{insulation}(t)}{R_{in}} = P_{12}$$

and,

$$R_{in} = R_{cell} + R_{insulation} \tag{3.11}$$

Therefore heat balance equation at node 1 is given as,

$$P = C_{cell}\frac{dT_{in}(t)}{dt} + \underbrace{\frac{T_{in}(t) - T_{insulation}(t)}{R_{in}}}_{=P_{12}} \tag{3.12}$$

At node 2, the rate of heat transfers from the cell to a point is related to $C_{insulation}$ $(\text{J K}^{-1})$ and change in insulation temperature with respect to time. The rate of heat flows that away from this point to the ambient is related to the heat transfer

coefficient $h_{insulation} + h_{air}$ and temperature difference of insulation and ambient temperatures. Similar to 3.12, heat balance equation at node 2 is given as,

$$\frac{T_{in}(t) - T_{insulation}(t)}{R_{in}} = C_{insulation}\frac{dT_{insulation}(t)}{dt} + \frac{T_{insulation}(t) - T_{ambient}}{R_{out}} \quad (3.13)$$

where,

$$R_{out} = R_{insulation} + R_{air}. \quad (3.14)$$

$T_{in}$ cannot be measured easily as it is the core temperature of the cell. To measure the internal temperature of the cell, a thermo-couple needs to be placed inside the cell. To do this, a glove box is required, where the inert atmosphere is maintained. This is not easily found in a basic laboratory. In order to simplify further calculations (3.13) is written in terms of $T_{in}$ and is replaced in (3.12) to give second-order differential equation without $T_{in}$,

$$T_{insulation}(t) = PR_{out} + T_{ambient} - 2\zeta\tau\frac{dT_{insulation}(t)}{dt} - \tau^2\frac{d^2T_{insulation}(t)}{dt^2} \quad (3.15)$$

where,

$$\tau = \sqrt{C_{cell}R_{in}C_{insulation}R_{out}} \quad (3.16)$$

$$2\zeta\tau = X = C_{cell}R_{in} + C_{cell}R_{out} + C_{insulation}R_{out} \quad (3.17)$$

To solve the second-order differential equation (3.15) and to find the final solution for $T_{insulation}(t)$ following steps as shown in figure (3.14) is implemented. Ambient temperature is considered to remain constant. The whole setup, before the start of the test, is kept at the ambient temperature. Hence, the initial conditions used in Laplace transformations are,

$$T_{insulation}(t = 0) = T_{ambient}$$
$$\frac{dT_{insulation}(t = 0)}{dt} = 0$$
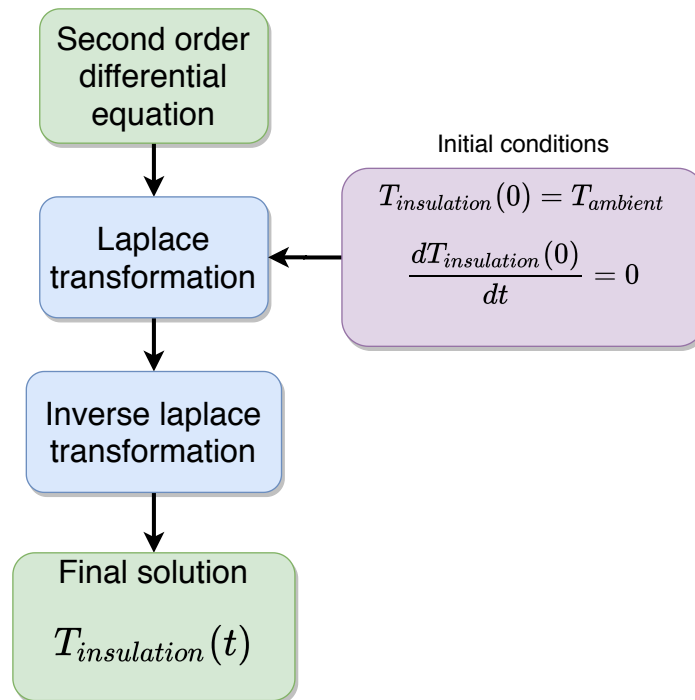
**Figure 3.14:** Steps followed to find the final general solution for $T_{insulation}(t)$.

The final solution is,

$$T_{insulation}(t) = T_{ambient} + PR_{out}\left[1 - e^{\frac{-\zeta t}{\tau}}\left(\cosh\left(\frac{t\sqrt{\zeta^2 - 1}}{\tau}\right) - \frac{\zeta}{\sqrt{\zeta^2 - 1}}\sinh\left(\frac{t\sqrt{\zeta^2 - 1}}{\tau}\right)\right)\right].$$

(3.18)

The above equation represents a second-order over-damped equation where $\zeta > 1$ is the damping coefficient and $\tau$ is the time constant of the system [56].

### 3.4.1.3   Test
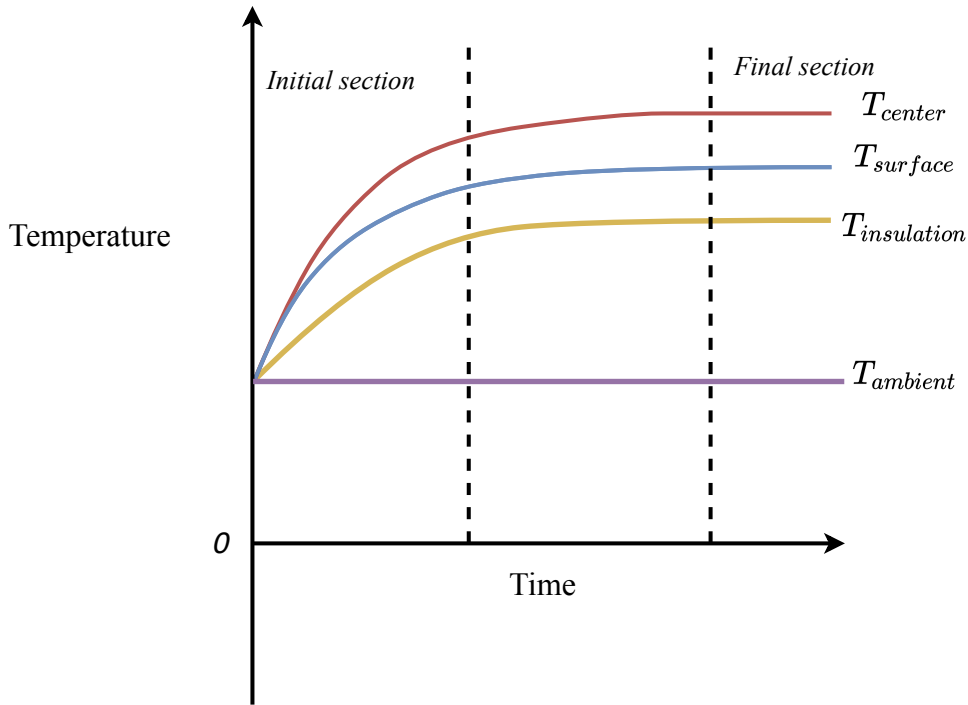


**Figure 3.15:** Test for finding $C_{cell}$ and $R_{cell}$.

Using the same experiment set up as shown in figures 3.10 and 3.12, a simple test is conducted. All the temperature sensor values are recorded during the test. A specified power is supplied to the flexible heater through a power supply to heat up the setup. Before starting the test, the setup must be at the ambient temperature. The test is continued until the temperature reaches a steady state as shown in figure 3.15.

### 3.4.1.4   Parameter extraction

Two important sections are identified from the test, namely the initial and final section as shown in figure 3.15. The steady-state region of the curve is the final section and the transient region is the initial section. To identify the initial section, data between the initial value of the temperature to 95% of the final temperature value is considered. Data for the last one hour of the steady-state part of the curve is the final section.

All the thermal resistances present in the thermal circuit (figure 3.13) are calculated based on the data present in the final section. At steady state, the change of $T_{in}$ and $T_{insulation}$ with respect to time is negligible and is considered to be zero. The effect of $C_{cell}$ and $C_{insulation}$ is therefore neglected at the steady-state. The modified thermal circuit at the steady-state is shown in figure 3.16.
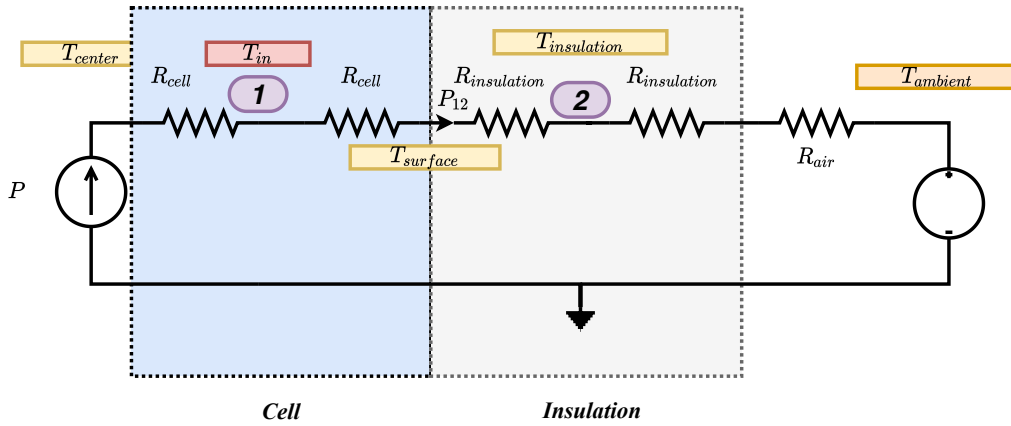
**Figure 3.16:** Thermal circuit at steady state.

As mentioned earlier in the section 3.4.1.2. Due to the symmetry in the experimental setup, the rate of heat transferred from the flexible heater to one side is assumed to be half of the applied power to the heater, $P = P_W/2$. At a steady-state region, $P$ flows through each thermal resistance element in the thermal circuit as shown in figure 3.16. The mean values of the temperatures in the final section are considered for the calculation.

The internal thermal resistance of the cell, $R_{cell}$ is calculated using the mean of the temperature difference between the centre and the surface. It is divided by the rate of heat $P$. It is shown as,

$$R_{cell} = \frac{mean(T_{center}(t = \infty)) - mean(T_{surface}(t = \infty))}{2P}. \tag{3.19}$$

Similar to $R_{cell}$, insulation thermal resistance is calculated by the mean temperature difference between the surface and the insulation as shown,

$$R_{insulation} = \frac{mean(T_{surface}(t = \infty)) - mean(T_{insulation}(t = \infty))}{P} \tag{3.20}$$

$R_{out}$ can be calculated directly by considering the mean temperature difference between insulation and the ambient. Thereby finding $R_{air}$,

$$R_{out} = \frac{mean(T_{insulation}(t = \infty)) - mean(T_{ambient}(t = \infty))}{P} \tag{3.21}$$

$R_{air}$ is the difference of $R_{out}$ and $R_{insulation}$,

$$R_{air} = R_{out} - R_{insulation} \tag{3.22}$$

Using the initial/transient section of the test, $C_{cell}$ is calculated. $C_{insulation}$ is a known quantity. Curve fitting on the initial section of the insulation temperature data is done using the final solution (3.18). Curve fitting is done with the help of the Matlab curve fitting toolbox [47]. Robust non-linear least square method is used for fitting the curve. The time constant $\tau$ and damping coefficient $\zeta$ are extracted.

Giving lower and upper bounds to the damping coefficient is important and it affects the values of both $\zeta$ and $\tau$.

An algorithm is proposed and is shown in figure 3.17. This algorithm is to select the right values for lower and higher limits of $\zeta$, and thereby to calculate the correct value of $C_{cell}$. The main principle of this method is to select the lower and higher limits for $\zeta$ such that, the absolute error between $R_{in}$ and $R_{in_{estim}}$ is minimum ($< 0.1\%$). Where $R_{in_{estim}}$ is the estimated sum of $R_{cell}$ and $R_{insulation}$. Once the correct value of $\zeta$ is found, $C_{cell}$ is calculated based on the given value of $\zeta$.

A Parameter sweep for $\zeta_{min}$ and $\zeta_{max}$ is done having a fixed difference ($\zeta_{max} - \zeta_{min} = m$) between them. Curve fitting for initial section of $T_{insulation}(t)$ is done to extract estimated values of time constant $\tau_{estim}$ and damping coefficient $\zeta_{estim}$. $\tau_{in_{estim}}$ is calculated by using (3.16) as shown,

$$\tau_{in_{estim}} = R_{in_{estim}} C_{cell_{estim}} = \frac{\tau_{estim}^2}{C_{insulation} R_{out}} \tag{3.23}$$

and $C_{cell_{estim}}$ is calculated by using (3.17),

$$C_{cell_{estim}} = \frac{2\tau_{estim}\zeta_{estim} - R_{out}C_{insulation} + \tau_{in_{estim}}}{R_{out}}. \tag{3.24}$$

Hence, $R_{in_{estim}}$ is calculated as,

$$R_{in_{estim}} = \frac{\tau_{in_{estim}}}{C_{cell_{estim}}}. \tag{3.25}$$

The error between the actual value of $R_{in}$ found based on experimental values in (3.11) and estimated value of internal thermal resistance (3.25) in percentage is given as,

$$R_{in_{error}} = \frac{R_{in} - R_{in_{estim}}}{R_{in}} \times 100. \tag{3.26}$$

After completing all the iterations (*iter*), the absolute minimum value in vector $R_{cell_{error}}$ is checked. If the minimum value is less than $0.1\%$, then computation is stopped. $C_{cell}(\mathrm{J\,K^{-1}})$ is calculated using (3.24). $C_{cell}$ is divided by its measured weight $0.606\,\mathrm{kg}$ to get the specific heat capacity $C_{p_{cell}}$ ($\mathrm{Jkg^{-1}K^{-1}}$). It is calculated for the value of $\zeta$ and $\tau$, for the least $R_{cell_{error}}$.

If $R_{cell_{error}}$ is not $<0.1\%$, the same procedure is repeated. It is repeated by updating the initial conditions. The index corresponding to the absolute minimum error $R_{in_{error}}$ is identified as $x$. The new range of $n_{min}$ and $n_{max}$ is selected around $x$. This leads to narrowing down the variables $n_{min}$ and $n_{max}$. The difference between $\zeta_{max}$ and $\zeta_{min}$ is $m$, which is reduced by a factor of 10 times. Decreasing $m$ increases the precision.
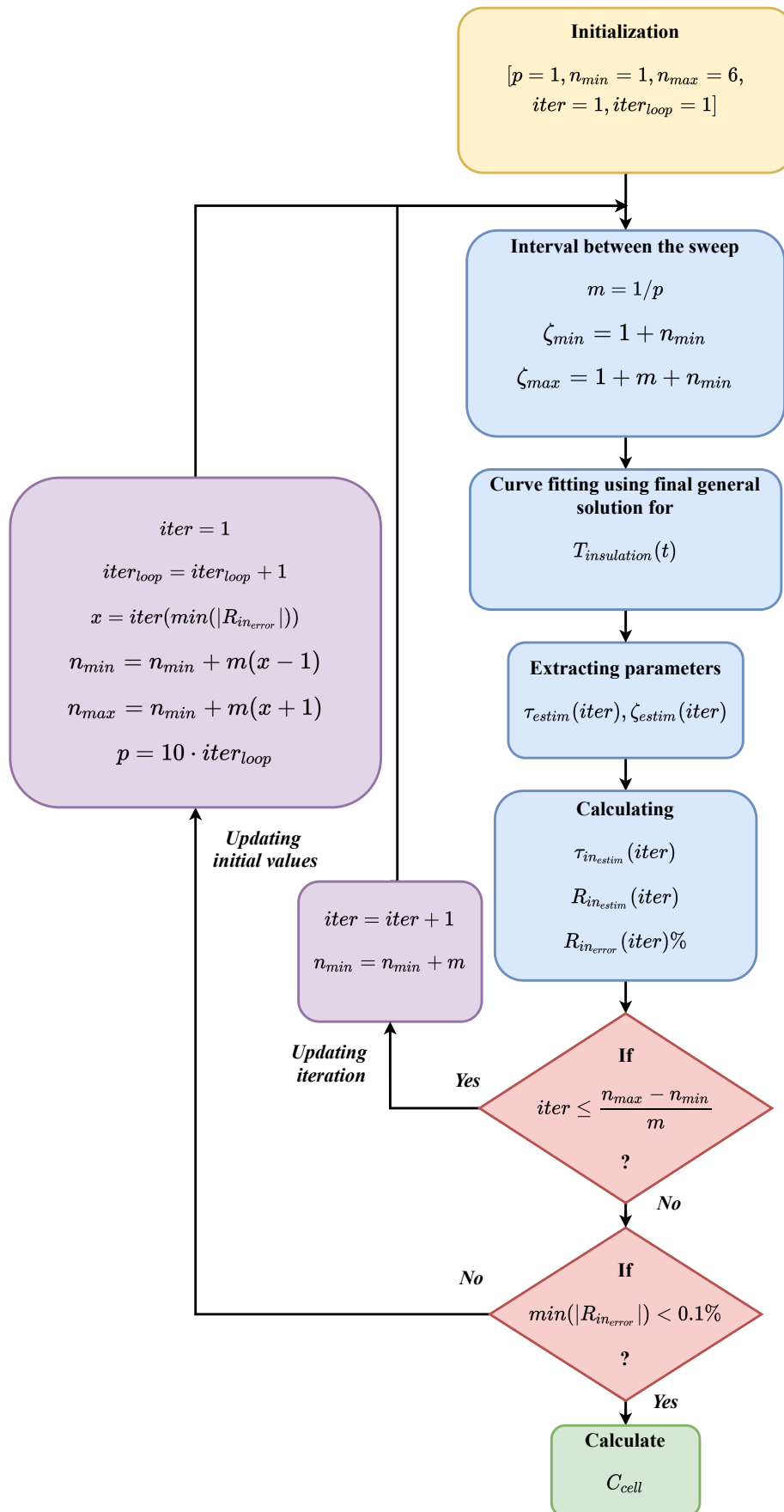
**Figure 3.17:** Algorithm to select the value for zeta. Thereby, calculating the value of $C_{cell}$.

## 3.4.2    Determining entropic coefficients

One of the sources of the heat generation in the battery is due to reversible losses and it is due to change in entropic coefficients. Entropic coefficients change with different $SOC$. The potentiometric test is one of the standard methods to determine the entropic coefficients of the cell. In this section, the test and methodology used in this thesis are presented.

### 3.4.2.1    Potentiometric test

In this experiment, the cell is placed in the temperature chamber. The temperature is changed to three different temperatures at different $SOC$ levels. In this thesis, 11 $SOC$ levels are chosen, starting from $100\% - 0\%$. Open circuit voltage is measured at each temperature levels. Before measuring, the cell must be at its thermal equilibrium state. $0.1C$ discharge current is used to discharge the cell by $10\%SOC$ to shift to the next $SOC$ level. After each discharge pulse, the cell is relaxed to at least 5 hours. The Temperature is changed and it is maintained for at least for 2 hours for the cell to reach its thermal equilibrium.

### 3.4.2.2    Methodology to find entropic coefficient

In this methodology, the temperature change $\Delta T$ affects the result and not the absolute temperature [29]. High accuracy measurement of voltage and temperature is important. The relaxation background of the cell after each pulse discharge is found by using the first-order polynomial fit. The voltage at the point after reaching thermal equilibrium is recorded. Its value is subtracted against the relaxation background to give 'voltage change'points. The slope of these three voltage change points at three different temperatures gives $dU/dT$ for a particular $SOC$ level.

## 3.5 Cell Simulation model

The cell model is made using Simulink after parameterization for the EECM, thermal characterisation and finding the entropic coefficients. An overview of the cell model is shown in figure 3.18. This model has two inputs and three outputs. Current and ambient temperature is given as input. Surface temperature, cell voltage and $SOC$ are the outputs.

Two separate blocks for EECM based on discharge and charge parameters are made, to suit convenience for the modelling. Both of these models need three inputs. It needs state of charge of the cell $SOC$, the estimated surface temperature of the cell $T$, and the absolute value of discharge or charging current that flows away or to the cell $|I|$. Outputs of these blocks are discharge voltage $V_{discharge}$ and charge voltage $V_{charge}$. Decision block helps in deciding output cell voltage to be either $V_{discharge}$ or $V_{charge}$ based on the current $I$ input to the block.

A Coulomb counting block calculates $SOC$ using the current integration method as mentioned earlier in section 3.3.4.1. It takes current as the input and gives calculated $SOC$ as output. This is one of the outputs of the cell model, also it is used as inputs to thermal and EECM models. The thermal model estimates the surface temperature of the cell $T$ using ambient temperature, current $I$ and $SOC$. This model will be discussed in detail in the coming section 3.5.2.
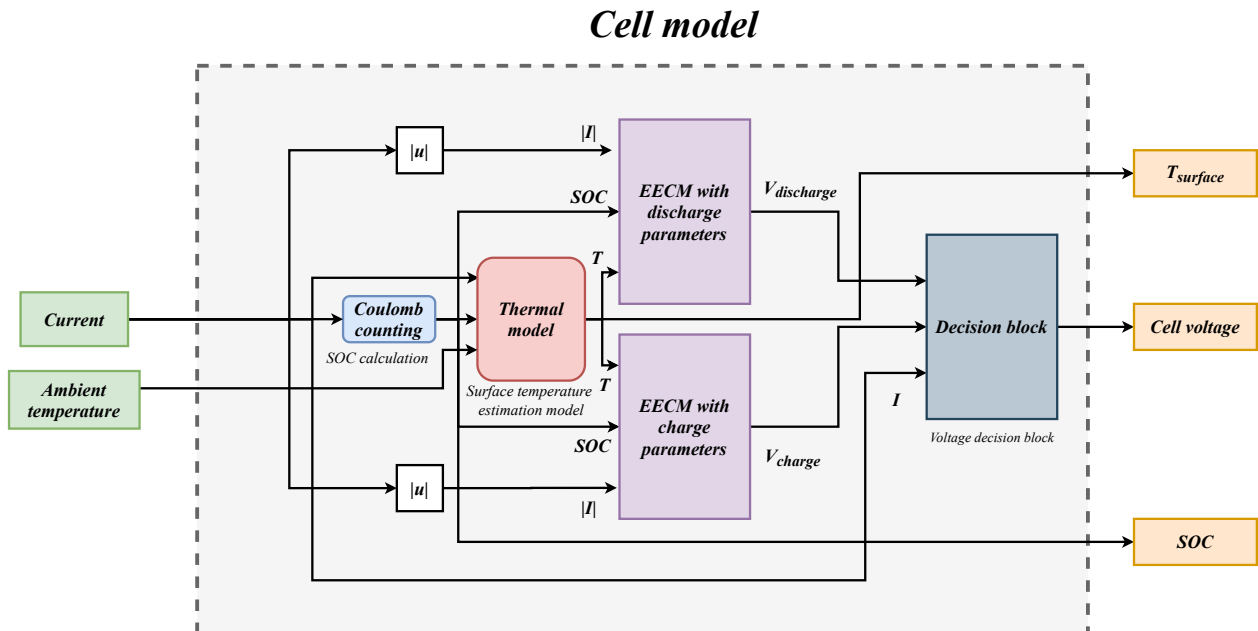
### Cell model



**Figure 3.18:** Overall view of the cell model.

### 3.5.1 Electrical model

The electrical model has two EECM models. Discharge and charge EECM models are modelled according to (3.10). It is the same model used for electrical character-

isation with some differences. 3-D look up[2]tables are made for all parameters and it is replaced instead of the 2-D look-up table (in figure 3.8). The two dimensions are surface temperature of the cell $T$ and state of charge of the cell $SOC$. This is as shown in figure 3.19.

### 3.5.2   Thermal model
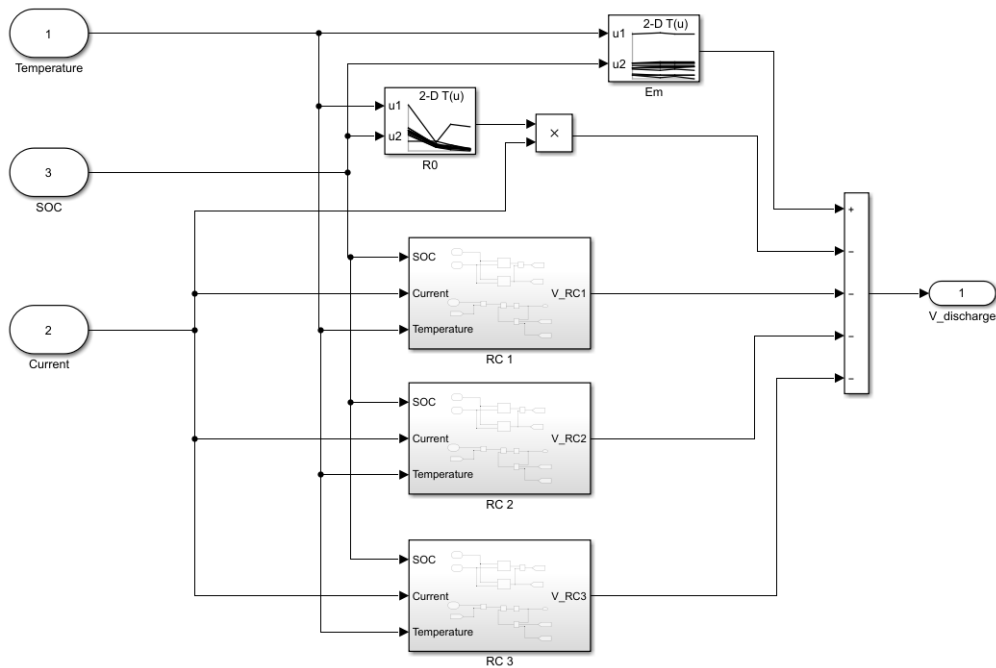


**Figure 3.19:** EECM model using discharge parameters. 3-D look up table is used for all parameters. Where surface temperature $T$ and $SOC$ are the two dimensions to decide the correct value of the parameter.

$RC_x$ are the blocks which calculate the voltage across the $RC$ links in the EECM. 3-D look up tables are used instead of 2-D look up table as shown in figure 3.20. The EECM block with charging parameters are modelled similarly.

A simple first-order thermal model is made using the thermal properties of the cell such as specific heat capacity, the thermal resistance of the cell and entropic coefficients. It is to estimate the surface temperature of the cell.

---

[2]In 3-D lookup tables one dimension belongs to the dependant variable and the other two variables are independent variables. In Simulink it is given as 2-D lookup table. In Simulink all look up tables are shown as one lesser dimension.
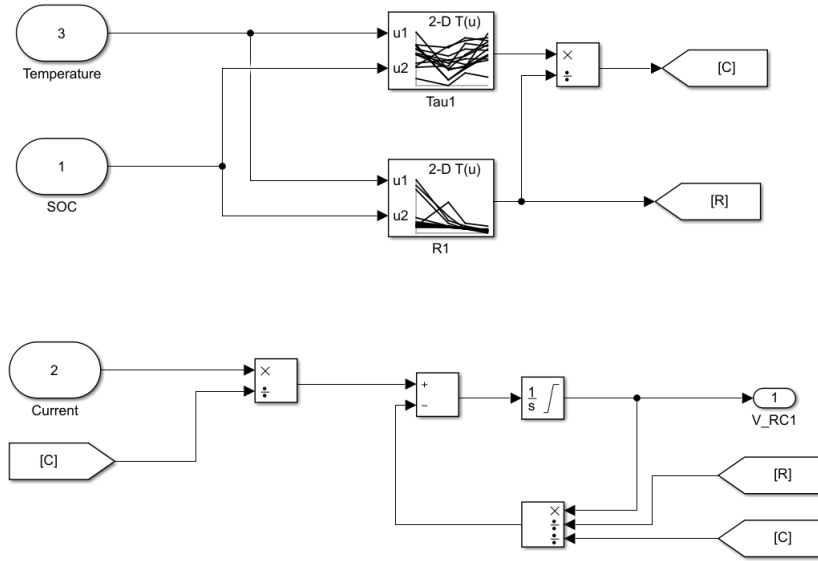
**Figure 3.20:** Model to calculate voltage across RC pair. 3-D lookup table for $\tau$ and $R_1$ is used.

### 3.5.2.1 Calculation of Losses

One of the inputs to the model is the rate of heat loss, $P$. It is the sum of irreversible and reversible losses of the cell. Irreversible losses are the losses due to Ohmic, activation overpotential and concentration overpotential in the cell during its operation. Reversible losses are caused by entropic change. A power loss model is made to feed into the thermal model as an input, as shown in figure 3.21. Irreversible heat loss is calculated as the sum of Ohmic losses due to $R_0$ and all the voltage drops across the $RC$ links in the electrical circuit model. Hence, it can be represented in the equation as,

$$P_{irr} = I|(V - V_{OCV})| = \underbrace{I^2 R_0}_{\text{Ohmic losses}} + \underbrace{I(V_{RC1} + V_{RC2} + ... + V_{RCn})}_{\text{Activation + Concentration overpotential losses}} \tag{3.27}$$

where $n$ is the number of RC pairs in the model. This is shown in figure 3.23. Irreversible heat loss is calculated for both discharge and charge parameters. It is supplied to the decision block, as shown in figure 3.22. The decision subsystem block outputs either losses calculated due to discharge or charge parameters based on the direction of the current. The reversible heat loss is given as,

$$P_{rev} = IT\frac{dU}{dT} \tag{3.28}$$

where, current $I$ is negative for discharge current and positive for charging current. The surface temperature $T$ is in K. $dU/dT$ is V°C$^{-1}$ or VK$^{-1}$. Hence, heat losses are calculated as the sum of both irreversible and reversible heat losses as,

$$P = P_{irr} + P_{rev} \tag{3.29}$$
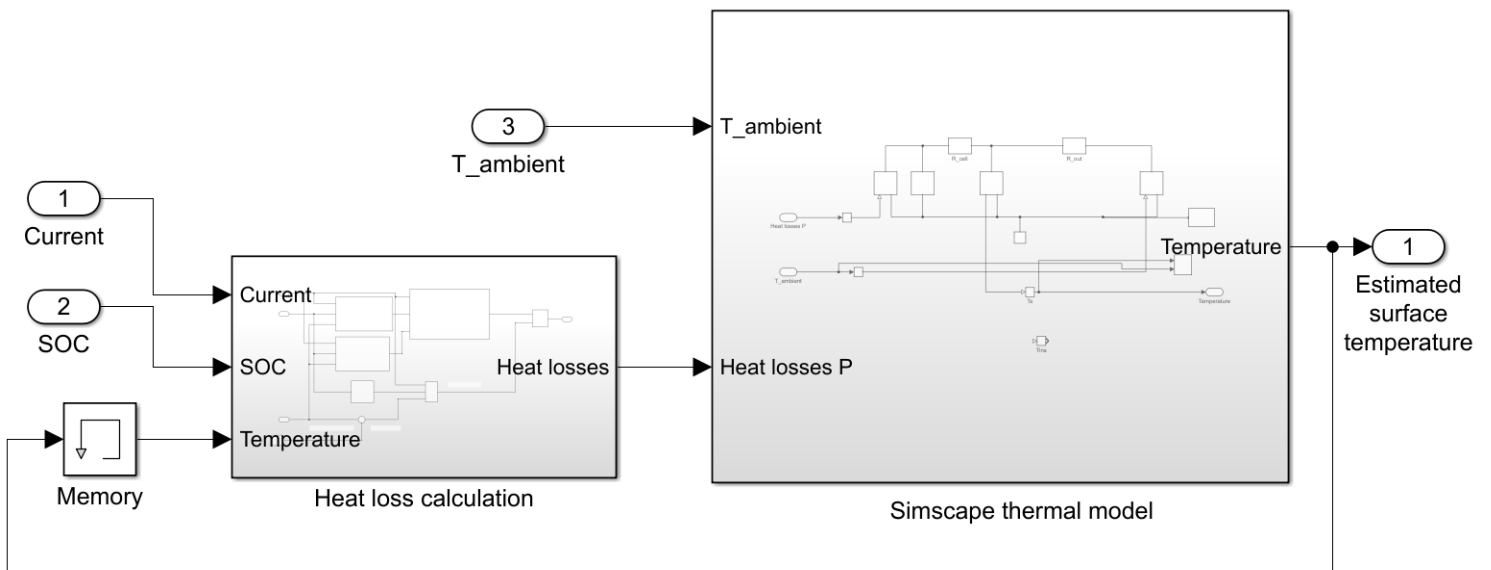
**Figure 3.21:** Overview of the thermal model. Output of Heat loss calculation model is fed as an input to the simscape model. Memory block is there to give delayed input to the heat loss calculation by one time instant. It has initial value equal to the ambient temperature.
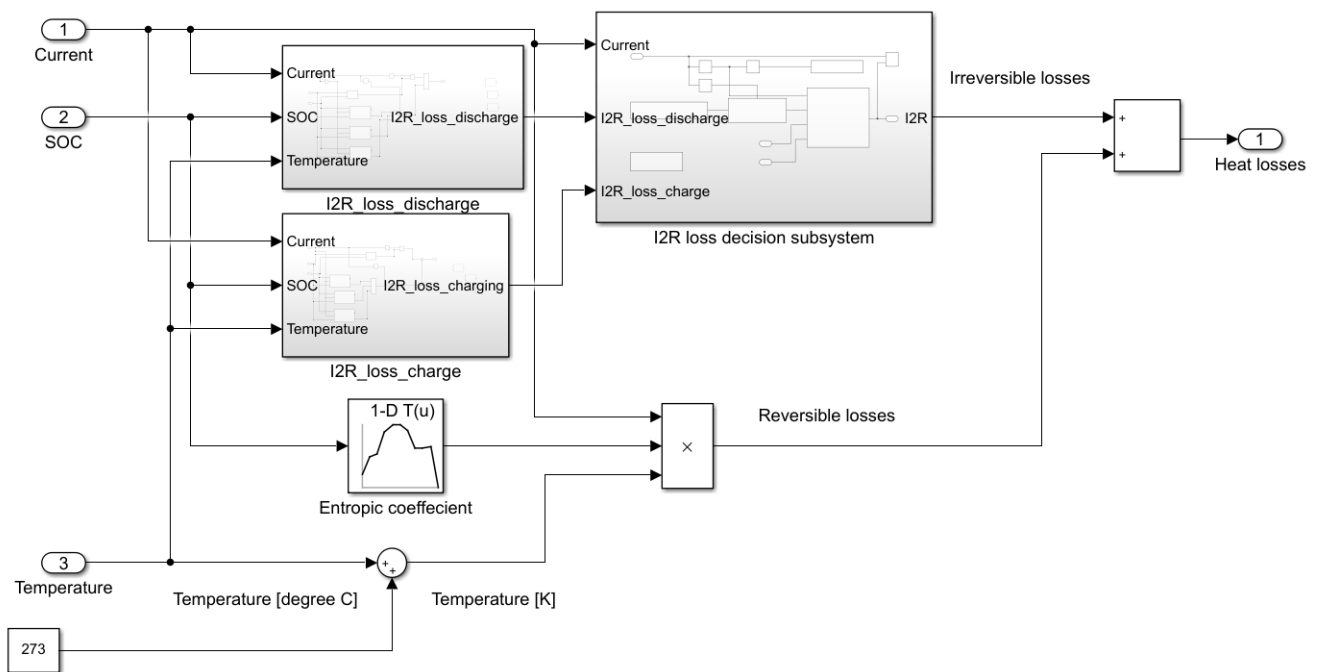


**Figure 3.22:** Heat loss calculation model.

**Figure 3.23:** Irreversible Heat loss calculation model using 3 *RC* links. All are discharge EECM parameters.

#### 3.5.2.2 Simscape model - for surface temperature estimation

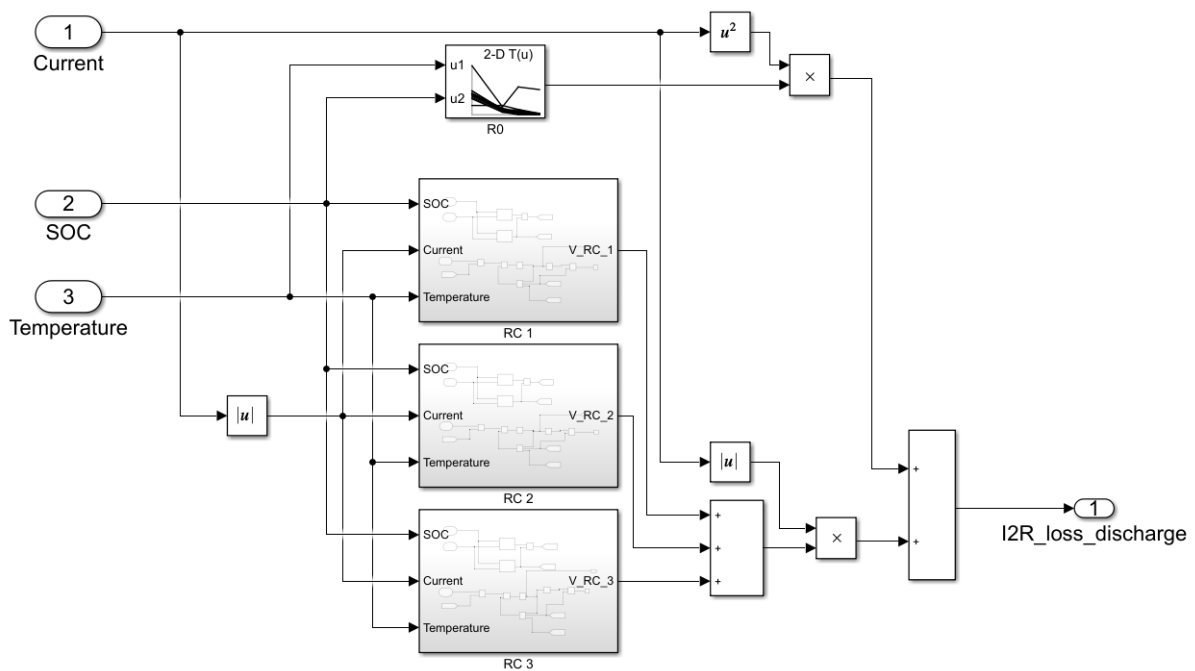The heat losses calculated in the previous section is fed as an input, to the Simscape thermal model to estimate the surface temperature of the cell. A first-order thermal circuit model of the cell is made to estimate the surface temperature. The temperature is assumed to be from the core of the cell moving outwards to the surface of the cell and later to the ambient. Heat losses $P$ and ambient temperature are given as the inputs. $C_{cell}$ and $R_{cell}$ are heat capacity and thermal resistance of the cell. $R_{out}$ is the thermal resistance due to both thermal conductivity and the convective heat transfer coefficient of the air.
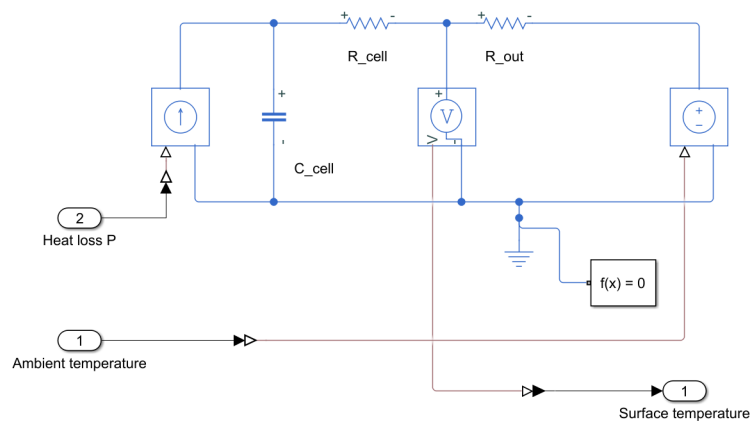


**Figure 3.24:** Thermal model - Simscape model

### 3.5.3 Decision block



**Figure 3.25:** Decision block flowchart

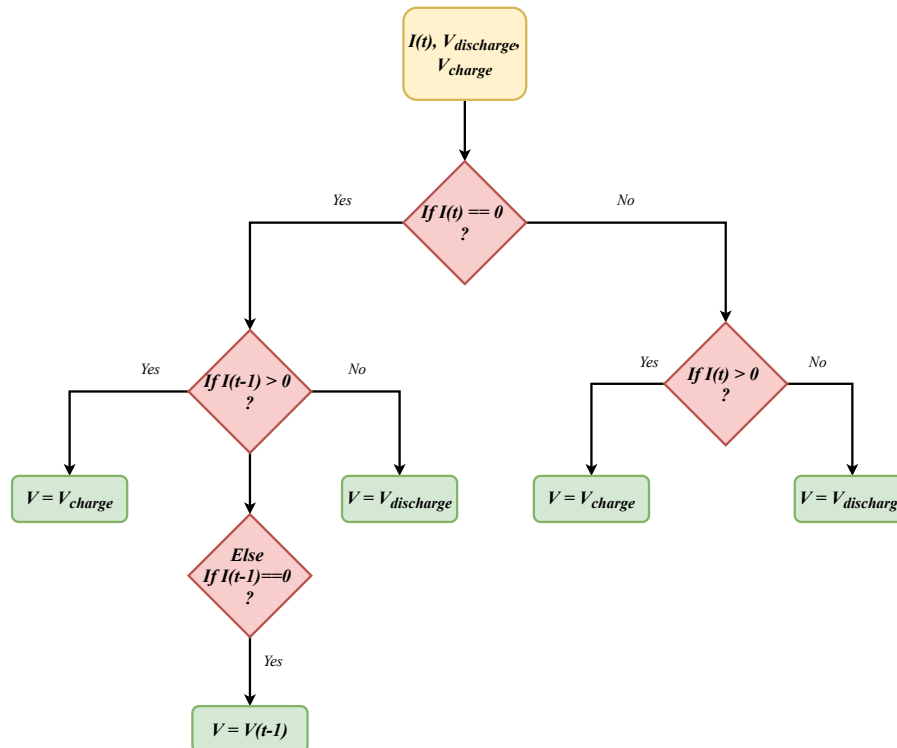The decision block is a generic block. It is used to decide between outputs from two blocks as its output based on the direction of the current. It works on the logic as presented in the flowchart as shown in figure 3.25. The logic is implemented in Simulink. In figure 3.18, a decision block is used. It has three inputs. The output of voltage of EECM block due to discharge and charge parameters, $V_{discharge}$ and $V_{charge}$. Another input is current. A common convention is used here. When the current is negative, $V_{discharge}$ is the output of the Decision block. When the current is positive, $V_{charge}$ is chosen as the output. When current is zero, then the value of current at its previous time instant is considered for the decision.

This decision block is also used in heat loss calculation model (figure 3.22), where the block output is either irreversible loss calculated due to either discharge or charge parameters based on the current. This decision block will be used wherever a decision needs to be taken between output due to either discharge or charge parameters due to the direction of current.
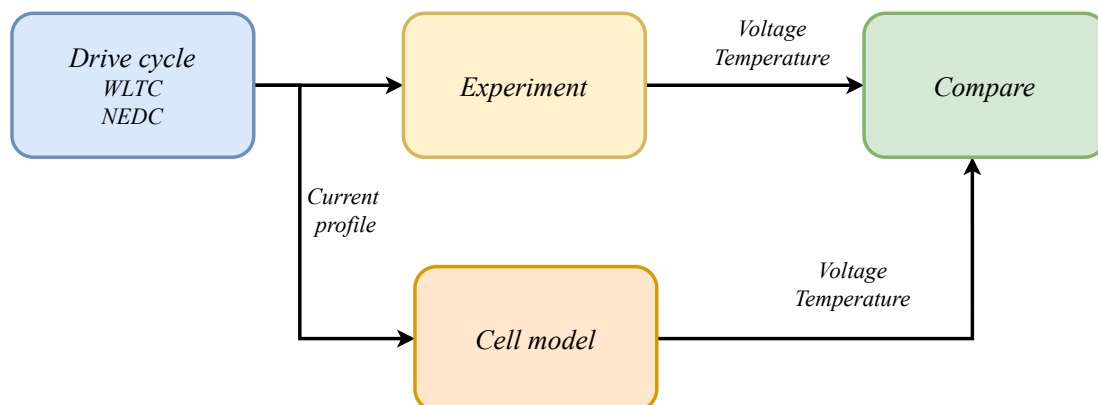
## 3.6  Drive cycle

Conventionally, test cycles are used to know pollutant emissions and fuel consumption of different vehicles based on standardised speed and elevation profile [52]. The driving cycle is the speed profile of the vehicle with respect to time. In BEV, these

cycles would be useful in knowing the performances of various electric components of the vehicle. In this thesis, test cycles will be used in validating the cell model, as shown in figure 3.26.

The Worldwide harmonised Light-duty driving Test Cycle (WLTC) and the New European Drive Cycle (NEDC) are used for validation purpose in this thesis work. Current profiles from these cycles have various points of discharge and charging of the cell. The cell is subjected to this current profile. Voltage and surface temperature of the cell are measured from the test. The same current profile is given as input to the cell model. The voltage and estimated surface temperature output of the model is then compared with that of the experiment.



**Figure 3.26:** Validation procedure using drive cycle

The WLTC drive cycle has four regions. It has four phases based on speed. Each phases has speed limits. Low phase is $<50\,\mathrm{km\,h^{-1}}$, mid phase is $<70\,\mathrm{km\,h^{-1}}$, high phase is $<110\,\mathrm{km\,h^{-1}}$ and extra high phase is $>110\,\mathrm{km\,h^{-1}}$ [57]. The speed profile is shown in figure 3.27.

The speed of the vehicle, time, gradient and gear shifts are available from drive cycle data. To calculate the traction force $F_t$ vehicle parameters are required. Vehicle parameters mentioned in appendix A.
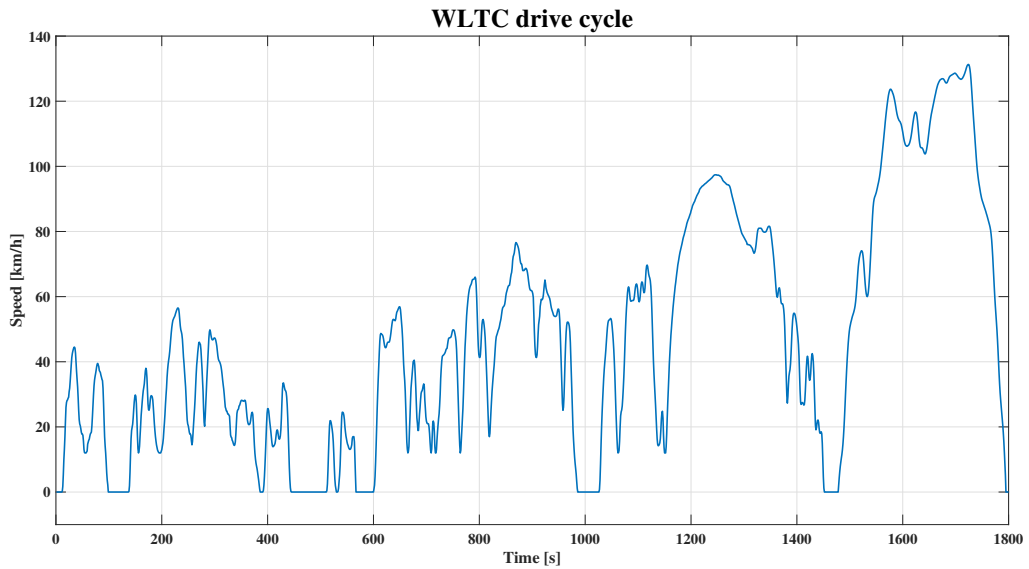
**Figure 3.27:** WLTC speed profile

Using vehicle parameters and drive cycle data, the aerodynamic frictional force $F_a$, rolling frictional force $F_r$, resistive force due to gradient $F_g$ and thereby traction force $F_t$ is calculated using (2.11 - 2.15). The Power profile for the WLTC drive cycle is done using (2.12) and is shown in figure 3.28
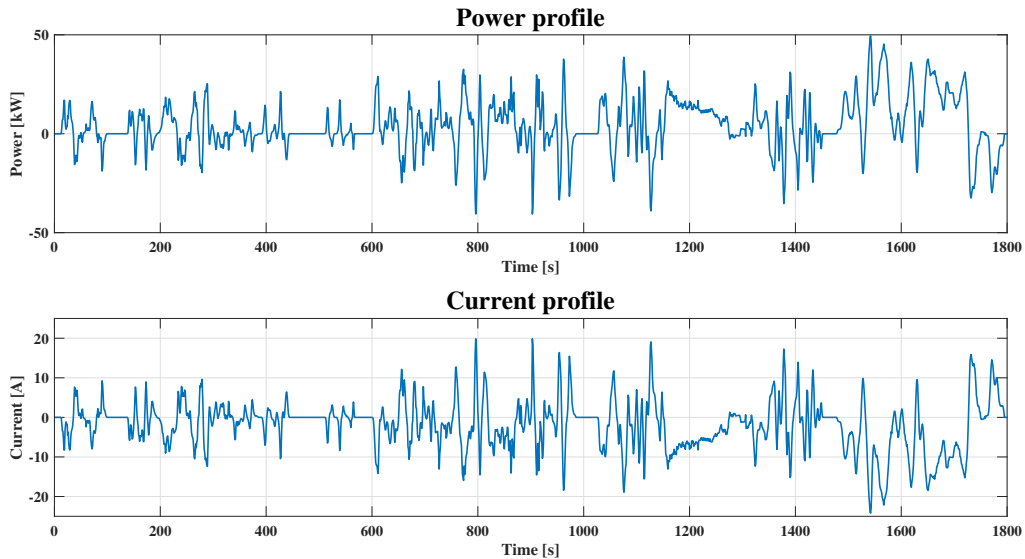


**Figure 3.28:** WLTC power and current profile

The current flowing in a cell in a battery pack at each time instant makes up for a current profile. To calculate the current at each time instant using the power profile, a few assumptions are made. It is considered that 20 % of the additional current is required for running the other auxiliary equipment in the vehicle and due to electrical losses. A battery pack having $n_{series} = 112$ cells in series and $n_{parallel}$

= 6 is assumed, to make sure that the charging current stays below the charging current limit of 20 A. Hence, the current is calculated as,

$$I_{profile} = 1.2 \frac{P_t}{V_{nom} n_{series} n_{parallel}}.$$ 
$$(3.30)$$
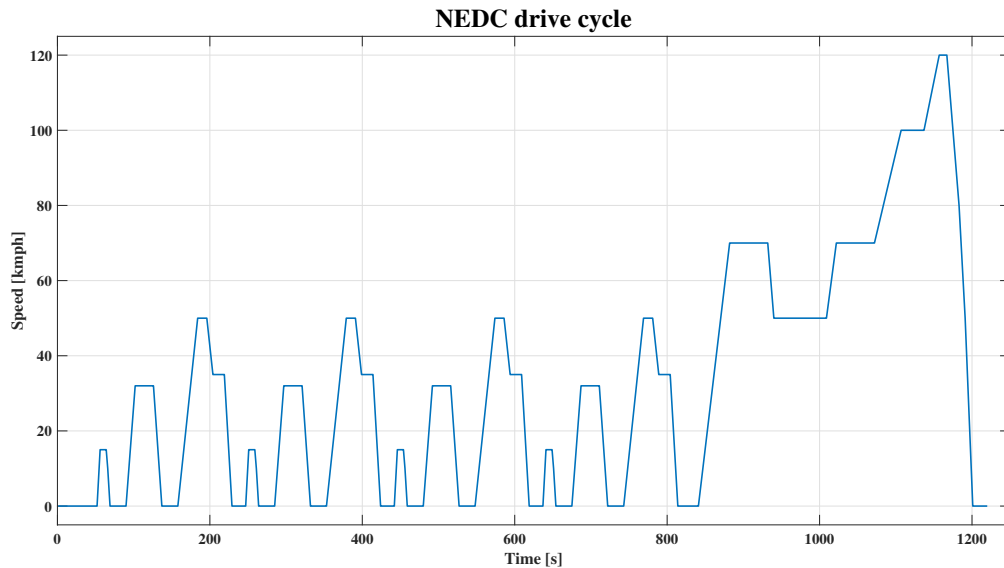


**Figure 3.29:** NEDC speed profile
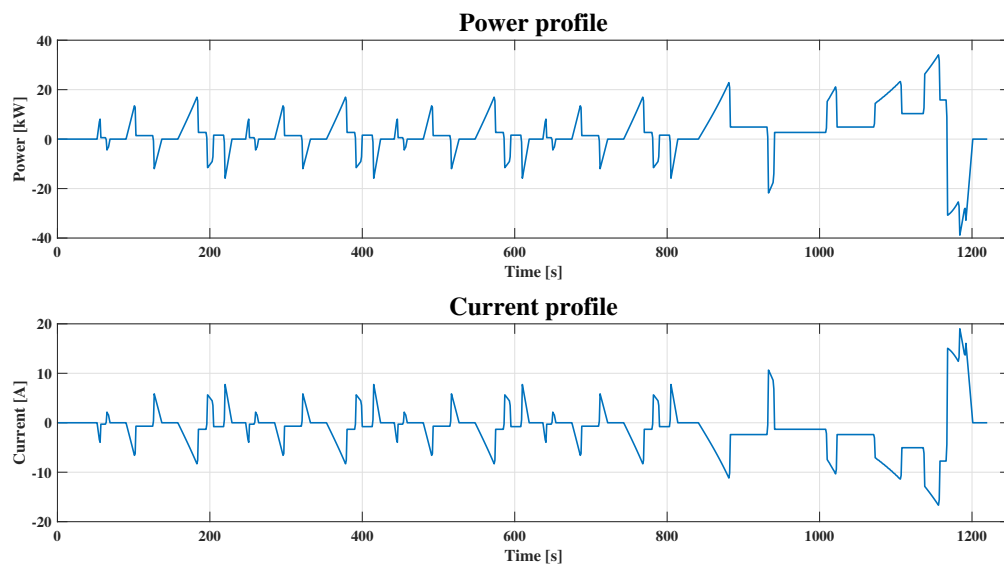


**Figure 3.30:** NEDC power and current profile

The NEDC drive cycle is also called as Motor Vehicles Emission Group (MVEG) drive cycle. It is one of the standard test cycles used for evaluating emissions of

the vehicle. Its drive cycle is shown in figure 3.29. Its tractive force $F_t$ and tractive power profile $P_t$ is made. Current profile of both WLTC and NEDC is made using (3.30) and is shown in figures 3.28 and 3.30. The negative current represents the discharging current and vice versa for positive current.

## 3.7 SOC estimation model

In this thesis, $SOC$ estimation model is made to demonstrate one of the many applications of the cell model. The cell model can be implemented in the Battery Management Systems(BMS) since most of the parameters have look-up tables and thus, it can be easily implemented on a microprocessor. $BMS$ usually measures the terminal voltage, current and temperature of the battery. With this sensor information, it is possible to estimate the $SOC$ and the methodology to show this will be discussed in this section.

### 3.7.1 State space modelling

The first step is to make the state-space modelling of the electrical model to find the matrices $A$, $B$, $C$ and $D$. From (3.8 and 3.7), state space equations can be written as,

$$\frac{dV_{R_iC_i}}{dt} = -\frac{1}{R_iC_i}V_{R_iC_i} + \frac{1}{C_i}I, \quad \forall i = 1, ..., n \tag{3.31}$$

$$\frac{dSOC}{dt} = \frac{1}{Capacity \times 3600}I \tag{3.32}$$

and this is of the form,

$$\dot{x} = Ax(t) + Bu(t)$$

Hence, if three $RC$ pairs are used in the EECM, then n = 3 the continuous-time domain process equations are given as,

$$\underbrace{\begin{bmatrix} \frac{dV_{R_1C_1}}{dt} \\ \frac{dV_{R_2C_2}}{dt} \\ \frac{dV_{R_3C_3}}{dt} \\ \frac{dSOC}{dt} \end{bmatrix}}_{\dot{x}(t)} = \underbrace{\begin{bmatrix} -\frac{1}{R_1C_1} & 0 & 0 & 0 \\ 0 & -\frac{1}{R_2C_2} & 0 & 0 \\ 0 & 0 & -\frac{1}{R_3C_3} & 0 \\ 0 & 0 & 0 & 0 \end{bmatrix}}_{Matrix-A} \underbrace{\begin{bmatrix} V_{R_1C_1} \\ V_{R_2C_2} \\ V_{R_3C_3} \\ SOC \end{bmatrix}}_{x(t)} + \underbrace{\begin{bmatrix} \frac{1}{C_1} \\ \frac{1}{C_2} \\ \frac{1}{C_3} \\ \frac{1}{Capacity \times 3600} \end{bmatrix}}_{Matrix-B} \underbrace{\begin{bmatrix} I \end{bmatrix}}_{u(t)}$$

$$\tag{3.33}$$

The above measurement equation is discretised using *Zero order hold* to find the new $Matrix - A_d$ and $Matrix - B_d$ as shown,

$$A_d = e^{AT_s} = \begin{bmatrix} e^{-\frac{1}{R_1 C_1}} & 0 & 0 & 0 \\ 0 & e^{-\frac{1}{R_2 C_2}} & 0 & 0 \\ 0 & 0 & e^{-\frac{1}{R_3 C_3}} & 0 \\ 0 & 0 & 0 & 1 \end{bmatrix} \qquad (3.34)$$

$$B_d = A^{-1}[e^{AT_s} - 1]B = \begin{bmatrix} R_1\left(1 - e^{\frac{T_s}{R_1 C_1}}\right) \\ R_2\left(1 - e^{\frac{T_s}{R_2 C_2}}\right) \\ R_3\left(1 - e^{\frac{T_s}{R_3 C_3}}\right) \\ \frac{-Ts}{Capacity \times 3600} \end{bmatrix} \qquad (3.35)$$

where, $T_s$ is the sampling rate in *seconds*. The measurement equation is based on the final output equation of the model (3.10) and it is given as,

$$y(t) = Em(SOC) \pm V_{R_1 C_1} \pm V_{R_2 C_2} \pm V_{R_3 C_3} \pm |I|R_0 \qquad (3.36)$$

where, $'-'$ is used when the cell is discharging and $'+'$ is used when charging. Since, $Em$ is non-linear and is dependant on both $SOC$ and $T$, it is linearised using the first order Taylor series. Using the Jacobian for the measurement equation, the matrices $C$ and $D$ are given as,

$$C_d = \frac{\partial y}{\partial x}|_{x=\widehat{x}_k} = \begin{bmatrix} \pm 1 \pm 1 \pm 1 \frac{\partial Em}{\partial SOC} \end{bmatrix} \qquad (3.37)$$

$$D_d = \frac{\partial y}{\partial u} = \begin{bmatrix} R_0 \end{bmatrix} \qquad (3.38)$$

### 3.7.2 Observer

Figure 3.31 represents the block diagram of the process model and observer model. It is done based on the state and measurement equations which were discussed earlier. The process model represents the operation of the actual cell, having the current as input and terminal voltage as the output. The observer model is the observer whose output is the estimated states $\widehat{x}$. It compares the process output $y$ and estimated output $\widehat{y}$ and feeds to the gain $K$ to correct the estimated states to match the actual values of the terminal voltage of the cell.
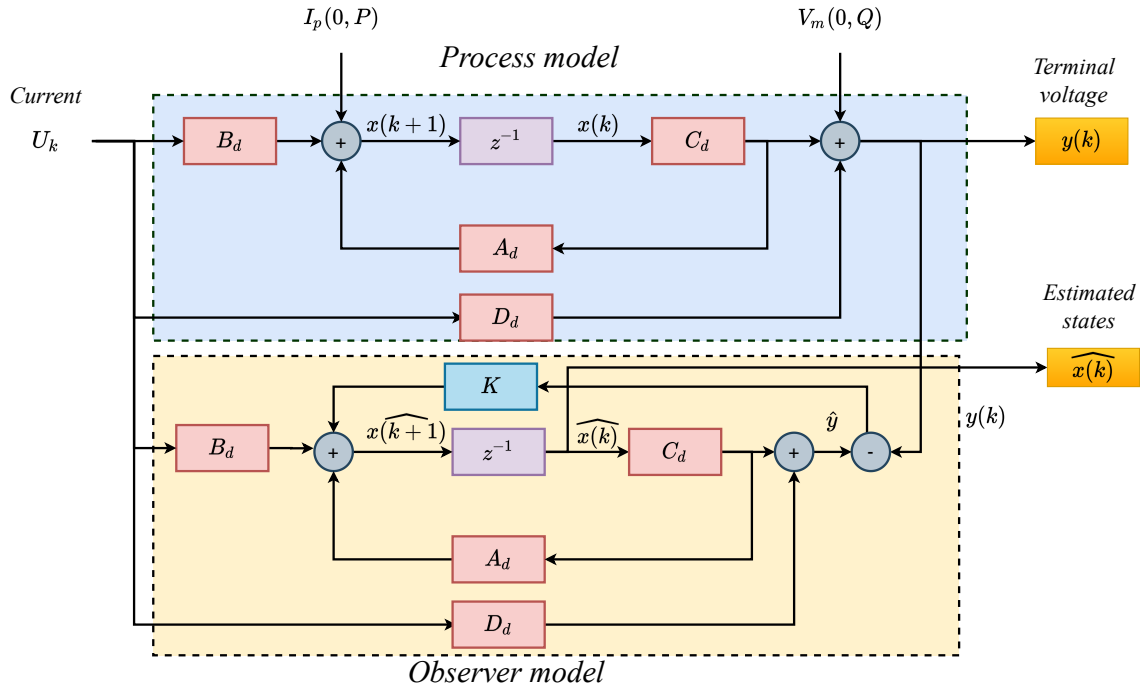
**Figure 3.31:** SOC estimation observer block model.

It is noticeable that none of the internal states $x$ are measurable in the model and thus we do not have any prior information about these states. Noise is considered as the additional inputs to the system, $I_p$ and $V_p$ are the noise due to the current and voltage sensors respectively. $I_p$ is added to the input current whereas $V_p$ is added to the output voltage. Here, $I_p$ and $V_p$ are considered to have it's mean at zero and are uncorrelated to each other, and thus $R_{12} = 0$. Its co-variances are $P$ and $Q$ respectively.

## Noise covariance matrix

According to the *central limit theorem*, the distribution of the disturbance/noise will be Gaussian if the distribution is due to many different sources where none of the sources is dominating or if the sources of distribution go to infinity. The Gaussian distribution for both the current and voltage sensor, as shown in figure 3.32 is made with one hour reading of the current sensor when it is discharging the cell at a constant current of $2\,\text{A}$ and one hour reading of the voltage sensor during the $CV$ mode by keeping the cell at $3.65\,\text{V}$. The covariance of the current sensor and voltage sensor is found by using

$$Cov(X) = Var(X) = \frac{1}{n}\sum_{i=1}^{n}(X_i - \mu)^2 \tag{3.39}$$

where, $\mu$ is the arithmetic mean of vector $X$. The values of the covariances for both the sensors is given in table 3.2.

**Table 3.2:** Noise covariances from current and voltage sensor are shown in the table. These two values will be used in forming the noise covariance matrix which is one of the inputs to the *SOC* estimation model.

| Description | Variable | Value |
|---|---|---|
| Process noise co-variance | $P$ | $1.35 \times 10^{-9}$ |
| Measurement noise co-variance | $Q$ | 0.0121 |
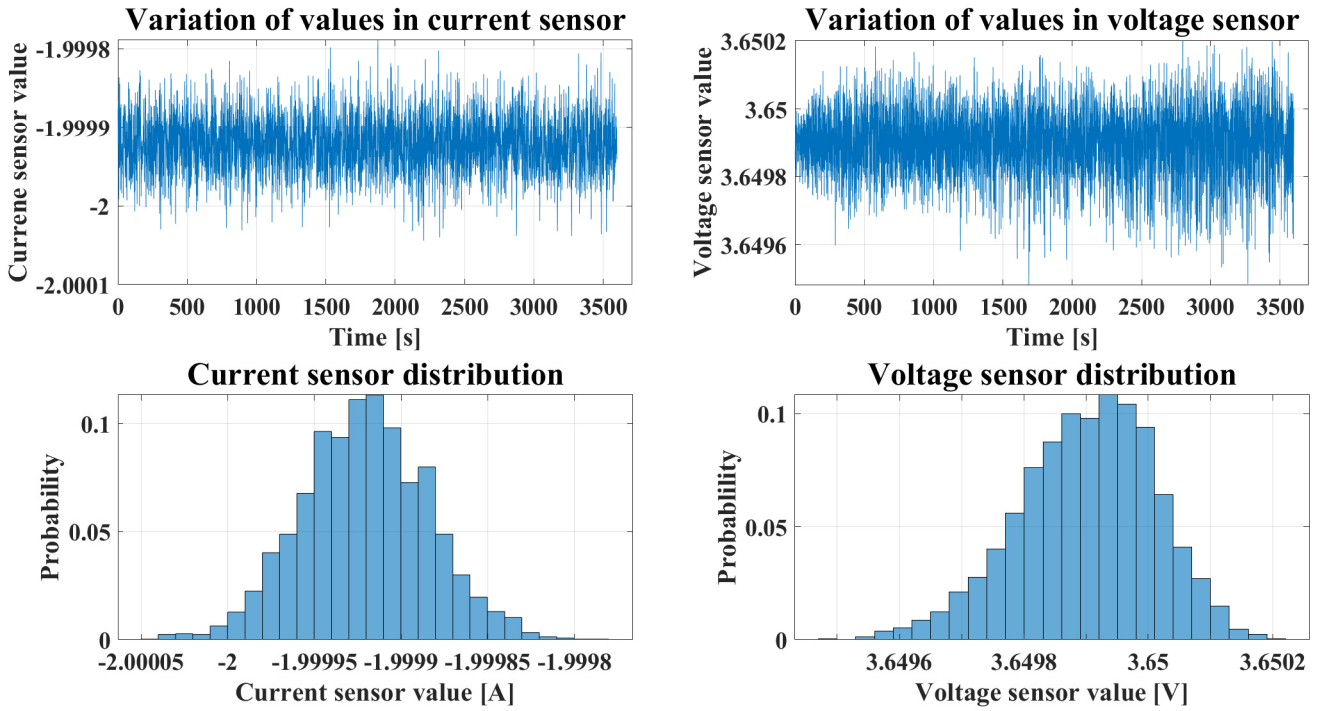


**Figure 3.32:** Process and measurement noise distributions.

## $R_1$, $R_2$ and $R$

The Noise due to current sensor adds to the input current and in (3.31) the state $V_{R_1 C_1}$ is directly influenced by the sum of input and disturbance $I + I_p$ and similarly from (3.32), the state $SOC$ is influenced by $(I + I_p)/3600$. Hence, the intensities $R_1$ and $R_2$ are written as,

$$R_1 = \begin{bmatrix} P \\ P \\ P \\ P/3600 \end{bmatrix} = \begin{bmatrix} 1.35 \times 10^{-9} \\ 1.35 \times 10^{-9} \\ 1.35 \times 10^{-9} \\ 3.73 \times 10^{-13} \end{bmatrix} \qquad R_2 = [Q] = [0.0121] \qquad (3.40)$$

The noise covariance matrix $R$ is given as,

$$
R = \begin{bmatrix} R_1 & R_{12} \\ R_{12}^T & R_2 \end{bmatrix} = \begin{bmatrix} 1.35 \times 10^{-9} & 0 & 0 & 0 & 0 \\ 0 & 1.35 \times 10^{-9} & 0 & 0 & 0 \\ 0 & 0 & 1.35 \times 10^{-9} & 0 & 0 \\ 0 & 0 & 0 & 3.73 \times 10^{-13} & 0 \\ 0 & 0 & 0 & 0 & 0.0121 \end{bmatrix}
$$

$$(3.41)$$

### 3.7.3 Modelling

The $EKF$ and $UKF$ are modelled in Simulink, where the process equation (3.33) and measurement equation (3.36) are used. The parameters for these two functions are provided by the cell model. Both the $EKF$ and $UKF$ need initial values of the states and the covariance matrix $P$ and it is given as

$$
x_0 = \begin{bmatrix} 0 \\ 0 \\ 0 \\ \widehat{SOC_{init}} \end{bmatrix} \quad P_0 = \begin{bmatrix} 10^{-4} \\ 10^{-4} \\ 10^{-4} \\ 0.01 \end{bmatrix}
$$

$$(3.42)$$

Here, the initial values of $V_{R_1C_1}$, $V_{R_2C_2}$ and $V_{R_3C_3}$ are assumed to be zero since there is no prior information available. The initial value $\widehat{SOC_{init}}$ is in between [0 1]. This value is selected such that it starts with the wrong value to see how quickly the estimated value of $SOC$ from both the filters converges to the actual $SOC$ value based on voltage measurement of the cell. To do this check, the WLTC current profile is given as the input to the cell model and the SOC estimation model. Voltage measurement from the experiment is given as the inputs to both of these models as shown in figures 3.33 and 3.34. Whereas, the initial noise co-variance matrix $P_0$ is selected such that an assumption of the maximum deviation of voltage is $10\,\mathrm{mV}$ and the maximum deviation in $SOC$ is 10% or 0.1. The relationship of variance $Var(x)$ and standard deviation $\sigma$ is given as,

$$
Var(x) = \sigma^2
$$

$$(3.43)$$

hence, the initial value of the covariance matrix is as shown in (3.42).The spread of the sigma points for the $UKF$ filter, is chosen based on the values of $\alpha, \beta$ and $\kappa$. It is chosen according to [51] and the values and description of these parameters are given in table 3.3. These three parameters affect the spread of the sigma points such that, if the values are higher then the sigma points are chosen far from the mean of the Gaussian random variable (GRV) and if the values are smaller then sigma points are selected near the vicinity of the mean.

**Table 3.3:** Selection of the $UKF$ parameters to select the spread of sigma points according to [51].

| Description | Variable | Value | Possible Range |
|---|---|---|---|
| Determines the spread of sigma points | $\alpha$ | 1 | (0 1] |
| To incorporate prior knowledge of the distribution | $\beta$ | 2 | 2 is optimal choice for Gaussian |
| Secondary scaling parameter | $\kappa$ | 0 | $\geq 0$ |

In this thesis, both the $EKF$ and $UKF$ is implemented using the Simulink blocks as shown in figure 3.33. The $EKF$ and the $UKF$ blocks take the measured voltage as the input and provide the estimated states as the output. The blocks has the provision to enter $R_1$, $R_2$, $x_0$ and $P_0$. Both blocks make use of the same measurement and process function for the computation. $UKF$ block has the options to enter the parameters $\alpha$, $\beta$ and $\kappa$ to select the spread of sigma points.
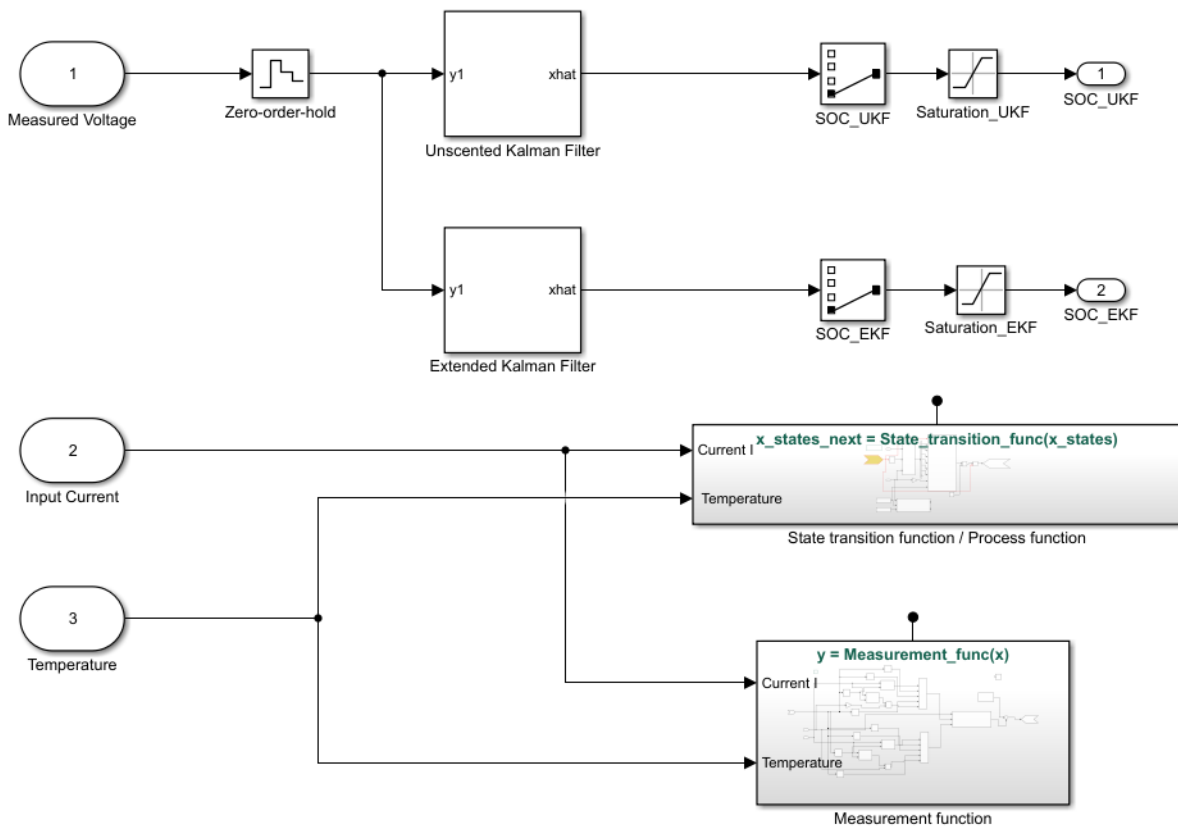


**Figure 3.33:** SOC estimation modelling in Simulink.

The process and measurement function is made based on (3.33) and (3.36). The parameters for the functions is provided by the cell model.
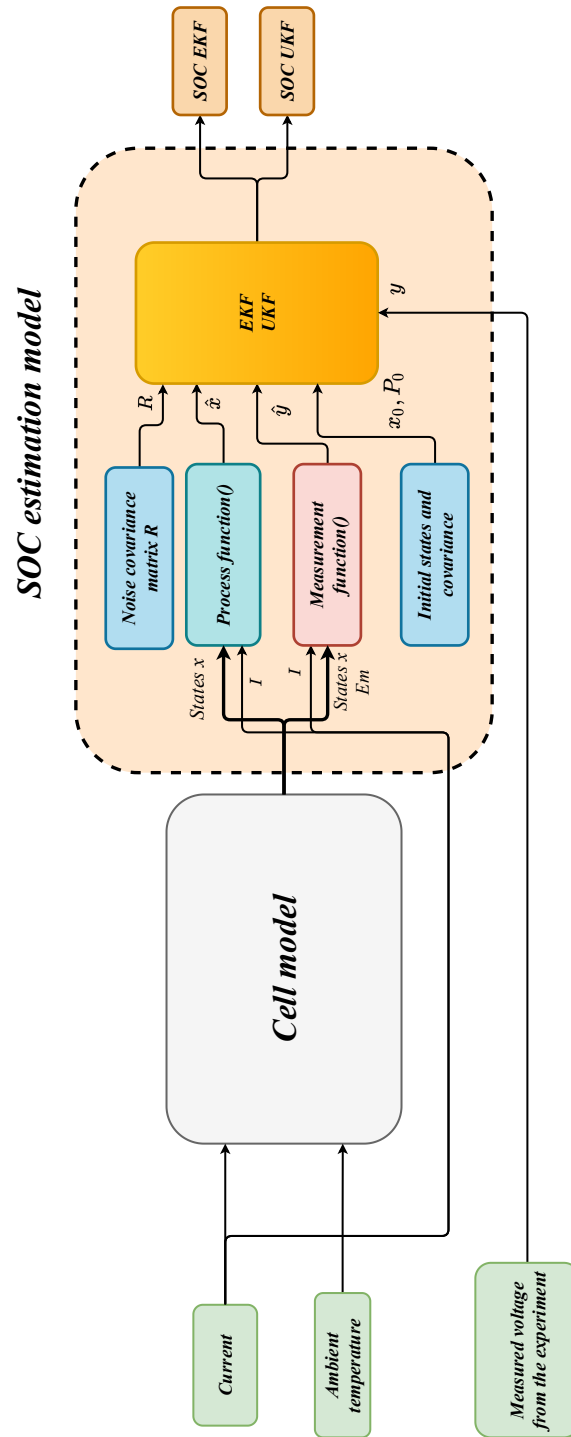
**Figure 3.34:** SOC estimation model

# 4

# Results

In this chapter, the results for the electrical and thermal model. The drive cycle validation results and *SOC* estimation model results will be presented in detail.

## 4.1 Preliminary tests

In this thesis project, an LFP prismatic cell is used and its details are already mentioned in section 3.1. Before starting the tests for electrical and thermal characterisation, it is important to know the characteristic behaviour of the cell. Also, it is important to know if the characteristic behaviour among similar cells is consistent with each other. For this test, the setup mentioned in figure 3.1 is used.

### 4.1.1 1C charge-discharge test

The similarities among the cells have been checked by testing two cells out of three. Their charging and discharging behaviours are compared and they show almost similar behaviour. The discharge and charging voltage curve v/s *SOC* is used to determine the current pulse width for pulse charge and discharge test which is discussed in detail in the next section.

The cells are discharged and charged at $1C$ $(20\,\mathrm{A})$ and the steps followed for the tests are as follows:
1. Two cells are initially charged to $V_{max} = 3.65\,\mathrm{V}$ at constant current of $10\,\mathrm{A}$ and kept at potentiostatic mode until the magnitude of the current reduces to $1\,\mathrm{mA}$.
2. After resting the cells for 20 minutes, the cells are discharged to $V_{min} = 2.8\,\mathrm{V}$ at 1C $(20\,\mathrm{A})$ and kept at constant voltage mode until the magnitude of current drops to $1\,\mathrm{mA}$.
3. After resting the cells for 20 minutes, the cells are charged to $V_{max} = 3.65\,\mathrm{V}$ at 1C $(20\,\mathrm{A})$ and kept at the potentiostatic mode until the magnitude of the current drops to $1\,\mathrm{mA}$.
4. Steps 2 and 3 are repeated once more, to have two cycles of charging and discharging of the cells.

After running the mentioned test sequence, the test results of cell 1 is as shown in figure 4.1. As the charge and discharge current is applied to the cell, the temperature of the cell increases. The temperature at the terminal of the cell is marginally higher than that of the surface. Hence, if the terminal temperature reaches the temperature

limit (45 °C), the test is programmed to stop. There could be three possible reasons for this behaviour:

- The temperature sensor at the terminal is separated by Kapton tape. The temperature sensor at the surface is separated by insulation (green cover) from the surface of the cell. This cover on the surface could have more thermal resistance than the Kapton tape. This will not be verified in this thesis work.
- The Positive current collector (Aluminium) has lesser electrical conductivity when compared to that of a negative current collector (Copper), hence it offers higher resistance, this, in turn, generates higher temperatures at the positive terminal.
- Since the entire setup is near the fans of the Neware battery tester, fans from the equipment are blowing air on the surface. Hence, the surface is losing more heat. Terminal temperature sensors are not in the direct path of the airflow.
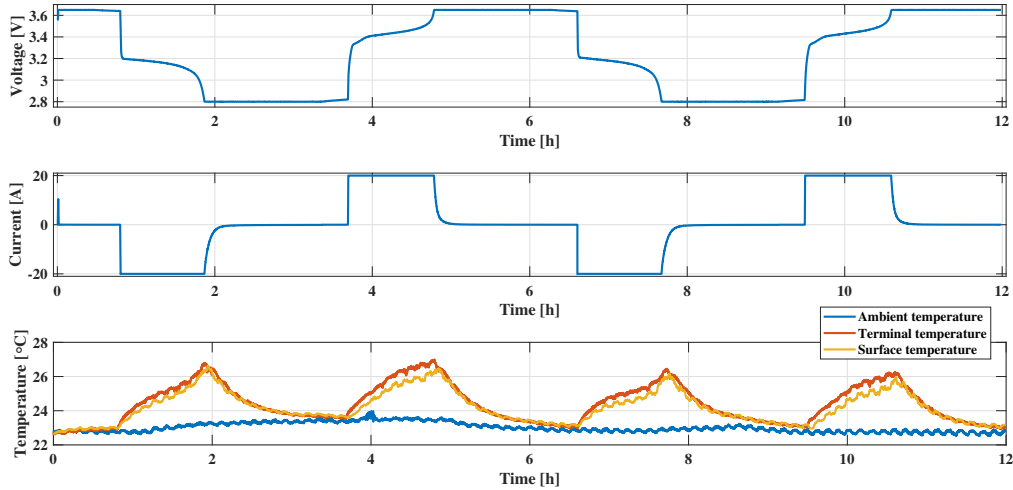


**Figure 4.1:** Measured voltage, current and temperature of *Cell* 1 during the discharge and charge test.

From figure 4.2, it can be observed that the charging and discharging curves of both cells and for two cycles are similar without major variations. Also, charging and discharging capacities are calculated as are shown in table 4.1. The charge-discharge capacities between the two cycles and the two cells are similar, but the capacities are higher compared to the specification. From these results, it is easy to conclude that the two cells are consistent with each other and for further tests, any one of these two cells can be selected.

## 4.2   Electrical characterisation

After a 1C charge and discharge tests on two cells, it is decided to use *Cell*1 for electrical characterisation. To extract parameters for the EECM, pulse discharge and charge tests are done. This section will explain the results from these tests and model results after extracting the parameters.

**Table 4.1:** Charging and discharge capacities of two cells for two cycles.

|  | Cell 1 | Cell 2 |
|---|---|---|
| **Discharge capacity - first cycle** | 22.67 A h | 22.52 A h |
| **Charge capacity - first cycle** | 22.69 A h | 22.53 A h |
| **Discharge capacity - second cycle** | 22.73 A h | 22.53 A h |
| **Charge capacity - second cycle** | 22.73 A h | 22.53 A h |
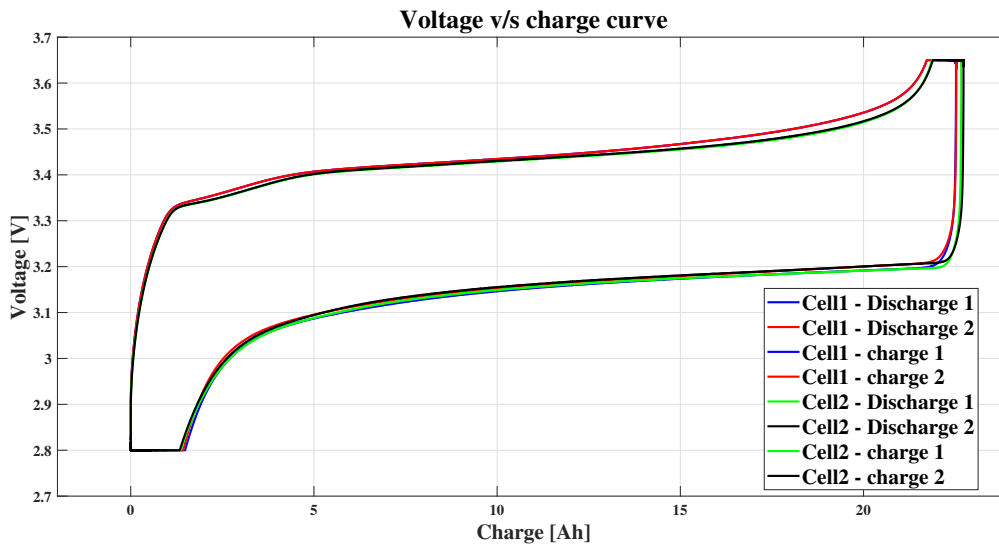


**Figure 4.2:** Voltage v/s charge curves of two cells for both the cycles

## 4.2.1 Pulse discharge - Charge test

In pulse discharge - charge test, discharge and charge current pulses with defined width and magnitude are applied to the cell at constant ambient temperature conditions. The magnitude of these current pulses is decided to be kept at $1C = 20$ A. To decide the width of the pulses, a second cycle from 1C discharge-charge voltage v/s $SOC$ curve of the cell without a potentiostatic step is used as a reference as shown in figure 4.3. To calculate the $SOC$, the discharge and charge capacities are considered without the potentiostatic step and the values are 21.38 A h and 21.90 A h respectively.

### 4.2.1.1 Discharge current profile

To decide pulses for the discharge test, the discharge voltage profile as shown in figure 4.4 is used. This discharge curve can be split into three regions. They are high $SOC$, mid $SOC$ and low $SOC$ regions.

In the discharge voltage profile, from 0 % to 8 % $SOC$ interval, the change in voltage is significant and this $SOC$ range is the low $SOC$ region. The voltage remains
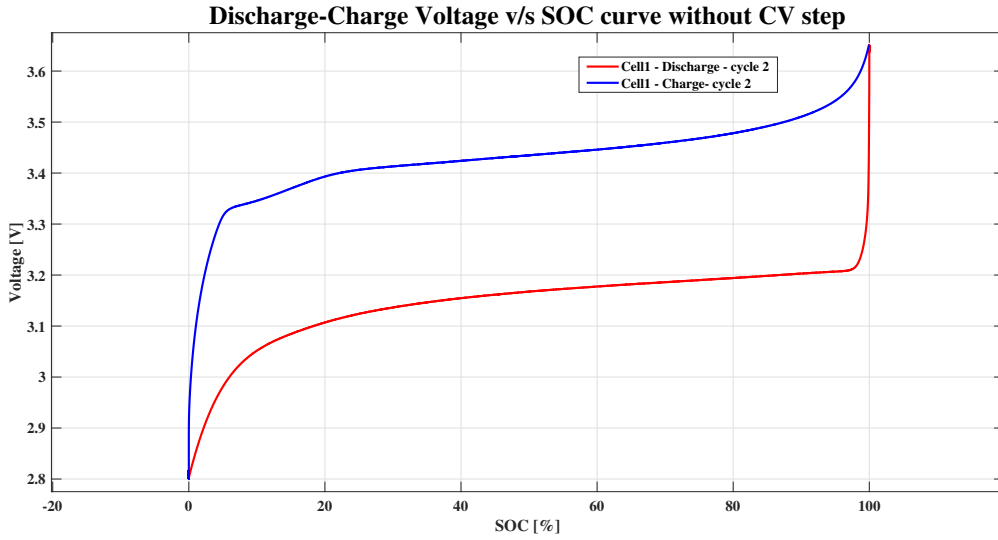
**Figure 4.3:** Discharge-Charge Voltage v/s $SOC$ curves of $Cell1$ for second cycle without potentiostatic step

almost flat from $8\%$ to $98\%$ $SOC$ and this is the mid $SOC$ region. Finally, the change in voltage is significant from $98\%$ to $100\%$ and this $SOC$ interval is named as high $SOC$ region. The number of pulses in each of these $SOC$ regions is selected as shown in table 4.2. The pulse width depends on the percentage of the capacity needed to be discharged by the current. The time for the pulse is calculated by the expression,

$$Time_{pulse} = \frac{C_{discharge}}{20\,\text{A}} \times \frac{PW_{discharge}}{100} \times 3600 \tag{4.1}$$

where $C_{discharge} = 21.38\,\text{A h}$ is the discharge capacity of the cell without the CV step, $PW_{discharge}$ is the pulse width in percentage. The time calculated for different pulse widths are shown in table 4.2. The calculated time is rounded off to the next second.

**Table 4.2:** Number of pulses in different $SOC$ regions for discharge pulse test

| $SOC$ region | $SOC$ interval | Number of pulses | Pulse width | Calculated time for each pulse width |
|---|---|---|---|---|
| **Low** | $0\%$ - $8\%$ | 2 | $4\%$ | $154\,\text{s}$ |
| **Mid** | $8\%$ - $98\%$ | 9 | $10\%$ | $385\,\text{s}$ |
| **High** | $98\%$ - $100\%$ | 1 | $2\%$ | $77\,\text{s}$ |

The current profile for the discharge pulse test is as shown in figure 4.5. The cell is relaxed for $1\,\text{h}$ after every pulse.
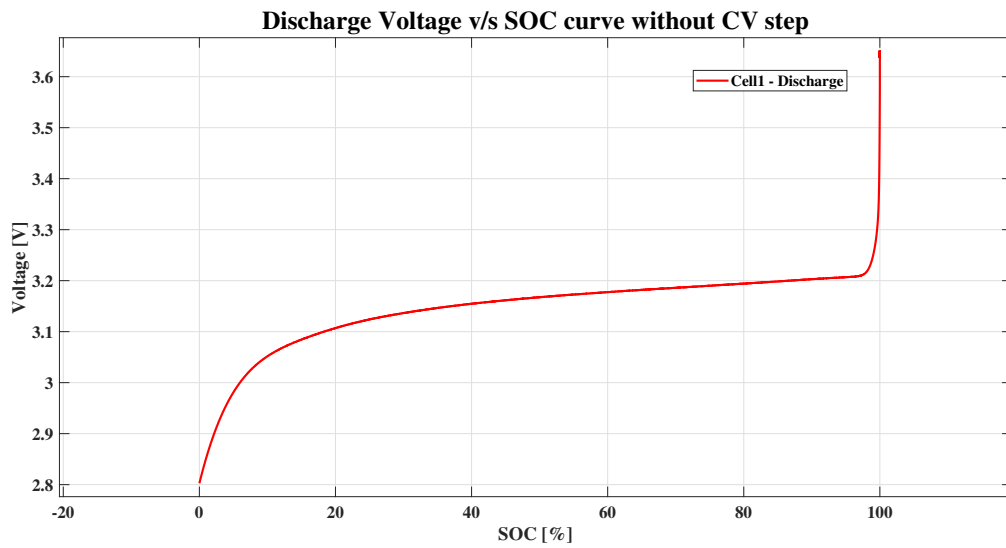
**Figure 4.4:** Discharge Voltage v/s *SOC* curves of *Cell*1 for second cycle without potentiostatic step
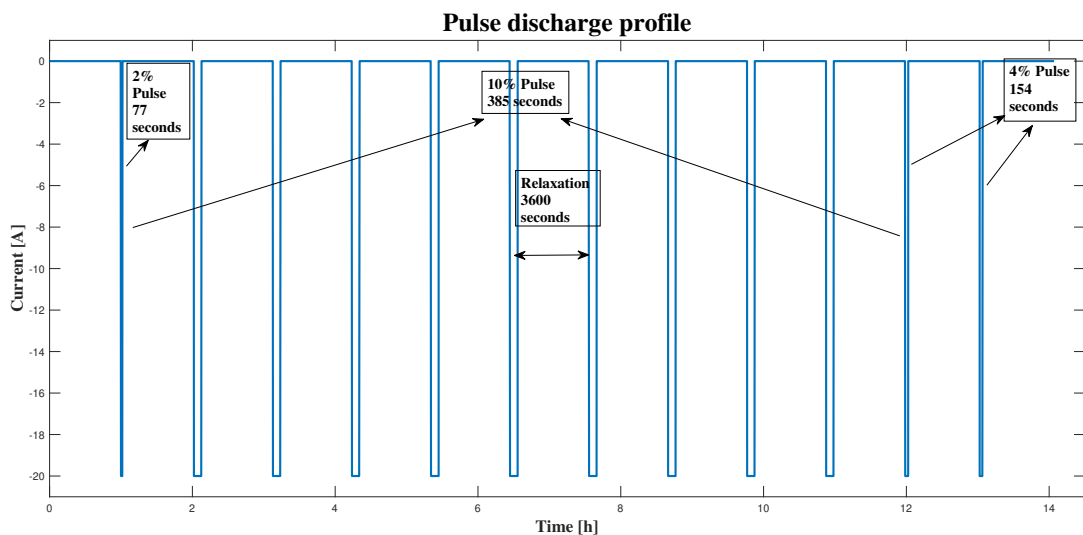


**Figure 4.5:** Discharge pulses current profile

### 4.2.1.2 Charging current profile

To decide the pulses for the pulse charge test, the charging voltage profile is chosen as reference (as shown in figure 4.6). Even this charging voltage curve is identified into three *SOC* regions as it was done for the discharge voltage curve.

In the charging voltage profile, the low *SOC* region is identified from 0 % to 6 % as a change in voltage is significant. Middle *SOC* region is from 6 % to 96 % as voltage remains almost flat and high *SOC* region is identified from 96 % to 100 % as a change in voltage is most significant. The number of pulses in each of these *SOC* regions are selected as shown in table 4.3. For calculating the time for charging

pulses, the following expression is used,

$$Time_{pulse} = \frac{C_{charging}}{20\,\text{A}} \times \frac{PW_{charging}}{100} \times 3600 \qquad (4.2)$$

where $C_{charging} = 21.9027\,\text{A h}$ is the charge capacity of the cell without the potentiostatic step. $PW_{charging}$ is the pulse width in percentage. The time calculated for different pulse widths are shown in table 4.3. The calculated time is rounded off to the next second.
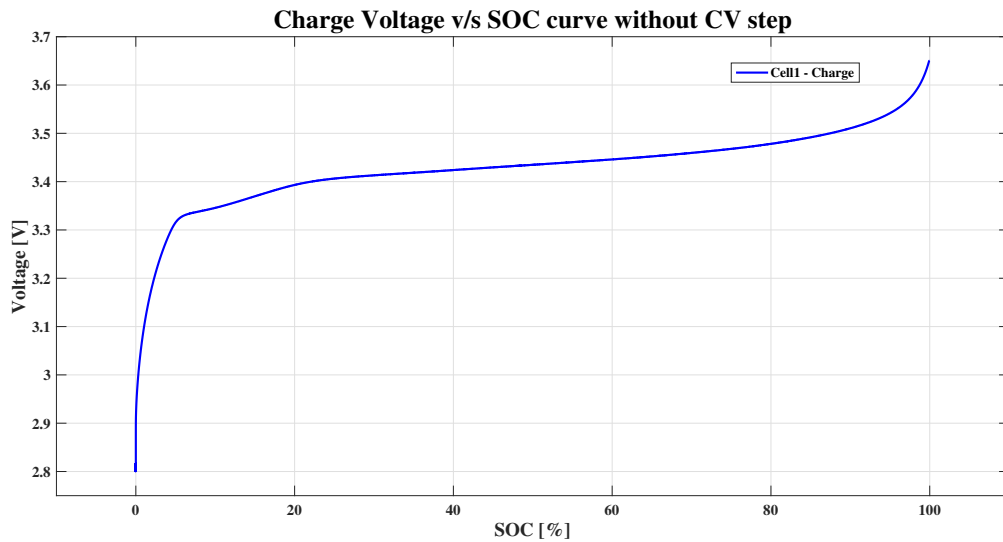
**Table 4.3:** Number of pulses in different $SOC$ regions for charging pulse test

| $SOC$ region | $SOC$ interval | Number of pulses | Pulse width | Calculated time for each pulse width |
|---|---|---|---|---|
| **Low** | 0 % - 6 % | 3 | 2 % | 79 s |
| **Mid** | 6 % - 96 % | 9 | 10 % | 394 s |
| **High** | 96 % - 100 % | 1 | 4 % | 157 s |



**Figure 4.6:** Charge Voltage v/s $SOC$ curves of $Cell1$ for second cycle without potentiostatic step

The current profile for the discharge pulse test is as shown in figure 4.7. The cell is relaxed for 1 h after every pulse.
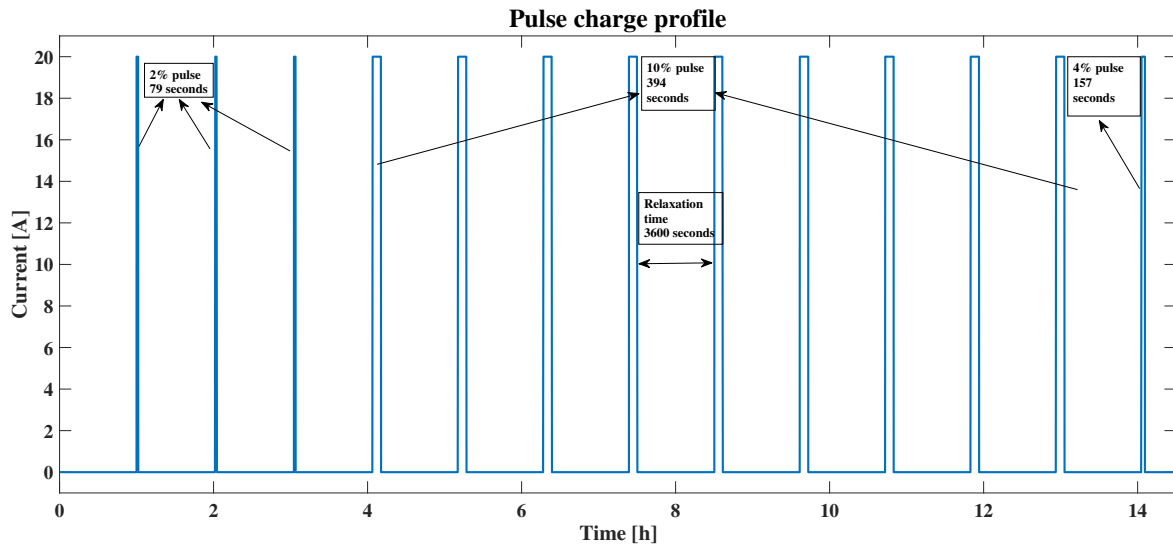
**Figure 4.7:** The current profile for charging pulses.

#### 4.2.1.3    Test results

Pulse discharge-charge tests are done at four different ambient temperatures. The test is done at 10 °C, room temperature, 30 °C and 40 °C. For the test done at room temperature the same setup used for 1C charge-discharge test as shown in figure 3.1. For tests done at 10 °C, 30 °C , and 40 °C, the entire setup is placed inside a temperature chamber to maintain constant ambient temperature as shown in figure 4.8. Since ambient temperature is already known inside the temperature chamber, an additional temperature sensor for measuring ambient temperature isn't used and only surface and the terminal temperature is measured.

For safety reasons, voltage limits are given in the program. If the voltage measured across the terminals are lower than $V_{LowLimit}$ or higher than $V_{HighLimit}$, then the program goes to the next step. In this test, the current goes to zero. Before starting a pulse discharge, the cell is charged to 100 % $SOC$ using a constant current of 10 A until the cell reaches $V_{max}$ =3.65 V. It is kept at the potentiostatic mode until current drops to less than 1 mA.

Similarly, for pulse charge test cell is discharged to 0 % $SOC$ using constant current of 10 A until the cell reaches $V_{min}$=2.8 V. It is kept at the potentiostatic mode until current drops to less than 1 mA.
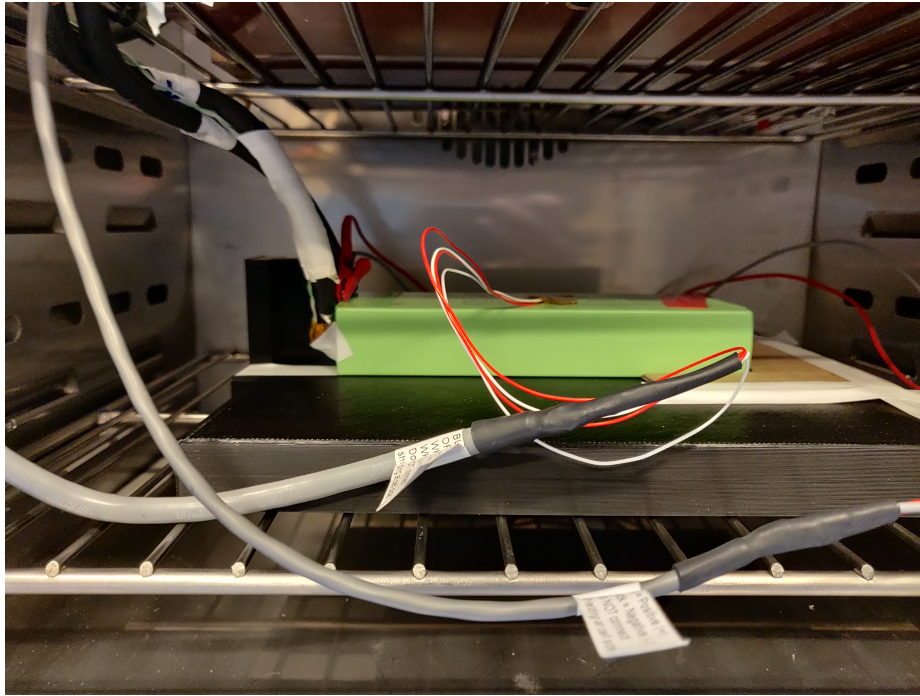
**Figure 4.8:** Test setup placed inside temperature chamber for tests done at $10\,°C$, $30\,°C$ and $40\,°C$
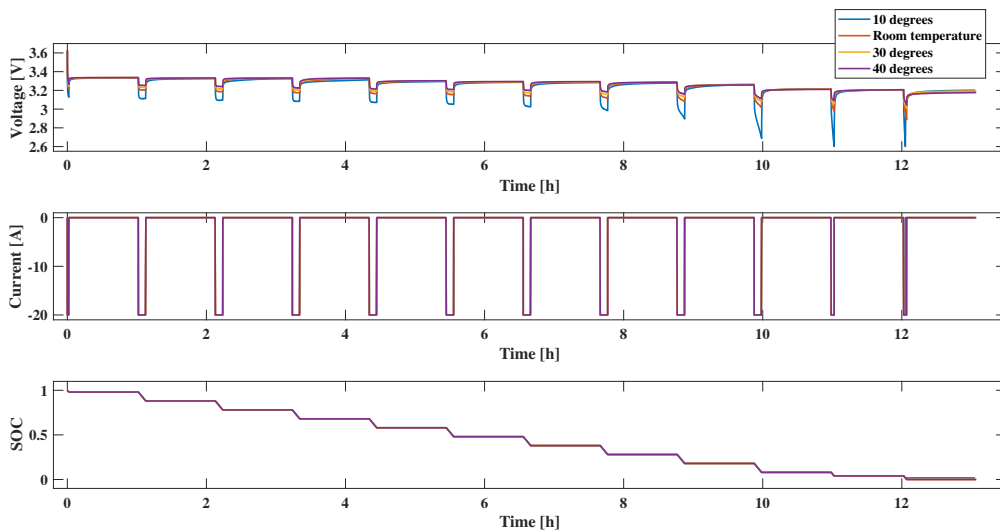


**Figure 4.9:** Test output for pulse discharge test.

The test output for the pulse discharge test is shown in figure 4.9. As a result, it is possible to observe the voltage response for the discharge current pulses. Also, $SOC$ reduces during the application of the current pulse from $100\,\%$ to $0\,\%$. At lower temperatures, the internal resistance is higher when compared to the resistance at a higher temperature. This is due to the conductivity of the electrolyte. Electrolytic conductivity increases as the temperature increases. Resistance is inversely proportional to conductivity and hence higher over potential for the entire $SOC$ region as

the temperature decreases.

At 10 °C, the voltage goes to $V_{LowLimit}$ before the duration of pulse finishes and the program goes to the next step (i.e relaxation phase). This happens twice for the final two pulses at low $SOC$ and can be observed in figure 4.10.



**Figure 4.10:** Voltage response reaching $V_{LowLimit}$ before the completion of pulse at low $SOC$ interval

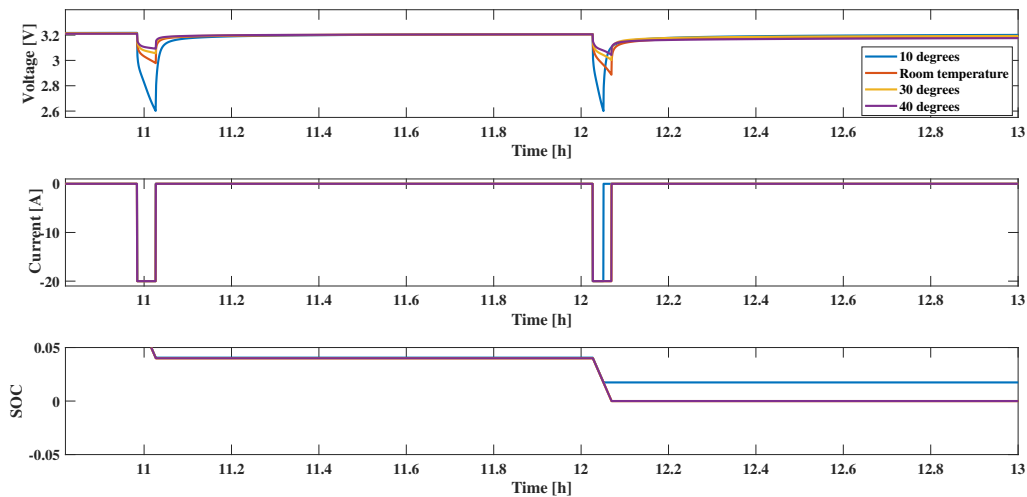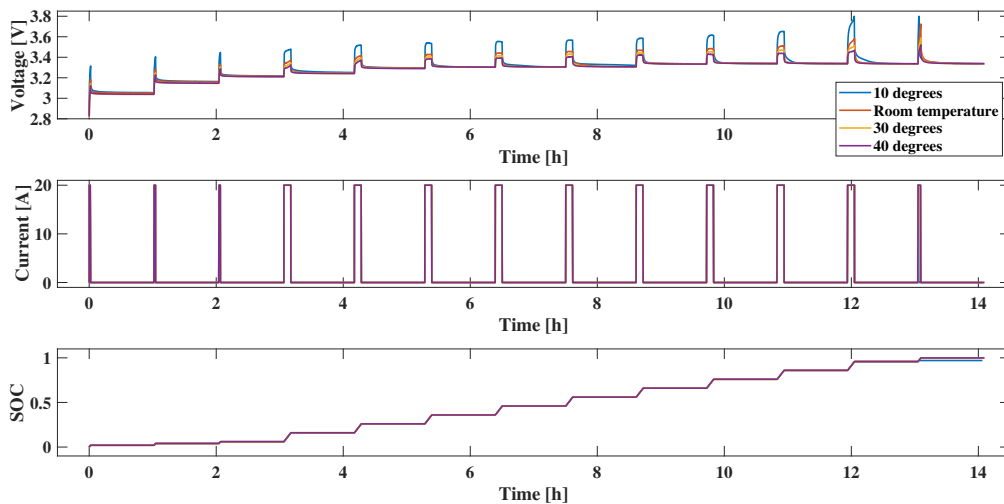

**Figure 4.11:** Test output for pulse charge test.

The test output for the pulse charge test is shown in figure 4.11. Similar to the result discussed for the pulse discharge test, at lower temperatures higher over potential can be witnessed throughout the $SOC$ regions during the pulse charge test and the

voltage reaches $V_{HighLimit}$ at higher $SOC$ interval before completion of the charging current pulse. This happens for the final two pulses as shown in figure 4.12.
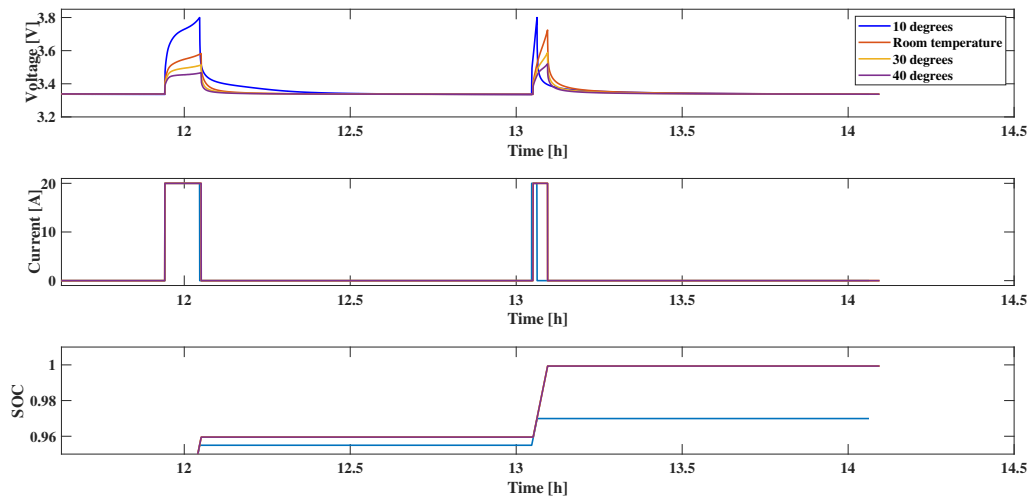


**Figure 4.12:** Voltage response reaching $V_{HighLimit}$ at high $SOC$ interval.

### 4.2.2 Points of load and relaxation

Identifying the points of load and relaxation is critical for extracting parameters from the voltage response curves of the pulse discharge-charge tests for the EECM model. Accurate identification of these points helps in getting a better calculation of $Em$, $R_0$, $R_x$ and $C_x$.

The value of $R_0$ is found by using (3.3). The value of $R_0$ can be found either during the falling edge or rising edge of the current pulse. It is found by the Instantaneous voltage difference between the point of load and relaxation divided by the magnitude of the current.
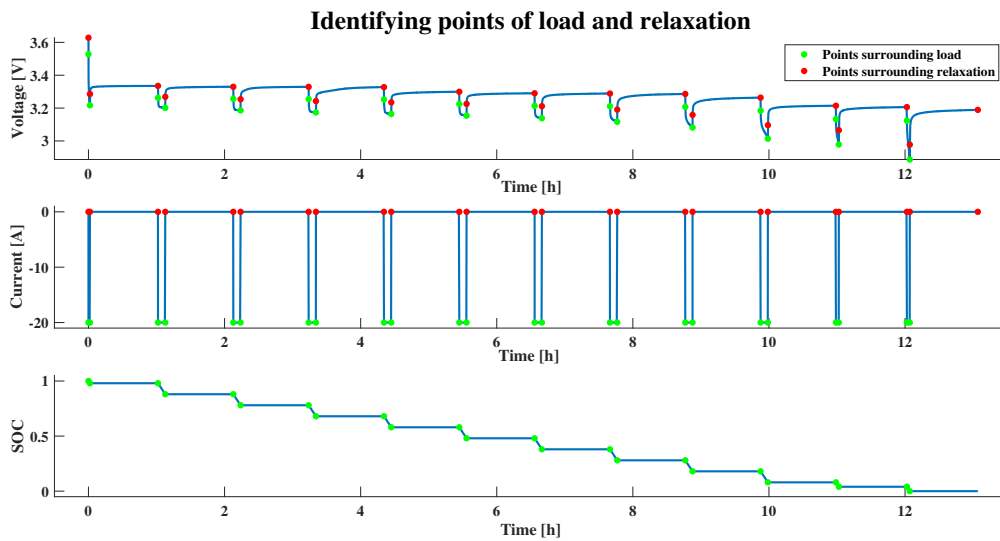
**Figure 4.13:** Identifying points of load and relaxation for pulse discharge test at room temperature.

Identification of points of load and relaxation for discharging and charging pulses are shown in figures 4.13 and 4.14 respectively. Points of load are the points identified when the magnitude of the current is 20 A and points of relaxation is when current is zero or when the cell is relaxing. An increase or decrease in *SOC* happens between the points of load.
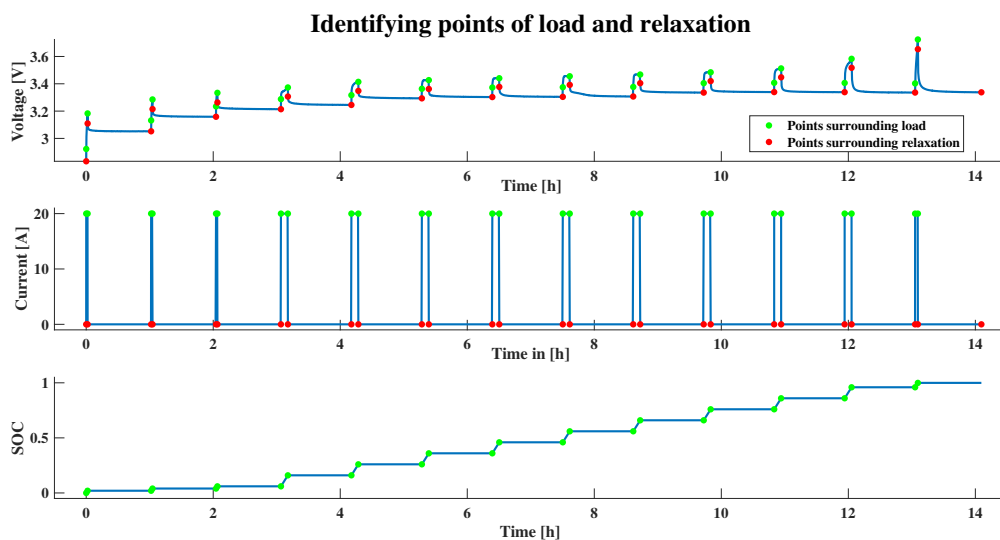


**Figure 4.14:** Identifying points of load and relaxation for pulse charge test at room temperature.

### 4.2.3 Selection of $RC$ pairs

For EECM, $3RC$ links are best suited for both pulse discharge and charge voltage response curves during relaxation. This can be seen in figures 4.15 and 4.16. The

RMS Error (RMSE) between the $RC$ links and the voltage curve is least with $3RC$ links when compared to $2RC$ links for all the exponential rising voltage curves during relaxation.

Voltage curves are selected between the two points of relaxation in figures 4.13 and 4.14. To fit the curve, (3.1) and (3.2) are used in Matlab curve fitting toolbox [47]. In exponential rising or falling curves in figures 4.15 and 4.16, there are three time-constants for $3RC$ links. Three time constants represent how fast the curves rise after discharge current pulse or fall after charge current pulse.

After curve fitting for all the curves the range for these time constants can be observed and is shown in table 4.4. These ranges help use it as limits during parameter estimation which is discussed in the next section.

**Table 4.4:** Range for time constants.

| $\tau$ | Time interval |
|--------|---------------|
| $\tau(1)$ | $0.1\,\mathrm{s}$ to $50\,\mathrm{s}$ |
| $\tau(2)$ | $50\,\mathrm{s}$ to $200\,\mathrm{s}$ |
| $\tau(3)$ | $200\,\mathrm{s}$ to $3600\,\mathrm{s}$ |
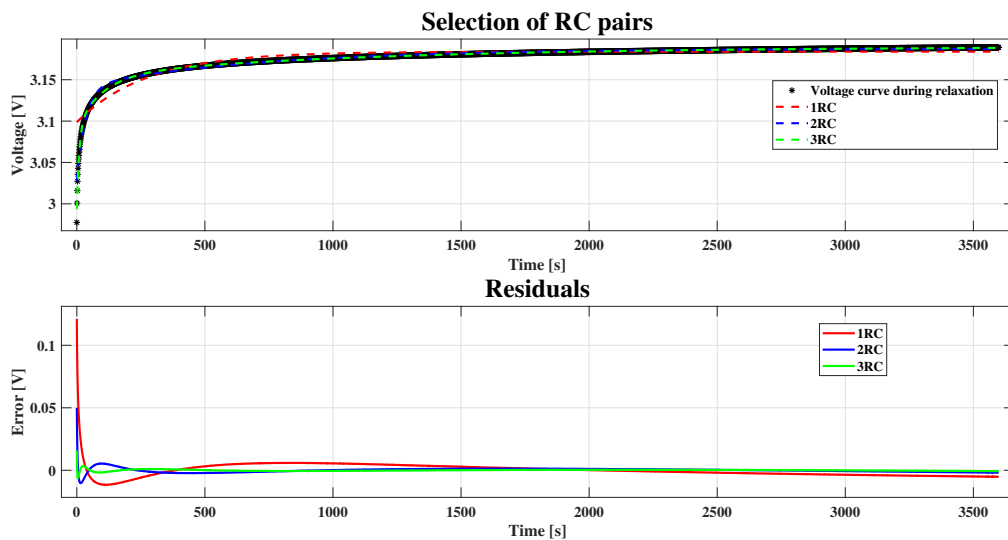


**Figure 4.15:** Voltage curve during relaxation after discharge current pulse, fitted using $1RC$, $2RC$ and $3RC$ exponential equations with the help of Matlab curve fitting tool box [47].
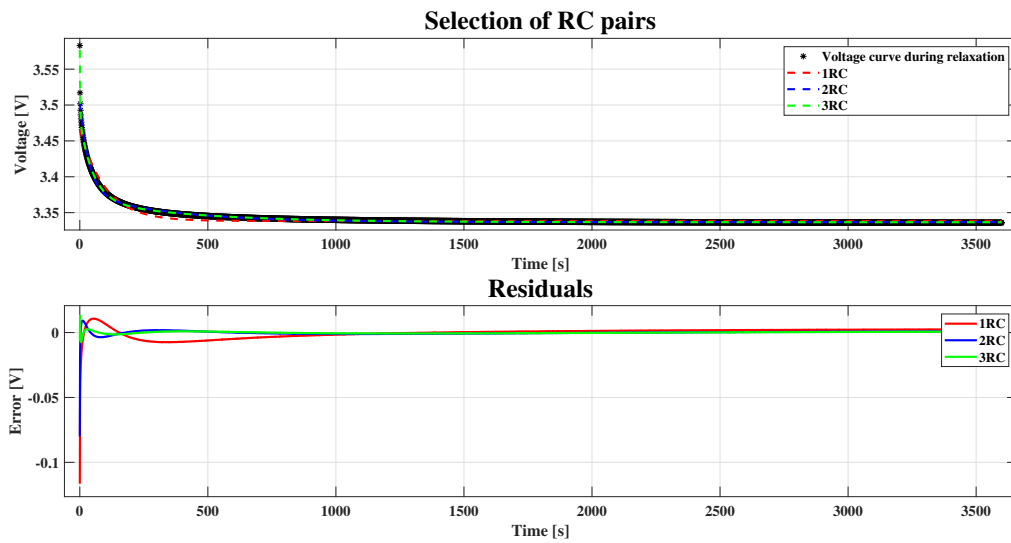
**Figure 4.16:** Voltage curve during relaxation after charge current pulse , fitted using $1RC$, $2RC$ and $3RC$ exponential equations with the help of Matlab curve fitting tool box [47].

## 4.2.4 Parameterization of $Em$, $R0$, $Rx$ and $Cx$

After accurate curve fitting, it is easy to extract parameters for the EECM. Exponential curve fitting for every pulse gives the values of $a_0$, $a(1)$, $a(1)$, $a(1)$, $\tau(1)$, $\tau(2)$ and $\tau(3)$. By using (3.4), (3.5) and (3.6) the values of $Em$, $R_1$, $R_2$, $R_3$, $C_1$, $C_2$ and $C_3$ are calculated. 2-D lookup table is made for all these parameters with respect to SOC breakpoints ($SOC$ at the end of relaxation). These lookup tables are fed to the EECM Simulink model (figure 3.8).
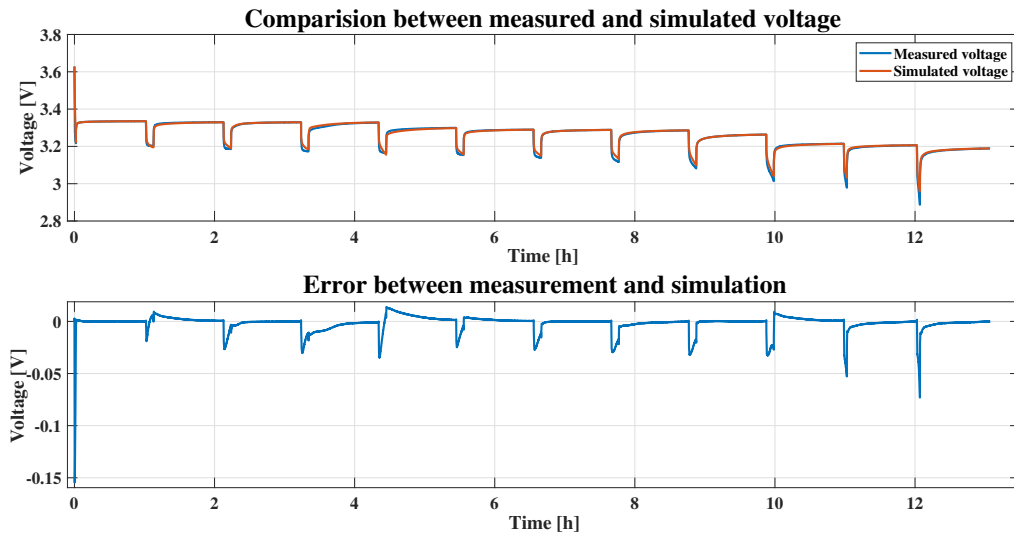
**Figure 4.17:** Comparison between measured and simulated voltage for pulse discharge test at room temperature

For the pulse discharge and charge test, a comparison between measured and model voltages are shown in figures 4.17 and 4.18. The simulated voltage has a good fit with respect to the measured voltage except at low *SOC* and high *SOC* regions.



**Figure 4.18:** Comparison between measured and simulated voltage for pulse charge test at room temperature

To further optimise the parameters for better performance of the model, parameter estimation in Simulink is executed. The limits for the parameters are defined in table 4.5. The parameter estimation algorithm varies these parameters within these limits to minimise the sum of squared error between the measured and simulated voltage using the non-linear least square method.

The limits for $Em$ is selected based on $V_{LowLimit}$=2.6 V and $V_{HighLimit}$=3.8 V. Limits for time constants $\tau_1$, $\tau_2$ and $\tau_3$ are selected based on observations made during the exponential curve fitting as mentioned in table 4.4. Limits for the resistances $R_0$, $R_1$, $R_2$ and $R_3$ are based on a reasonable assumption of its value in the cell, which is in the order of a few m$\Omega$. To avoid restricting the range of resistance to a narrow range, a bigger range of 0.1 m$\Omega$ and 1 $\Omega$ is chosen.

**Table 4.5:** Limits of the parameters given for parameter estimation

| Parameter | Minimum | Maximum |
|-----------|---------|---------|
| $Em$ | 2.6 V | 3.8 V |
| $R_0$ | 0.1 m$\Omega$ | 1 $\Omega$ |
| $R_1$ | 0.1 m$\Omega$ | 1 $\Omega$ |
| $\tau_1$ | 0.1 s | 50 s |
| $R_2$ | 0.1 m$\Omega$ | 1 $\Omega$ |
| $\tau_2$ | 50 s | 200 s |
| $R_3$ | 0.1 m$\Omega$ | 1 $\Omega$ |
| $\tau_3$ | 200 s | 3600 s |

After parameter estimation, the comparison between the measured and simulated voltage for pulse discharge and charge tests are shown in figures 4.19 and 4.20. Parameter estimation has optimised the parameters to a major extent and minimised the error between measurement and simulation.
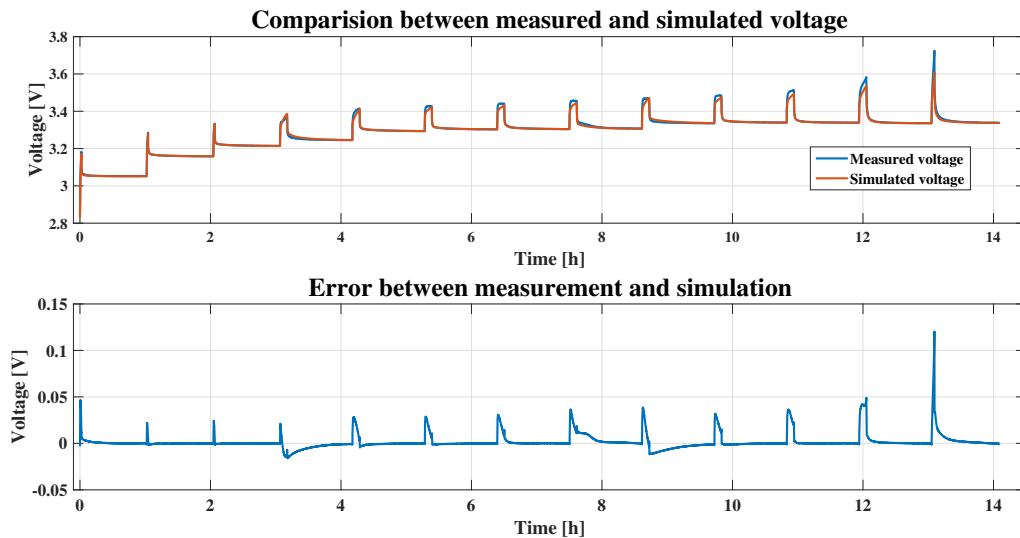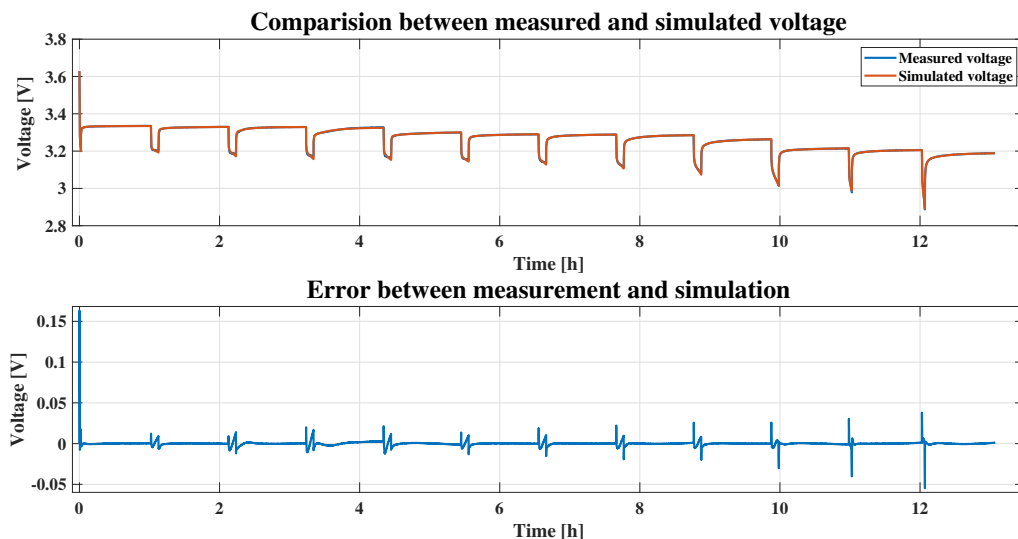


**Figure 4.19:** Comparison between measured and simulated voltage for the pulse discharge test at room temperature after optimising the parameters using parameter estimation.
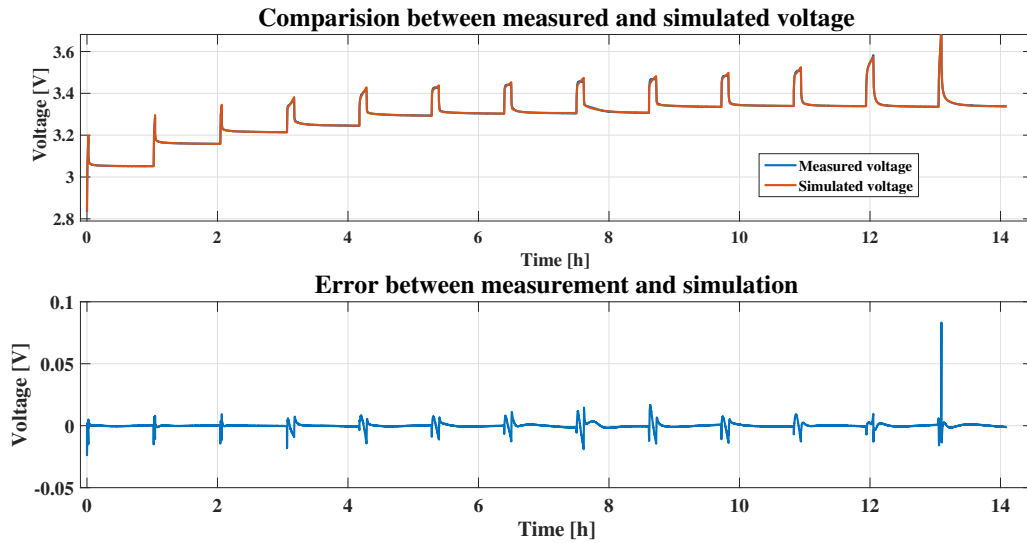
**Figure 4.20:** Comparison between measured and simulated voltage for the pulse charge test at room temperature after optimising the parameters using parameter estimation.

Table 4.6 shows the RMSE between measurement and simulation of each step during parameter estimation done for all temperatures. The RMSE is reducing after every step except at 10 °C. The error doesn't seem to be reduced even after the parameter estimation steps. But that is not the case. It is logical to consider only the flat voltage region of the cell for analysis and neglect high and low *SOC* regions. The high and low *SOC* regions have more errors due to a large voltage change for small *SOC* intervals. This induces more errors and is unimportant from the application point of view. Hence, the RMSE error between 8 % to 98 % *SOC* at 10 °C is checked and can be seen that the modelling is good even for a low temperature. As the temperature increases, the RMSE between measurement and simulation decreases.

**Table 4.6:** RMSE between measurement and simulation - Pulse discharge test.

| **Step** | 10 °C | 23.6 °C | 30 °C | 40 °C |
|---|---|---|---|---|
| Before Parameter estimation | 20.09 mV | 8.50 mV | 9.56 mV | 5.25 mV |
| Parameter estimation - $Em$, $R_0$ | 19.72 mV | 3.13 mV | 2.71 mV | 2.84 mV |
| Parameter estimation - $R_x$, $\tau_x$ | 19.70 mV | 2.27 mV | 2.07 mV | 2.27 mV |
| Parameter estimation - $Em$, $R_0$, $R_x$, $\tau_x$ | 19.06 mV | 2.26 mV | 1.88 mV | 1.99 mV |
| | | | | |
| RMSE between 8 % to 98 % *SOC* | 5.25 mV | 2.10 mV | 1.69 mV | 1.68 mV |

As the temperature increases, the magnitude of error also decreases and it can be seen in table 4.7. Due to large over-potential at a lower temperature, the error is larger and vice versa at higher temperatures. The minimum and maximum value of error in the mid *SOC* region is given. These errors are during the transition of voltage when the discharge current is applied. This minimum and maximum values

give the possible range for the error. The error range reduces as the temperature increases.

**Table 4.7:** Minimum and maximum error between measurement and simulation - Pulse discharge test between $8\,\%$ to $98\,\%$ *SOC*.

| Temperature | Minimum error | Maximum error |
|---|---|---|
| $10\,°C$ | $-214.11\,mV$ | $178.10\,mV$ |
| $23.6\,°C$ | $-30.23\,mV$ | $25.85\,mV$ |
| $30\,°C$ | $-22.72\,mV$ | $26.43\,mV$ |
| $40\,°C$ | $-9.04\,mV$ | $16.19\,mV$ |

A similar trend can be observed with the RMSE between the measured and simulated voltage of the pulse charge test as shown in table 4.8. The RMSE decreases after every step except at $10\,°C$. The RMSE at the middle *SOC* region is lower than that of the entire region for $10\,°C$. As the temperature increases, the RMSE decreases. Minimum and maximum errors in the middle *SOC* region are shown in table 4.9. The error range decreases as the temperature increases.

**Table 4.8:** The RMSE between measurement and simulation - Pulse charge test.

| Step | $10\,°C$ | $23.8\,°C$ | $30\,°C$ | $40\,°C$ |
|---|---|---|---|---|
| Before Parameter estimation | $25.64\,mV$ | $8.35\,mV$ | $7.53\,mV$ | $4.61\,mV$ |
| Parameter estimation - $Em$, $R_0$ | $24.62\,mV$ | $5.95\,mV$ | $5.72\,mV$ | $3.12\,mV$ |
| Parameter estimation - $R_x$, $\tau_x$ | $26.57\,mV$ | $3.32\,mV$ | $2.51\,mV$ | $1.97\,mV$ |
| Parameter estimation - $Em$, $R_0$, $R_x$, $\tau_x$ | $26.57\,mV$ | $2.23\,mV$ | $1.69\,mV$ | $1.36\,mV$ |
| RMSE between $6\,\%$ to $96\,\%$ *SOC* | $7.42\,mV$ | $2.23\,mV$ | $1.75\,mV$ | $1.39\,mV$ |

**Table 4.9:** Minimum and maximum error between measurement and simulation - Pulse charge test between $6\,\%$ to $96\,\%$ *SOC*

| Temperature | Minimum error | Maximum error |
|---|---|---|
| $10\,°C$ | $-262.41\,mV$ | $140.78\,mV$ |
| $23.8\,°C$ | $-19.00\,mV$ | $16.71\,mV$ |
| $30\,°C$ | $-16.65\,mV$ | $11.11\,mV$ |
| $40\,°C$ | $-10.45\,mV$ | $8.20\,mV$ |

#### 4.2.4.1 Parameter look-up table

The parameter $Em$ is calculated at the end of the relaxation period during pulse discharge and charge tests. Its $1-D$ lookup table with respect to *SOC* breakpoints

for all the four temperatures are shown in figures 4.21 and 4.22. The variation of *Em* voltage points with respect to temperature is minimal.
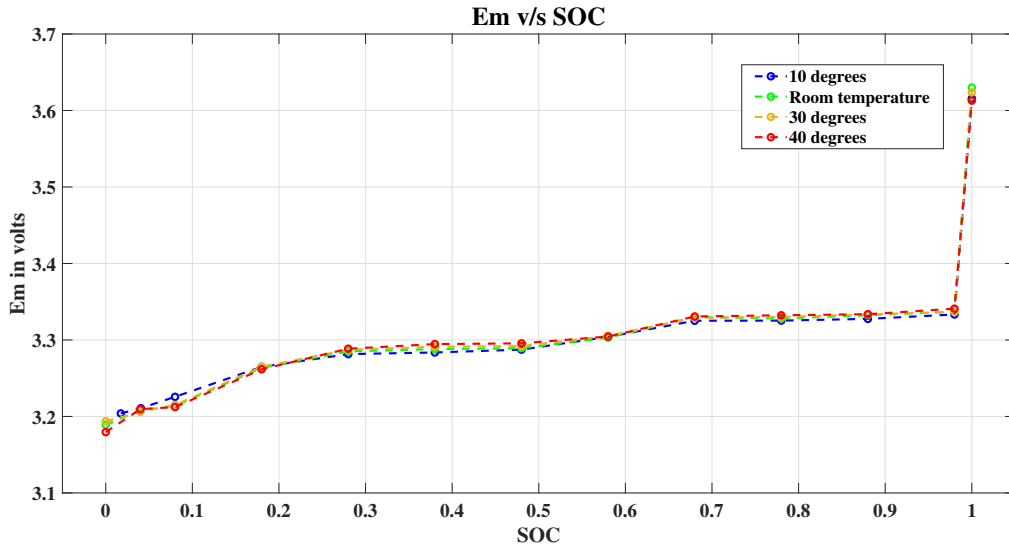


**Figure 4.21:** *Em* v/s *SOC* look up table for pulse discharge tests.
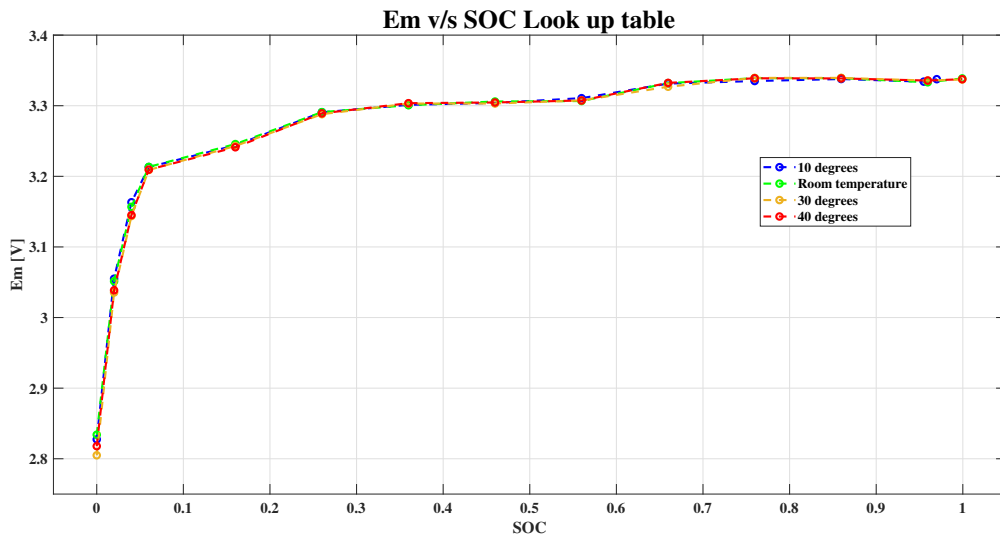


**Figure 4.22:** *Em* v/s *SOC* look up table for pulse charge tests

Electrolytic conductivity is higher as the temperature increases. Hence, lesser resistance at a higher temperature and vice versa at a lower temperature. This behaviour is witnesses in the 2-D lookup table of $R_0$ with respect to *SOC* breakpoints. It is observed for both for pulse discharge and charge test as shown in figures 4.23 and 4.24. Resistance at 10 °C is higher and at 40 °C it is the lower.
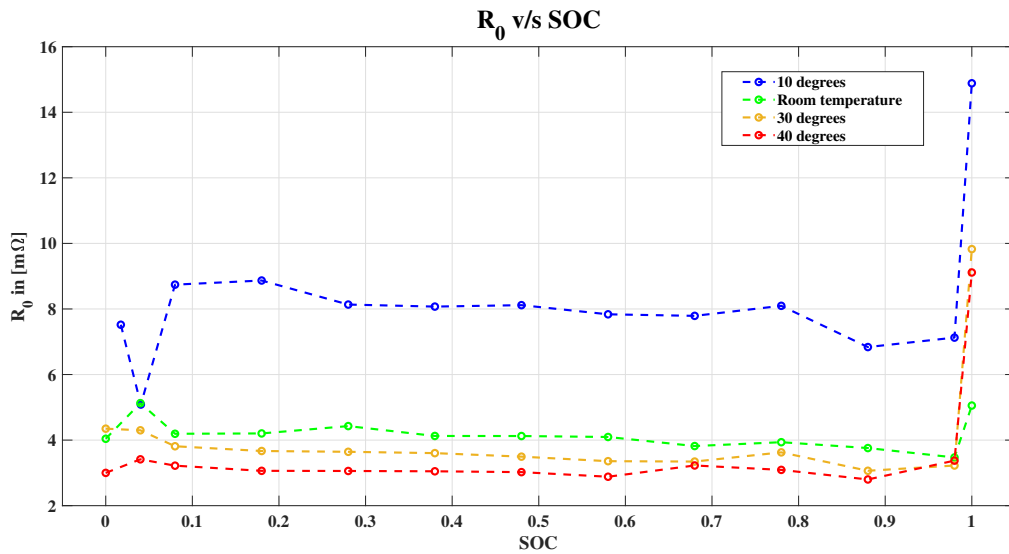
**Figure 4.23:** $R_0$ v/s $SOC$ look up table for pulse discharge tests.
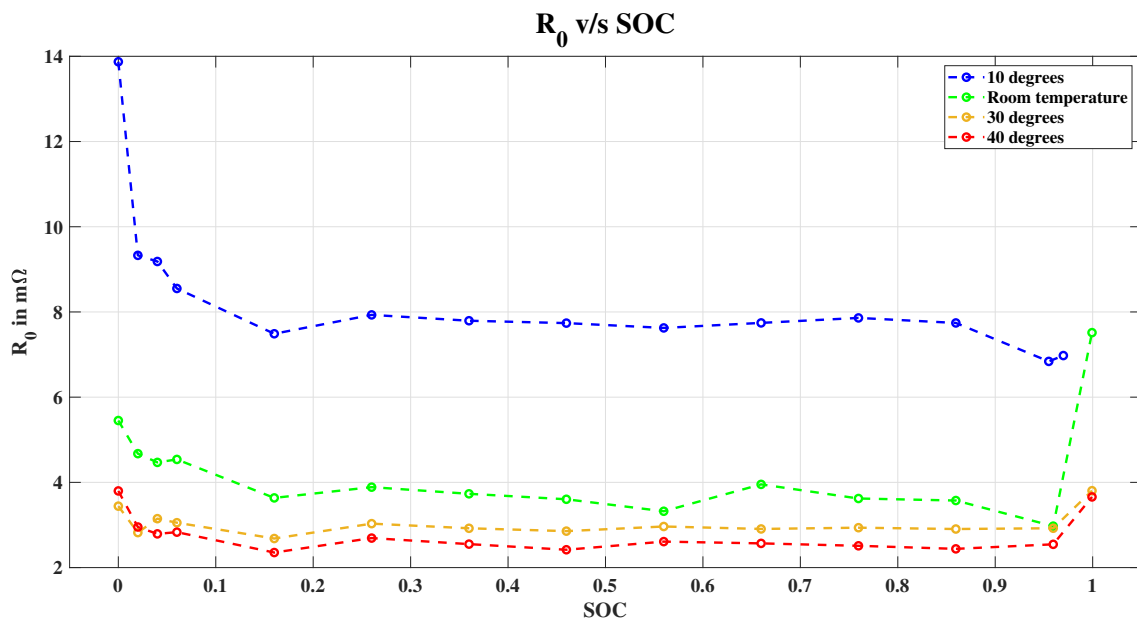


**Figure 4.24:** $R_0$ v/s $SOC$ look up table for pulse charge tests

The time constants of RC links are within their specified limits. $\tau_1$ is within $0\,\text{s}$ to $50\,\text{s}$ for both pulse charge and discharge test as shown in figures 4.25 and 4.26. $\tau_2$ is within $50\,\text{s}$ to $200\,\text{s}$ as seen in figures 4.27 and 4.28. $\tau_3$ is within $200\,\text{s}$ to $3600\,\text{s}$ as shown in figures 4.29 and 4.30. Resistance $R_1$, $R_2$ and $R_3$ at a lower temperature is higher and vice versa at a higher temperature. $C_1$, $C_2$ and $C_3$ values are calculated using (3.6).

**Figure 4.25:** $R_1$, $C_1$, $\tau_1$ v/s $SOC$ look up table for pulse discharge tests.



**Figure 4.26:** $R_1$, $C_1$, $\tau_1$ look up table for pulse charge tests

**Figure 4.27:** $R_2$, $C_2$, $\tau_2$ look up table for pulse discharge tests.



**Figure 4.28:** $R_2$, $C_2$, $\tau_2$ look up table for pulse charge tests

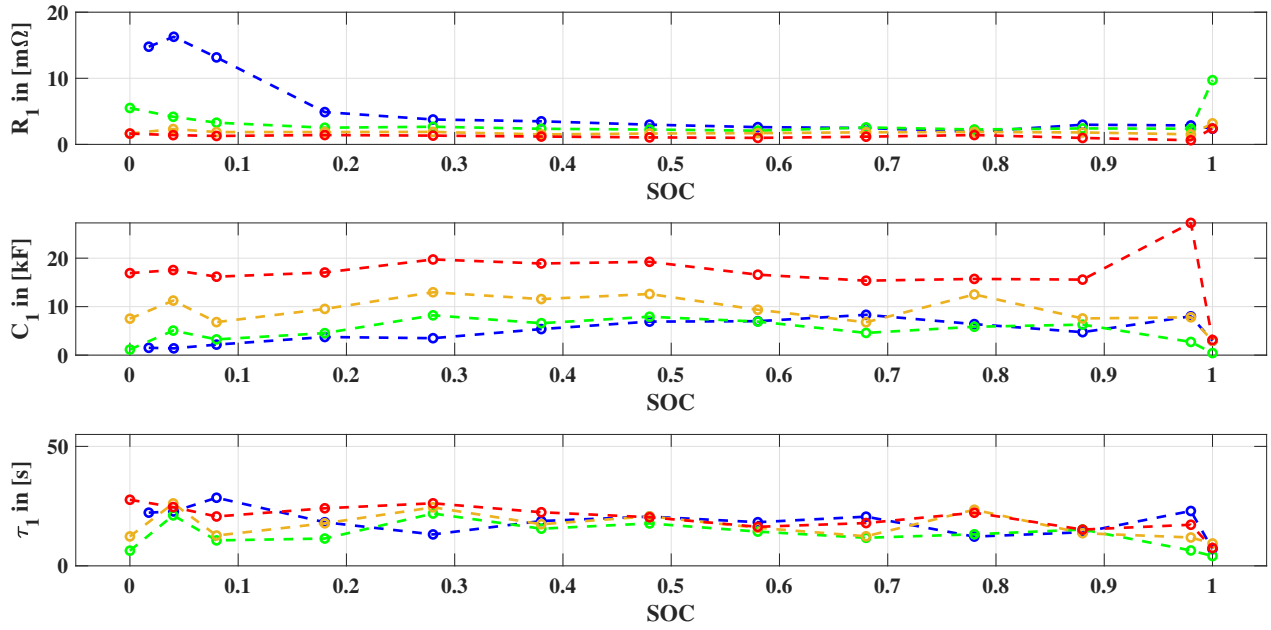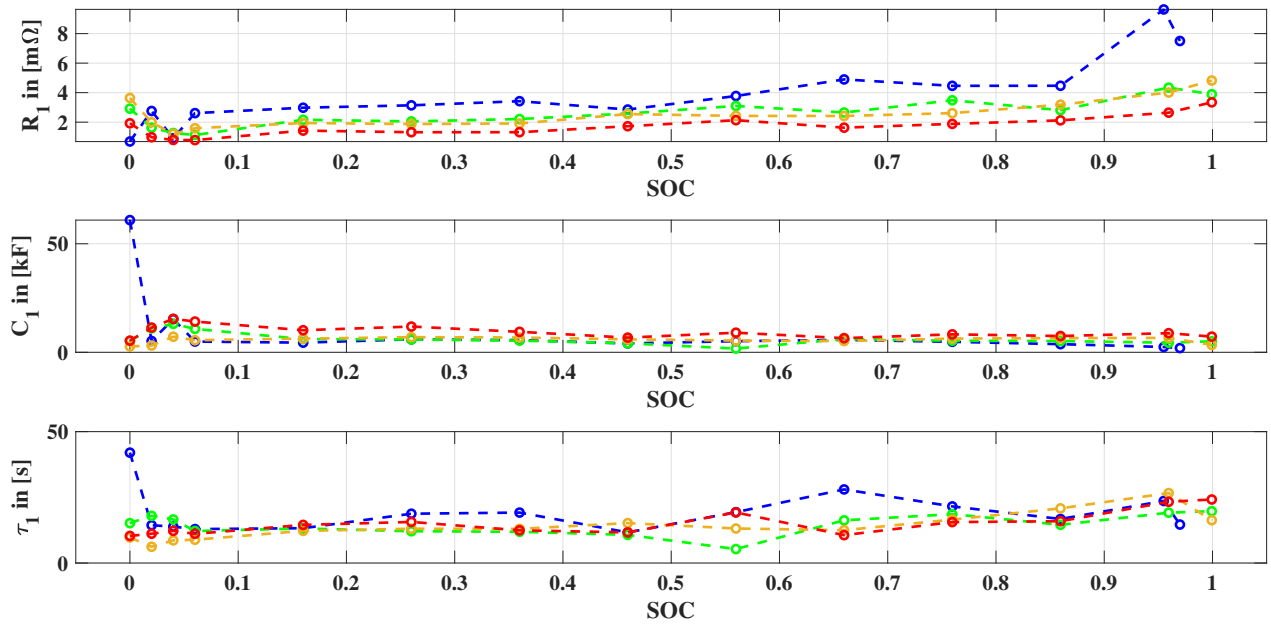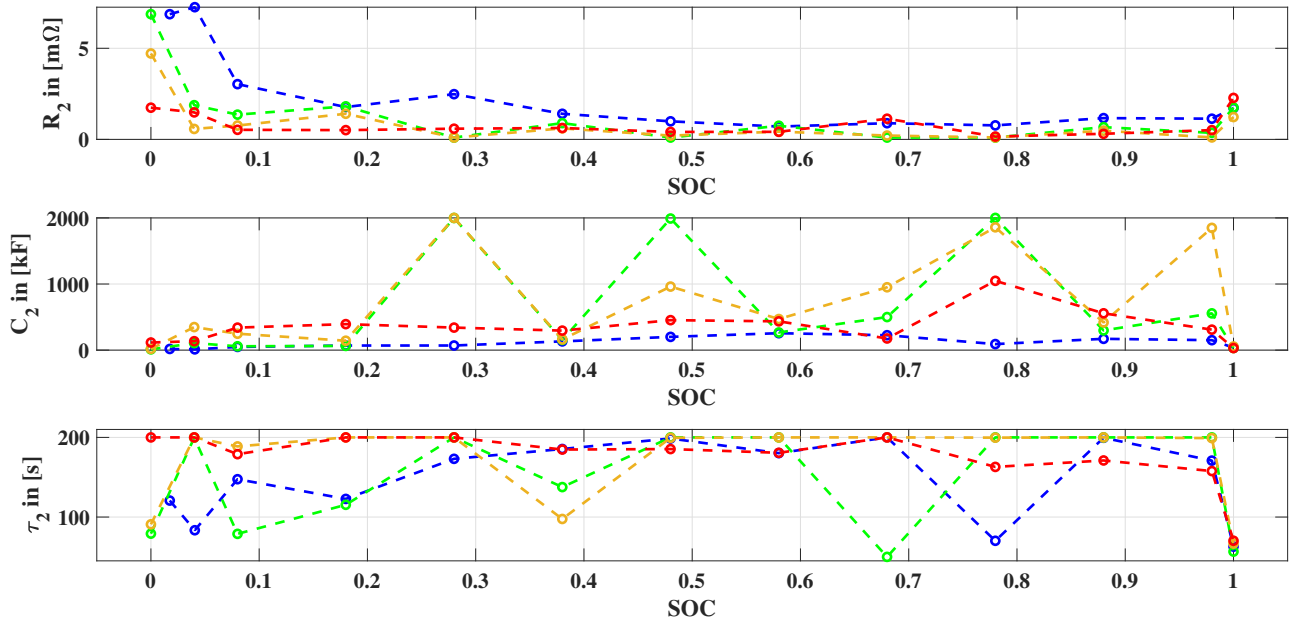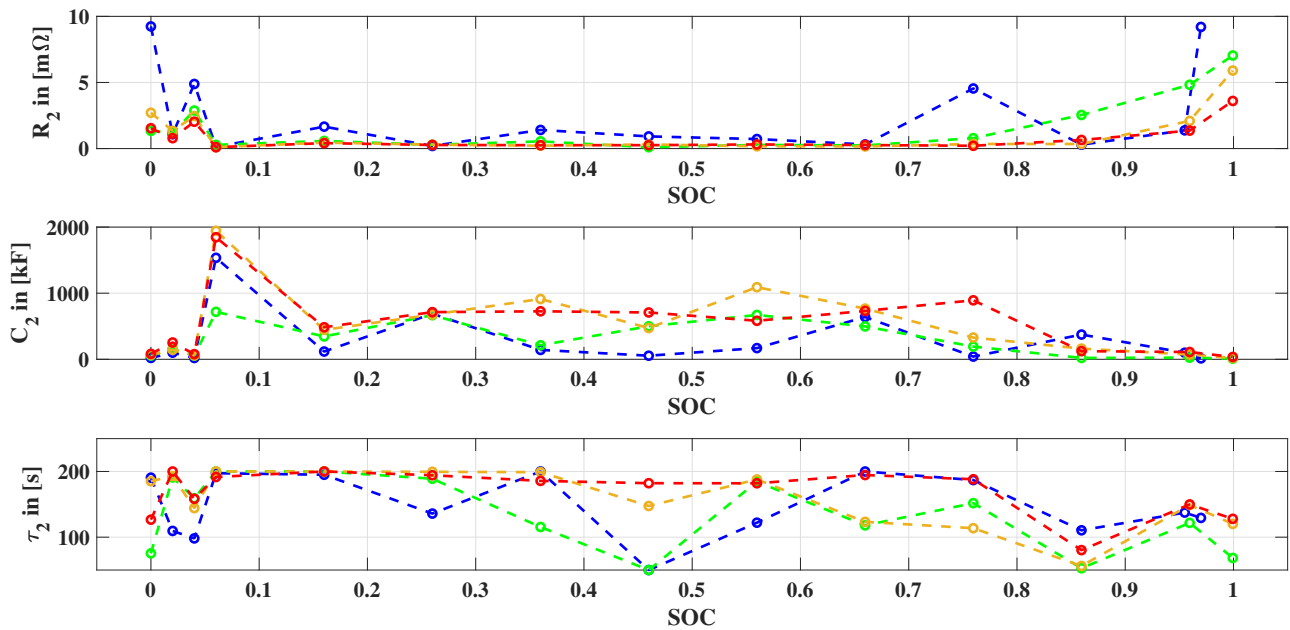**Figure 4.29:** $R_3$, $C_3$, $\tau_3$ look up table for pulse discharge tests
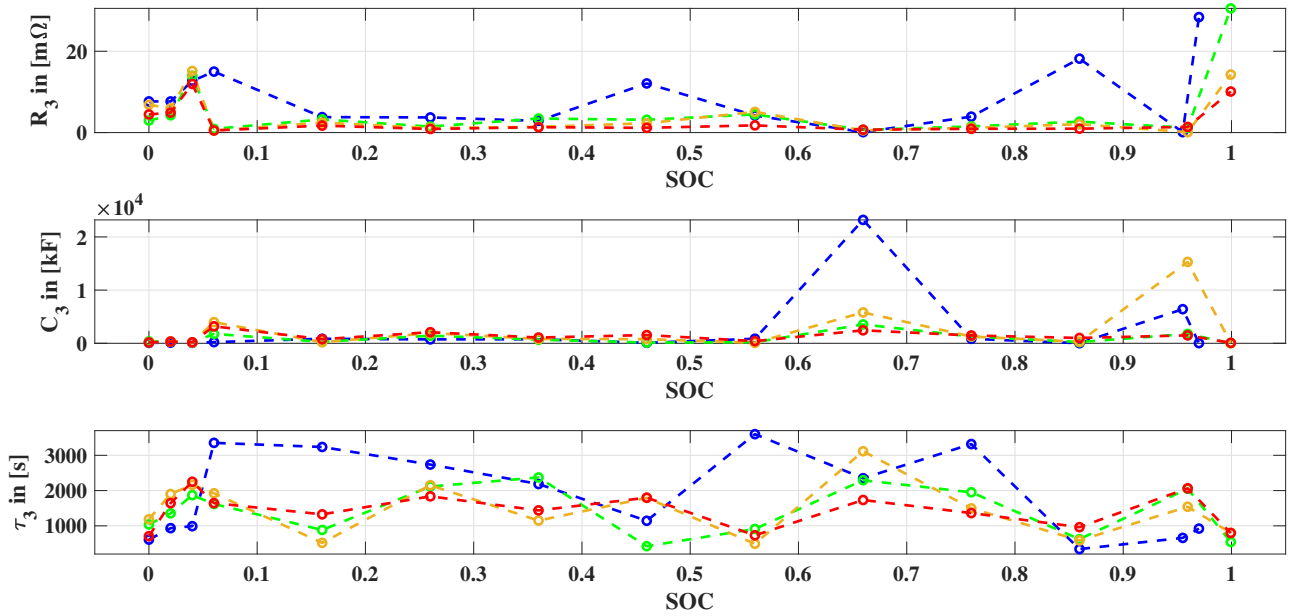


**Figure 4.30:** $R_3$, $C_3$, $\tau_3$ look up table for pulse charge tests

4. Results

## 4.3 Thermal model

To find the thermal properties required for the thermal model, thermal characterisation, and potentiometric tests to determine entropic coefficients were done. In this section, a detailed discussion on these tests and results will be presented.

### 4.3.1 Thermal characterisation - to determine specific heat capacity and internal thermal resistance

The experimental setup required to determine the specific heat capacity and internal thermal resistance of the cell is made as shown in figure 4.31(a). The setup is made according to figure 3.10 and temperature sensors are placed as shown in figure 3.12. The breather material is a soft porous material (similar to any thick fabric) that is laid on the floor of the box and stuck to the walls of a plastic box. Styrofoam sheets are used to cover all the surfaces of the box. The entire experimental setup is placed in this box and a Styrofoam lid is placed on top as shown in figure 4.31(b).

There are two sensors fixed on the inner surface of the box for recording the box temperature, and one sensor is outside the box to record the ambient temperature of the lab during the test (not present in the figure 4.31(a)). For calculations, an ambient sensor outside the box is considered. The box temperature sensors are present only to monitor the box temperature during the test and not used in any calculations.
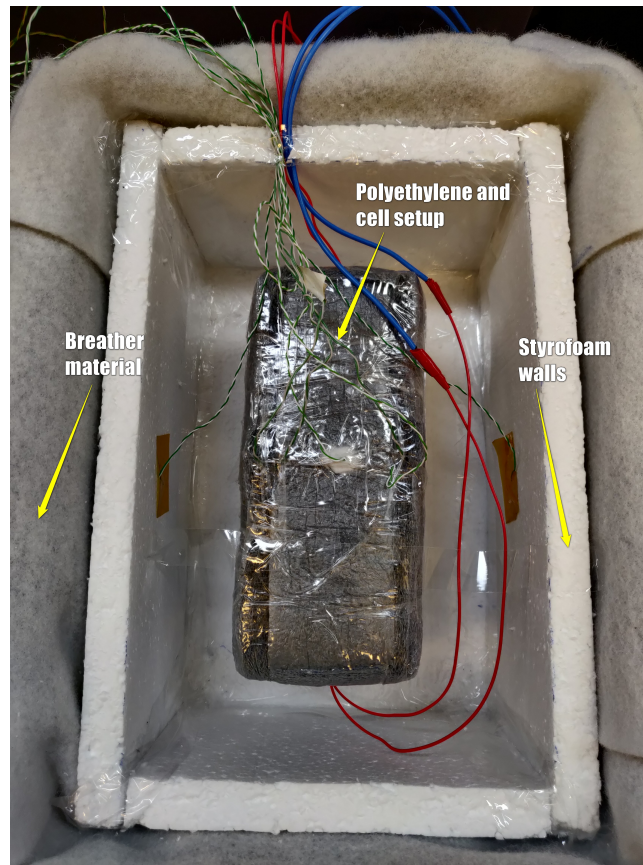
(a) Experimental setup of the cell and polyethylene placed in the styrofoam box.
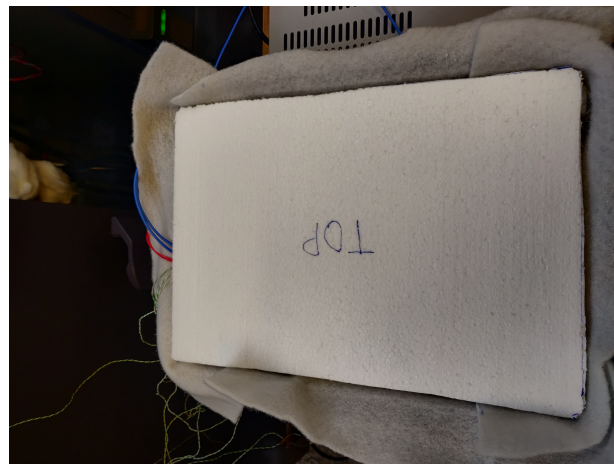


(b) Test setup with the lid

**Figure 4.31:** Test setup

As discussed in section 3.4.1.2, the power $P_W = 2$ W is utilised by the flexible heater to heat-up the setup. Temperatures are recorded during the test. The temperature in the centre is the highest. Successively followed by the surface and insulation temperatures. The ambient temperature is constant without huge fluctuations during the test, as shown in figure 4.32.
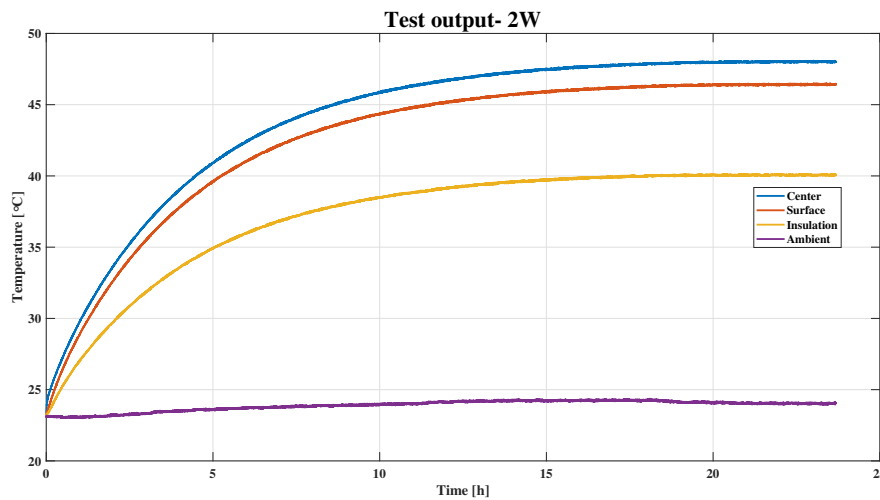
**Figure 4.32:** Test output

The initial and final section is identified from test output as shown in figure 4.33. After the temperatures reached a steady-state, the test is continued for at least 2 h before it is stopped. The final one hour of the test data is the final section. The initial section is identified as the data from 0-95 % of the way to the final value of insulation temperature sensor.

Insulation temperature is smoothed before calculating the temperature corresponding to 95 % value. After smoothing the curve, it is calculated using the data from the final section as,

$$T_{95} = mean(T_{ambient}) + 0.95(mean(T_{insulation}) - mean(T_{ambient})). \tag{4.3}$$
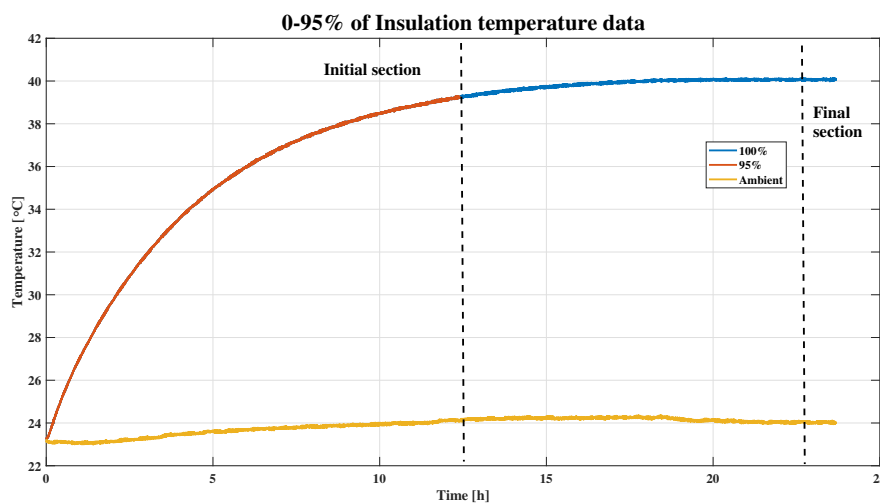


**Figure 4.33:** Identification of initial section and final section from the insulation temperature data.

All the thermal resistances $R_{cell}, R_{insulation}$ and $R_{air}$ are calculated using the data from the final section using (3.19 - 3.22). Curve fitting is done using the final general equation for $T_{insulation}(t)$ (3.18) as shown in the figure 4.34. Following the procedure mentioned in the subsection 3.4.1.4, value of $\zeta$ and $\tau$ is extracted. Heat capacity $C_{cell}$ is calculated.

The value of heat capacity of the cell is found to be $632.32 \, \text{JK}^{-1}$. Specific heat capacity of the cell is calculated by dividing the heat capacity with the cell's weight. Weight of the cell is measured to be $0.606 \, \text{kg}$. Specific heat capacity is found to be $1046.7 \, \text{Jkg}^{-1}\text{K}^{-1}$. Internal thermal resistance of the cell, $R_{cell}$ is calculated to be $0.8 \, \text{KW}^{-1}$.



**Figure 4.34:** Curve fitting for $T_{insulation}$ data at its identified initial section.

This test was done for three different powers, $P_W = 2 \, \text{W}$, $1.6 \, \text{W}$ and $1.2 \, \text{W}$. For each power two trials was done with the same setup. Third trial was done without the lid. Mean value of $C_{p_{cell}}$ and $R_{cell}$ is calculated for each power. Variation of $C_{p_{cell}}$ and $R_{cell}$ with respect to power is shown in figures 4.35(a) and 4.35(b).

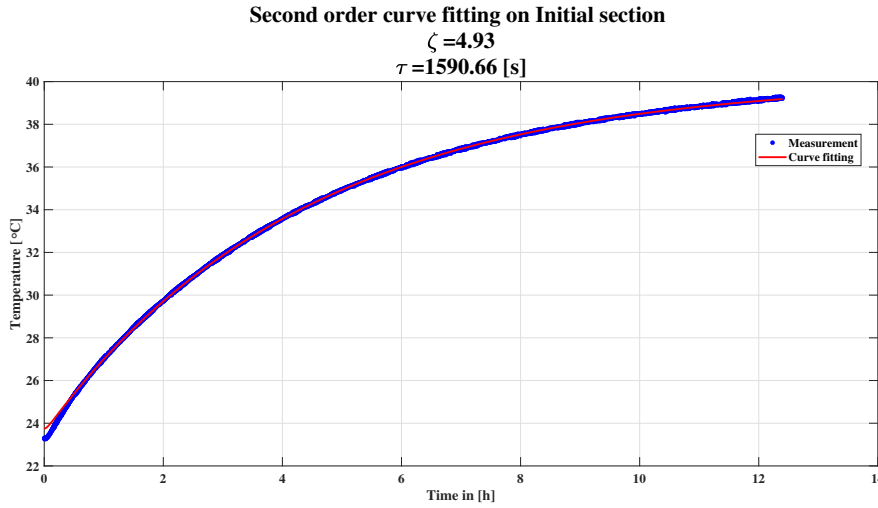There is a good repeat-ability between trials, having maximum deviation of $-29.53$ to $17.97 \, \text{JK}^{-1}\text{kg}^{-1}$ for $1.2 \, \text{W}$ with respect to the mean value of $1059 \, \text{JK}^{-1}\text{kg}^{-1}$ and maximum error range is within $\pm 3 \, \%$. Similarly, $R_{cell}$ also has good repeatability having maximum deviation of $-26$ to $13 \, \text{mKW}^{-1}$ for $1.6 \, \text{W}$ with respect to the mean value of $0.81 \, \text{KW}^{-1}$ and maximum error range is within $\pm 3.5 \, \%$. Since, the test is having good repeatability between different trials, cases, and concerning power. The test is not affected by the power, $P_W$ used for the experiment. Hence, a single test at any power is sufficient to determine the specific heat capacity and thermal resistance of the cell.

**Table 4.10:** Tabulation of various parameters calculated for the tests done at 2 W and $C_{insulation} = 33.39\,\mathrm{J\,K^{-1}}$.

| Parameters | Trial 1 | Trial 2 | Without lid |
|---|---|---|---|
| m | 0.0001 | 0.0001 | 0.0001 |
| n | 3.9331 | 3.9027 | 3.5155 |
| $R_{cell}$ | 0.8 | 0.78 | 0.80 |
| $R_{insulation}$ | 6.35 | 6.42 | 6.54 |
| $R_{air}$ | 10.36 | 10.42 | 3.73 |
| $\tau$ | 1590.5 | 1592.4 | 1252.2 |
| $\zeta$ | 4.93 | 4.90 | 4.51 |
| $R_{in_{error}}\%$ | 0.01 | 0.003 | 0.01 |
| $C_{p_{cell}}[\mathrm{JK^{-1}kg^{-1}}]$ | 1046.7 | 1033.1 | 1027.2 |

**Table 4.11:** Tabulation of various parameters calculated for the tests done at 1.6 W and $C_{insulation} = 33.39\,\mathrm{J\,K^{-1}}$.

| Parameters | Trial 1 | Trial 2 | Without lid |
|---|---|---|---|
| m | 0.0001 | 0.001 | 0.001 |
| n | 3.8494 | 3.965 | 3.584 |
| $R_{cell}$ | 0.78 | 0.82 | 0.82 |
| $R_{insulation}$ | 6.56 | 6.43 | 6.59 |
| $R_{air}$ | 9.57 | 10.38 | 3.11 |
| $\tau$ | 1576.8 | 1622.9 | 1250.8 |
| $\zeta$ | 4.85 | 4.97 | 4.56 |
| $R_{in_{error}}\%$ | 0.01 | 0.004 | 0.004 |
| $C_{p_{cell}}[\mathrm{JK^{-1}kg^{-1}}]$ | 1036.9 | 1065.9 | 1073.9 |

**Table 4.12:** Tabulation of various parameters calculated for the tests done at 1.2 W and $C_{insulation} = 33.39\,\mathrm{J\,K^{-1}}$.

| Parameters | Trial 1 | Trial 2 | Without lid |
|---|---|---|---|
| m | 0.001 | 0.0001 | 0.0001 |
| n | 3.98 | 3.89 | 3.65 |
| $R_{cell}$ | 0.81 | 0.84 | 0.84 |
| $R_{insulation}$ | 6.72 | 6.56 | 6.56 |
| $R_{air}$ | 10.59 | 10.68 | 4.87 |
| $\tau$ | 1686.6 | 1631.1 | 1362.9 |
| $\zeta$ | 4.98 | 4.89 | 4.65 |
| $R_{in_{error}}\%$ | 0.01 | 0.01 | 0.01 |
| $C_{p_{cell}}[\mathrm{JK^{-1}kg^{-1}}]$ | 1077.3 | 1030.8 | 1069.9 |

(a) $C_{p_{cell}}$



(b) $R_{cell}$
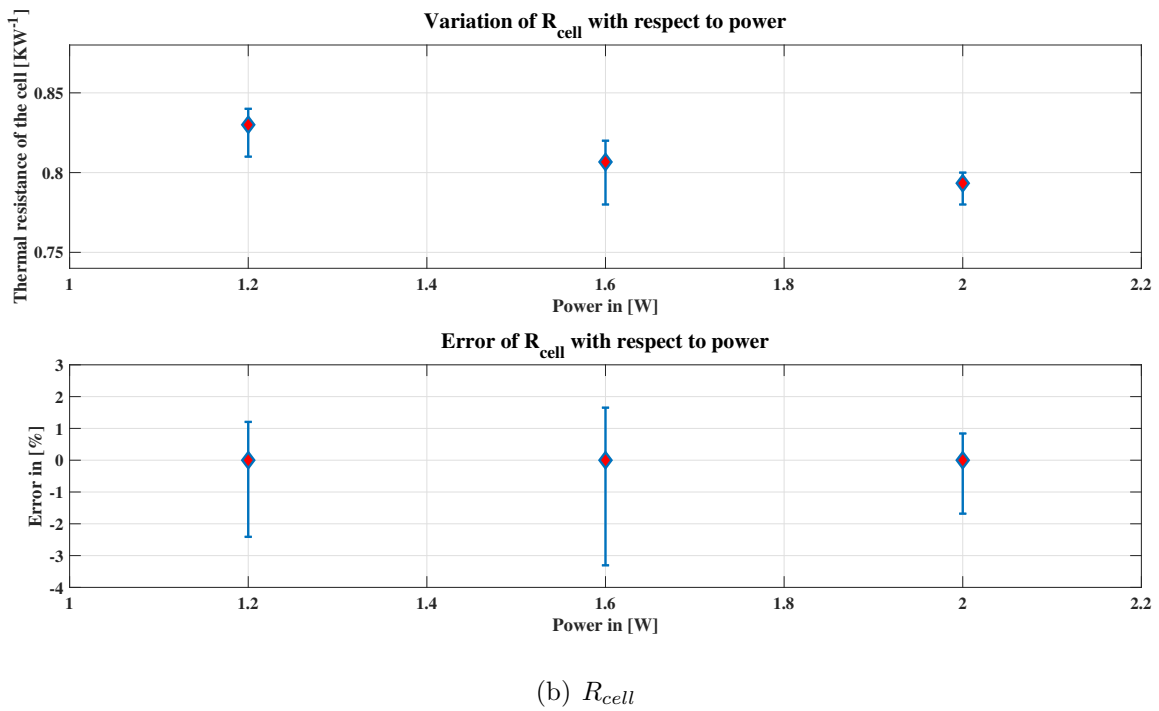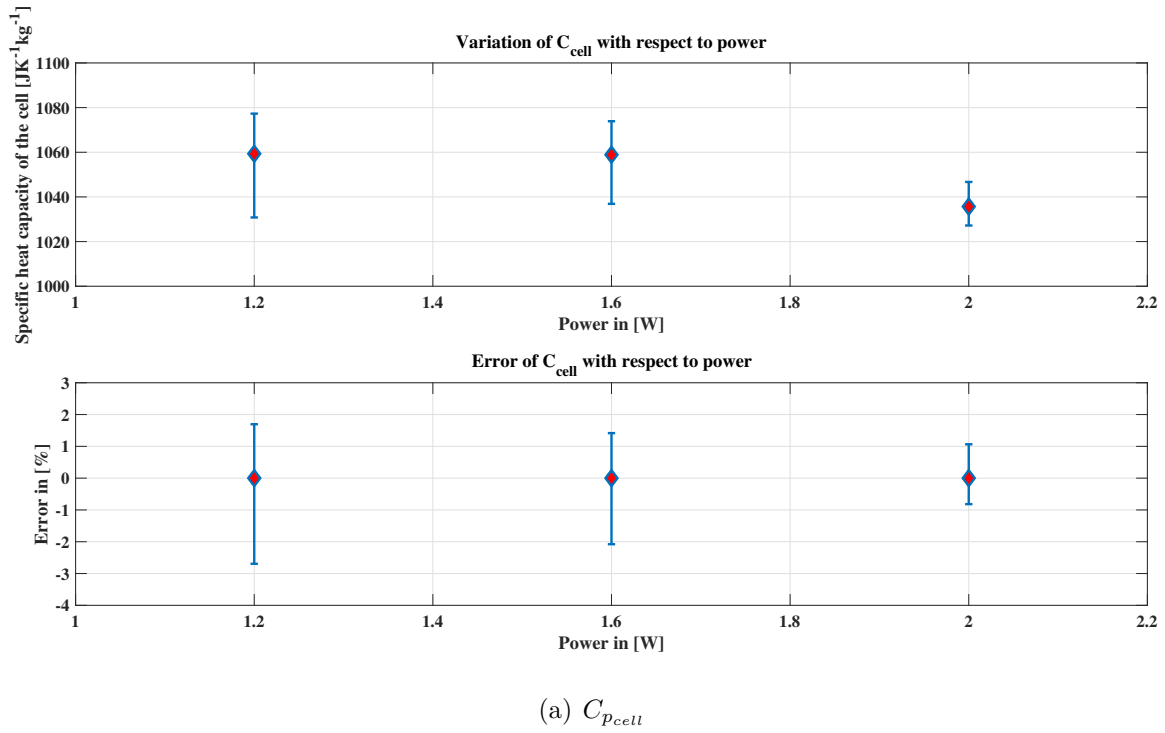
**Figure 4.35:** Graphical representation of variation of parameters due to different trials and with respect to different power

### 4.3.2 Potentiometric test - Determining entropic coefficient

As discussed in section 3.4.2.1, a potentiometric test is done on the cell. The setup is as shown in figure 4.9. The cell is kept in a temperature chamber with a temperature sensor, sensing the surface temperature of the cell. The cell is kept at $25\,°C$ for at least 5 hours. The temperature is then changed to $35\,°C$ and $15\,°C$. The cell is kept at each temperature for at least 2 hours for the cell to reach thermal equilibrium. The discharge current of $0.1C = 2\,A$ is used to discharge the cell by $10\%\ SOC$.

Due to the time taken by the temperature chamber to change to the selected temperatures, perfect synchronisation of the discharge pulse and temperature change is not achieved. At $40\%\ SOC$ as shown in figure 4.36, temperature settings of the chamber were re-adjusted to make sure that the temperature changes after the cell relaxes for a minimum time of hours after the discharge current pulse. Voltage points at different temperatures after the cell has reached its thermal equilibrium is identified as shown in figure 4.36.
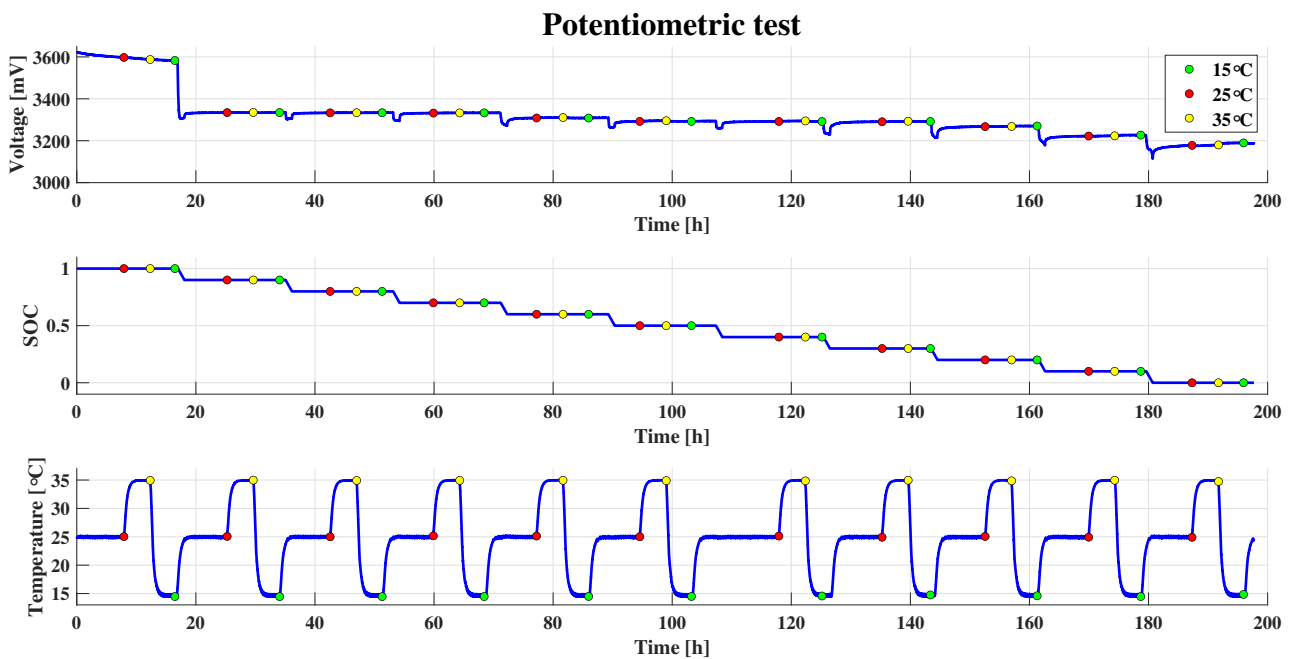


**Figure 4.36:** Potentiometric test output. Voltage points are marked for different temperatures. It is marked after the cell has reached its thermal equilibrium.

The relaxation background is shown in the figure 4.37. It is identified by extrapolation using the first-order polynomial equation. The voltage change points are calculated by subtracting voltage points with their corresponding relaxation background.
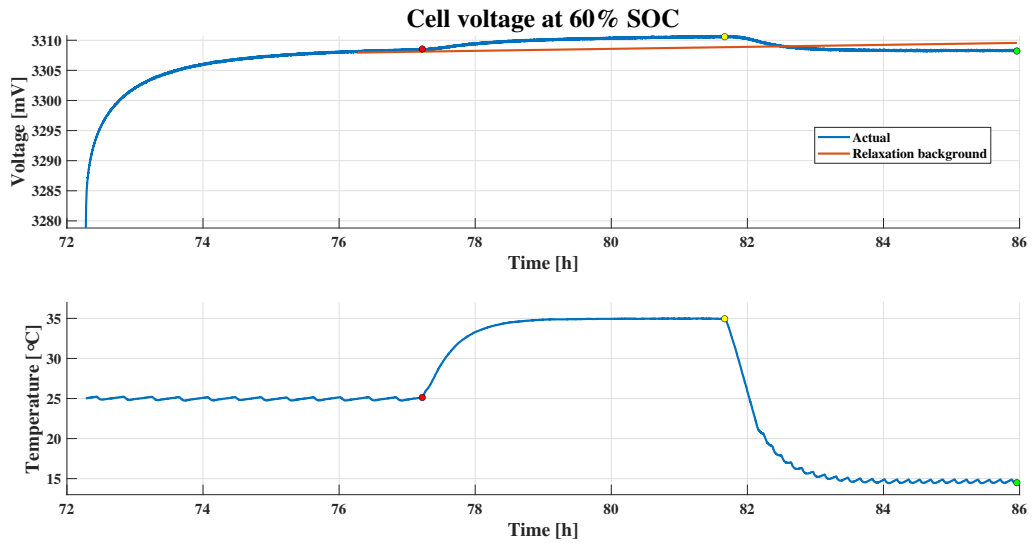
**Figure 4.37:** Extrapolation using first order polynomial fit at 60%$SOC$.

The slope calculated using the voltage change points in the y-axis and its corresponding temperature in the x-axis gives the entropic coefficient $dU/dT$, as shown in figure 4.38. At 60% $SOC$, the entropic coefficient is found to be $0.15\,\mathrm{mV°C^{-1}}$. Entropic coefficients found for different $SOC$ levels are as shown in figure 4.39. The trend of the entropic coefficients concerning $SOC$ is in agreement with the result given in [58]. The entropic coefficients are in the range of $\pm 0.2\,\mathrm{mV°C^{-1}}$. The test is not repeated to check the repeat-ability, since the test takes around 200 hours to complete. The entropic coefficients found will be used when calculating the reversible losses and will be fed to the thermal model.
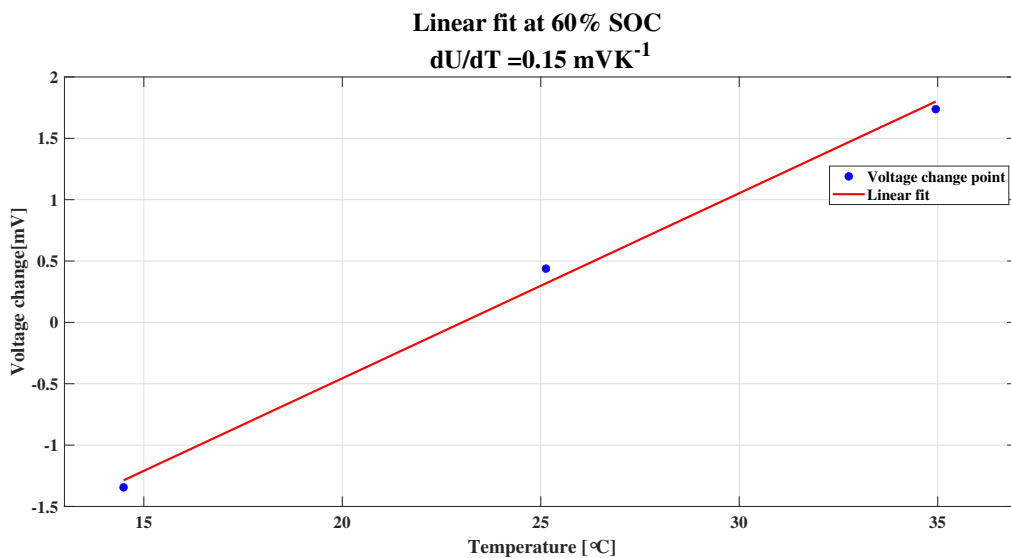


**Figure 4.38:** Linear fitting the voltage change points at different temperatures.
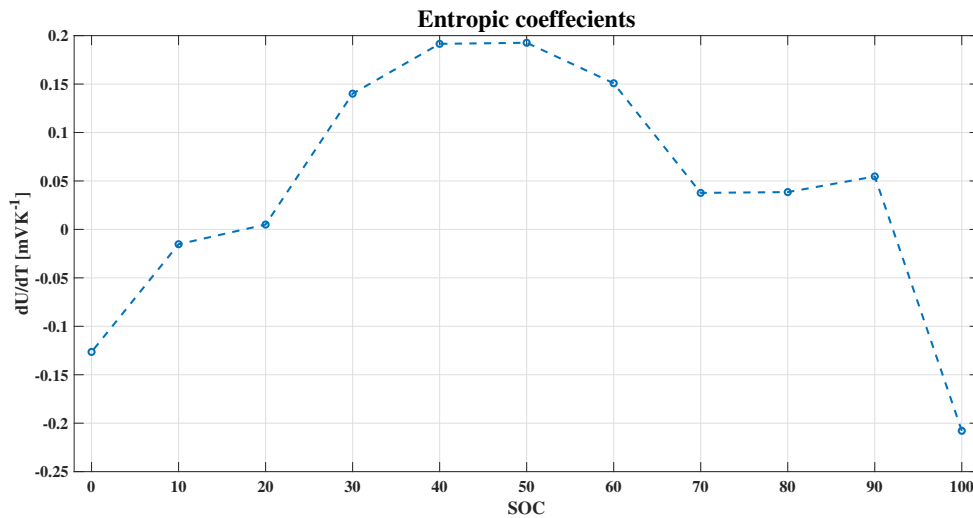
**Figure 4.39:** Entropic coefficients with respect to its *SOC*.

It is interesting to know at which C-rate, reversible and irreversible losses affect the temperature of the cell. In [29], at lower currents, reversible heat loss has a dominating effect when compared with irreversible heat loss and vice versa at higher currents. The same observations are made in figure 4.40. In this illustration as shown in figure 4.40, 50% *SOC* and 20 °C is chosen. Simulink models as shown in figure 3.22 and 3.23 are used. At 50% *SOC*, value of entropic coefficient is $0.2\,\mathrm{mVK^{-1}}$. The analysis is done for both irreversible heat losses corresponding to the discharge and charge parameters. The reversible losses dominate over the irreversible losses for charge and discharge parameters, under 0.24 and 0.55 C-rate respectively. If the cell is operated at lower currents, such as for lighting application, then the accuracy of the entropic coefficient is vital for accurate calculation of losses and estimation of surface temperature.
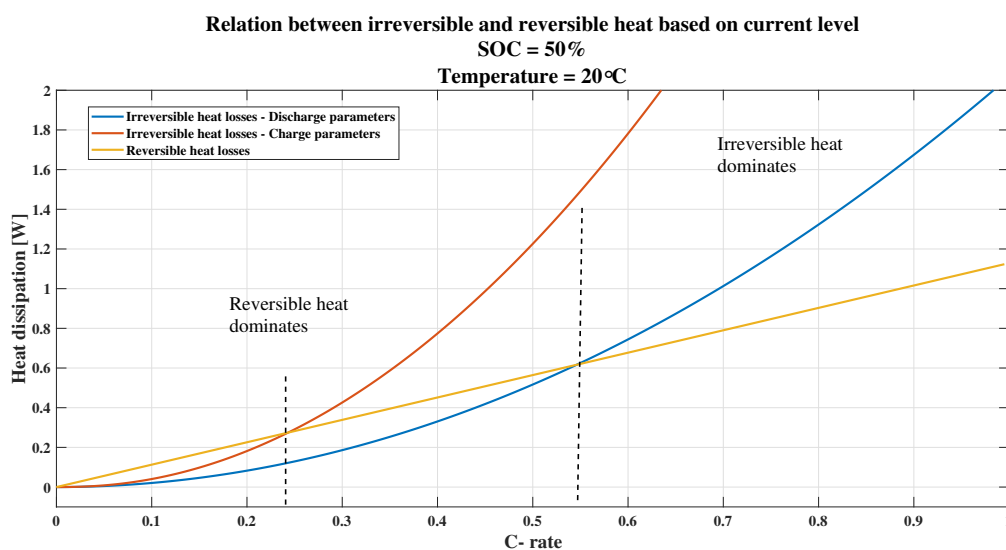


**Figure 4.40:** Relation between reversible and irreversible heat loss based on current at 50% *SOC* and 20 °C.

### 4.3.3  Thermal model verification

It is important to know if the value of specific heat capacity and thermal resistance of the cell is accurate. To verify this, a simple test is conducted. The modified setup of figure 3.12 is shown in figure 4.41. It is a first-order thermal model. The outer insulation on the surface of the cell is removed. There are three temperature sensors to measure the temperature at the centre, surface, and ambient.
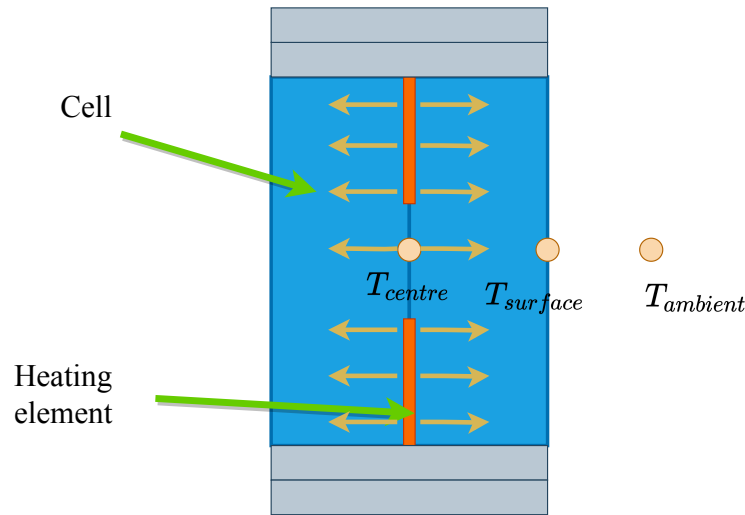


**Figure 4.41:** Modified setup for thermal model verification. It is a single order thermal model.

The Simscape model as shown in figure 3.24 is used for the analysis. The first test is to determine the thermal resistance of air $R_{out}$. The flexible heaters are heated by supplying a known power of $P = P_W/2 = 0.9\,\text{W}$ for around 25 hours until the temperature reaches a steady state.
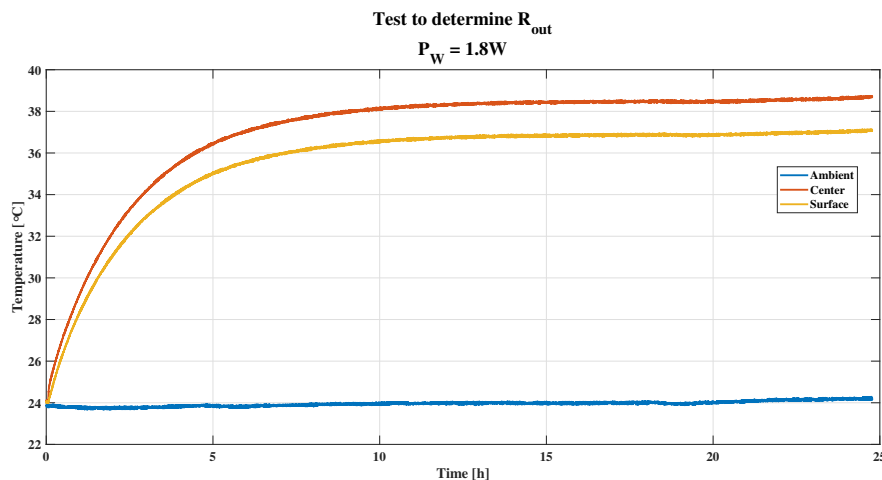


**Figure 4.42:** Test to determine $R_{out}$ for single order thermal model.

By using the last one hour of the test data, as shown in figure 4.42 at steady-state, $R_{out}$ is calculated using the mean of the temperature difference between the surface

and the ambient. It is divided by the rate of heat $P$. It is shown as,

$$R_{out} = \frac{mean(T_{surface}(t = \infty)) - mean(T_{ambient}(t = \infty))}{P} \qquad (4.4)$$

where, $R_{out}$ is found to be $14.28\,\mathrm{KW^{-1}}$.

After finding $R_{out}$ from the first test, the second test is performed. The second test is performed to determine the performance of the model comparing the experiment. In this test, the power to the heater is switched on for 2 h and switched off for 1 h. This is repeated 3 times. The power $P_W$ given to the heater is $1.5\,\mathrm{W}$. Hence, the heat generated at the centre is $0.75\,\mathrm{W}$ ($P = P_W/2$). The test output is shown in figure 4.43(a).

The power profile and ambient temperature are given as the input to the Simscape model and the surface temperature is the output. The model output is closely matching with the measured values of surface temperature from the test, as seen in figure 4.43(b). Three different $C_{cell}$ and $R_{cell}$ is chosen as shown in table 4.13. $C_{cell}$ and $R_{cell}$ are the mean values of the three trials in tables 4.10 to 4.12.

The maximum error for all trials, between model and experiment, is within $0.5\,°C$. RMS error is also lesser than $0.15\,°C$. The error in percentage is within $\pm 1.7\%$. Hence, the values of specific heat capacity and thermal resistance of the cell can be used in the model and the estimated surface temperature is reliable. Considering, when $C_p = 1035.67\,\mathrm{JK^{-1}kg^{-1}}$ and $R_{cell} = 0.79\,\mathrm{KW^{-1}}$ is used and gives the least error among the three cases. These two values of $C_{cell}$ and $R_{cell}$ would be used in the upcoming analysis.

**Table 4.13:** Maximum and RMS error between the model and experiment for three different cases. The mean values of $C_{cell}$ and $R_{cell}$ of three trials for $2\,\mathrm{W}$, $1.6\,\mathrm{W}$ and $1.2\,\mathrm{W}$ mentioned in tables 4.10 to 4.12 are used.

| $C_{p_{cell}}[\mathrm{JK^{-1}kg^{-1}}]$ | $R_{cell}[\,\mathrm{KW^{-1}}]$ | $R_{out}[\mathrm{KW^{-1}}]$ | **Max(\|Error\|)** [°C] | RMSE [°C] |
|---|---|---|---|---|
| 1035.67 | 0.79 | 14.28 | 0.39 | 0.11 |
| 1058.9 | 0.8 | 14.28 | 0.46 | 0.13 |
| 1059.33 | 0.83 | 14.28 | 0.46 | 0.13 |
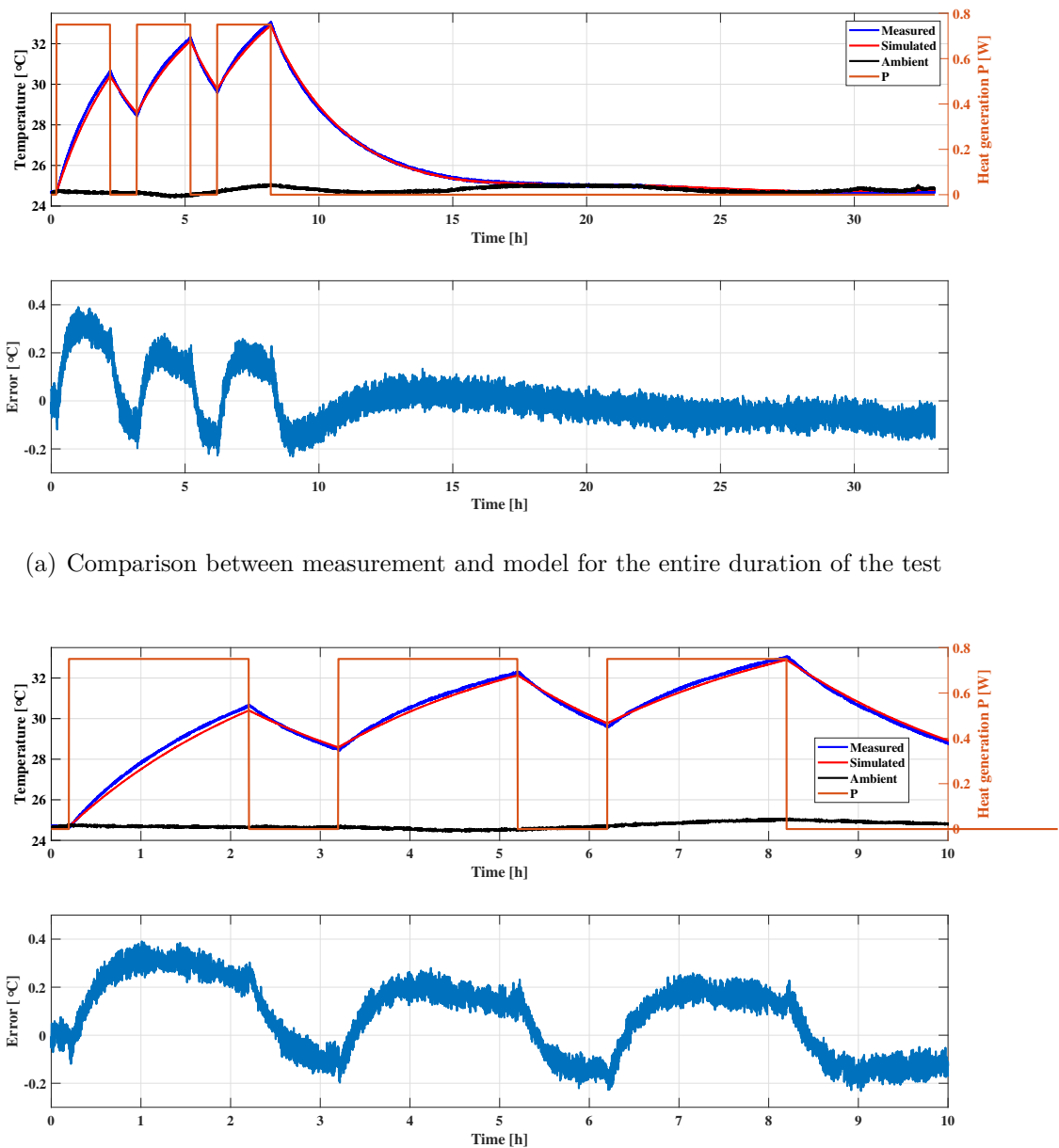
(a) Comparison between measurement and model for the entire duration of the test



(b) Comparison between measurement and model. Magnified image. image.

**Figure 4.43:** Test output and Comparison between measurement and model. $C_{cell} = 1035.67 \, \text{JK}^{-1}\text{kg}^{-1}$ and $R_{cell} = 0.79 \, \text{KW}^{-1}$ is chosen in the model.

## 4.4 Model verification using - Drive cycle data

After the electrical and thermal characterisation is complete, the final cell model is made as per section 3.5. It is interesting to verify this model to know the performance of the model. It is to see how good the model predicts the surface temperature of the cell and the open-circuit voltage. At first, the calibration of the model is done using the NEDC test cycle. Then, by using the WLTC test cycle and the same

calibration values, the model is verified.

### 4.4.1 Test output - Drive cycles



(a) NEDC test cycle



(b) WLTC test cycle
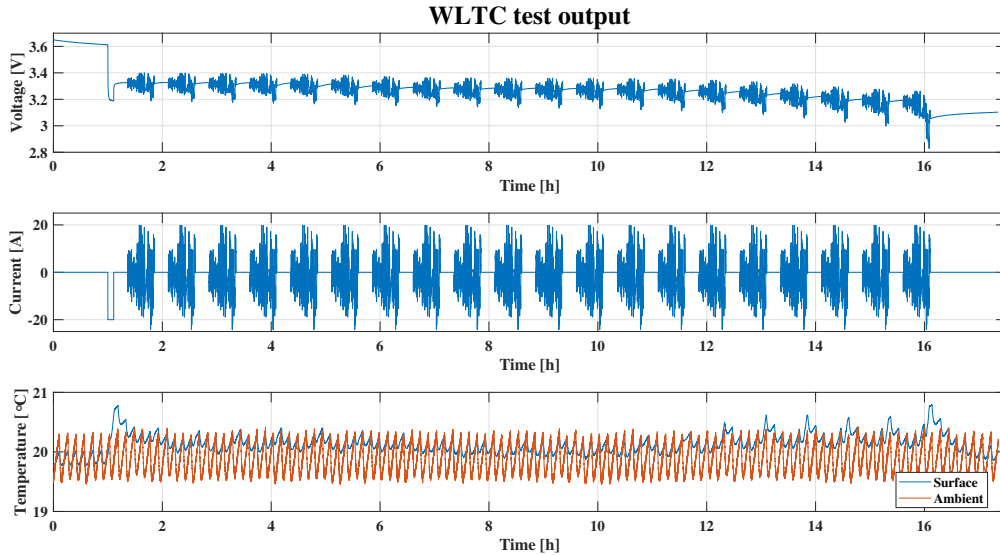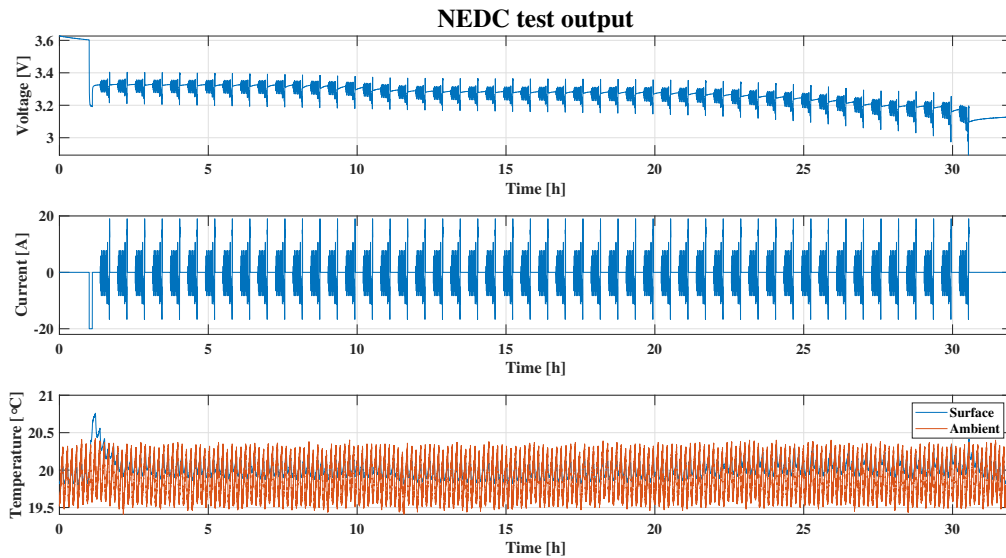
**Figure 4.44:** Test output

The cell is placed in the temperature chamber. The two drive cycles, NEDC and WLTC current profiles have charge and discharge points. The cell is charged and discharged according to these current profiles. Open circuit voltage and surface temperature of the cell is recorded during the test. Also, the ambient temperature

recorded during the test is given as the input to the cell model. Current profiles for these two cycles are found based on the discussion done in section 3.6.

The cell is initially discharged by 10% $SOC$ with 20 A. This is done to avoid the overcharging of the cell due to charging current, present in the current profile. Since in the electrical characterisation, the error is maximum at low and high $SOC$ region. In this analysis the region of interest is from 90-10% $SOC$. Between every drive cycles resting time of 20 minutes is used. This is to replicate the driving pattern, where the driver stops and restarts the vehicle. Test results due to both of the drive cycles are shown in figure 4.44(a) and 4.44(b). The ambient temperature inside the temperature chamber is not constant and it fluctuates within 1 °C. The current profiles are repeated until the cell reaches 0% $SOC$.

## 4.4.2   Model calibration using NEDC test cycle

After making the model, the model requires the value of $R_{out}$ in its thermal model. Conventionally, to find this a separate test is required. Where, the cell is kept at 50% $SOC$. A charging and discharging current pulse ($\geq 1C$) is given such that the $SOC$ changes by equal amounts, usually lesser than $\pm 5\%$ $SOC$. These pulses are continued until the cell surface temperature reaches a steady state. Heat dissipation and $R_{out}$ is calculated as given in [28].

In this thesis to find $R_{out}$, a different approach is implemented using the NEDC test cycle. The heat dissipation $P_{sim}$ is calculated using the heat loss calculation model as shown in figure 3.22. Using the mean values of $P_{sim}$, surface and ambient temperature between 90-10% $SOC$, $R_{out}$ is calculated as,

$$R_{out} = \frac{mean(T_{surface} - T_{ambient})}{mean(P_{sim})} \tag{4.5}$$

Due to modelling errors and approximations, the offset in open circuit voltage is observed. This voltage error was removed by adding a voltage correction factor $V_{correction}$ to the cell model voltage. It is calculated as the mean of the difference between the measured voltage from NEDC test cycle and cell model voltage between 90-10% $SOC$. It is given as,

$$V_{correction} = mean(V_{measured} - V_{model}) \tag{4.6}$$

The values of external thermal resistance $R_{out}$ and voltage correction factor $V_{correction}$ using (4.5 and 4.6) are presented in table 4.14. These two values will be used when verifying the model.

**Table 4.14:** Calculated calibration values

| Parameter | Value |
|---|---|
| $R_{out}$ | $1.61 \, \mathrm{K \, W^{-1}}$ |
| $V_{correction}$ | $-16.8 \, \mathrm{mV}$ |

### 4.4.3 Model verification results

In this section, we observe how well open-circuit voltage and the surface temperature from the model matches with actual values of the voltage response and temperature of the cell due to the drive cycle current profile. From the previous analysis during electrical characterisation, it was observed that the electrical model had higher errors at both low and at high $SOC$. It was due to the higher change in voltage at those $SOC$ regions. This behaviour is observed in this analysis as well. In figures 4.45(a) and 4.45(b), at low and at high $SOC$ regions, the error is higher. The maximum errors seen in this region is higher than the errors seen from 90-10 % $SOC$, as shown in table 4.15. Since the electrical parameters are used in the calculation of irreversible heat losses, the errors in the surface temperature estimation is also higher at low and high $SOC$ regions, as shown in table 4.16. It can be observed visually in figures 4.46(a) and 4.46(b).

As expected, by using the values of $R_{out}$ and $V_{correction}$ as mentioned in table 4.14, the RMSE between the actual and model open circuit voltage has reduced from 19.5 mV to 9.83 mV for NEDC drive cycle. Similarly, for WLTC the RMSE has reduced from 22.43 mV to 13.36 mV. The model is closely matching with the actual values of the open circuit voltage. It has managed to accurately predict the open circuit voltage of the cell, this can be observed for both NEDC and WLTC drive cycle in figures 4.47(a) and 4.47(b).

**Table 4.15:** Summary of electrical model performance for both NEDC and WLTC drive cycle. Error between measurement and model voltage

|  | 100-0% $SOC$ before calibration | 100-0% $SOC$ after calibration | 90-10% $SOC$ before calibration | 90-10% $SOC$ after calibration |
|---|---|---|---|---|
| NEDC-RMSE | 53.82 mV | 55.51 mV | 19.50 mV | 9.83 mV |
| NEDC-Max | 254.58 mV | 271.38 mV | 86.98 mV | 70.18 mV |
| WLTC-RMSE | 58.59 mV | 61.43 mV | 22.43 mV | 13.36 mV |
| WLTC-Max | 230.73 mV | 247.53 mV | 87.08 mV | 70.28 mV |

Similarly, the estimated surface temperature of the cell closely matches the experiment, as seen in figures 4.48(a) and 4.48(b). The RMS errors for the NEDC and WLTC drive cycles is found to be 0.04 °C and 0.07 °C respectively. The maximum errors for both the drive cycles are small and are <1 °C. The surface temperature of the cell can be estimated to be very close to the actual value, and this model is thus reliable.

**Table 4.16:** Summary of thermal model performance for both NEDC and WLTC drive cycle. Error between measurement and model surface temperature

|           | 100-0% $SOC$ | 90-10% $SOC$ |
|-----------|--------------|--------------|
| NEDC-RMSE | 0.06 °C      | 0.04 °C      |
| NEDC-Max  | 0.62 °C      | 0.32 °C      |
| WLTC-RMSE | 0.09 °C      | 0.07 °C      |
| WLTC-Max  | 0.62 °C      | 0.36 °C      |
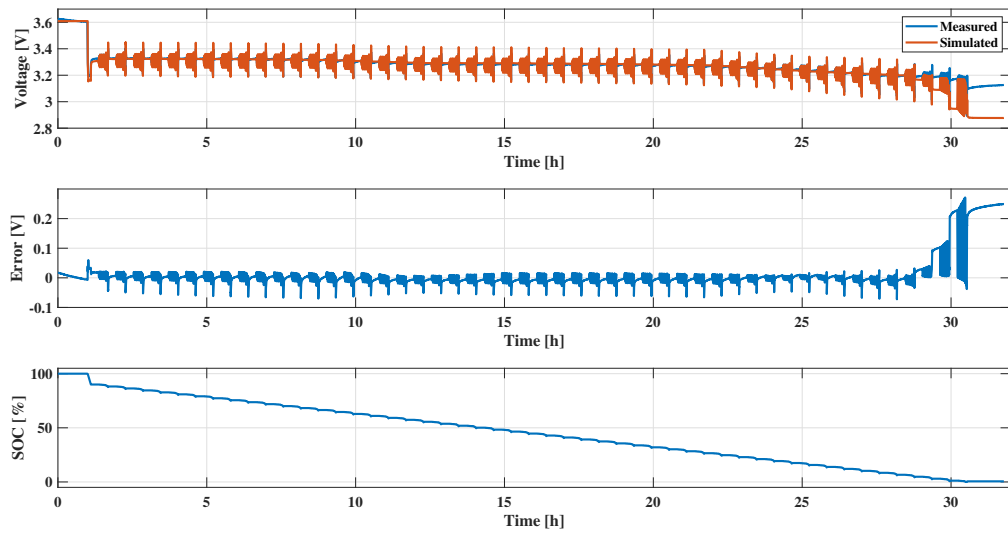
(a) NEDC test cycle
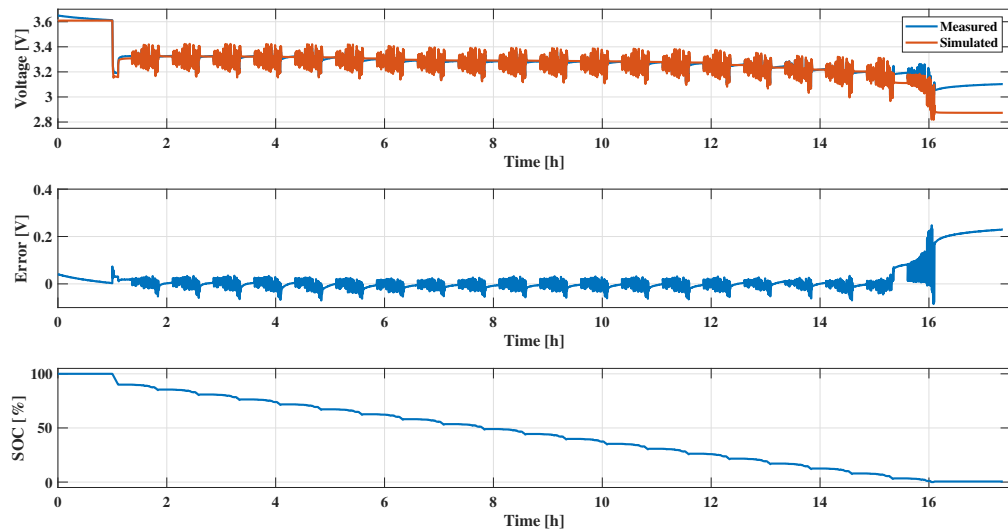


(b) WLTC test cycle

**Figure 4.45:** Electrical model performance for different drive cycles from 100-0% *SOC*.
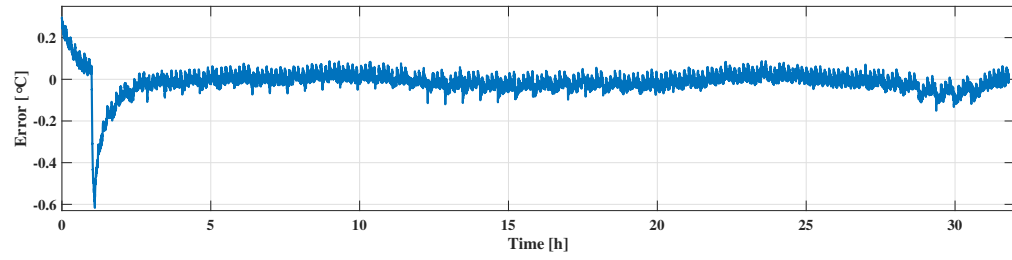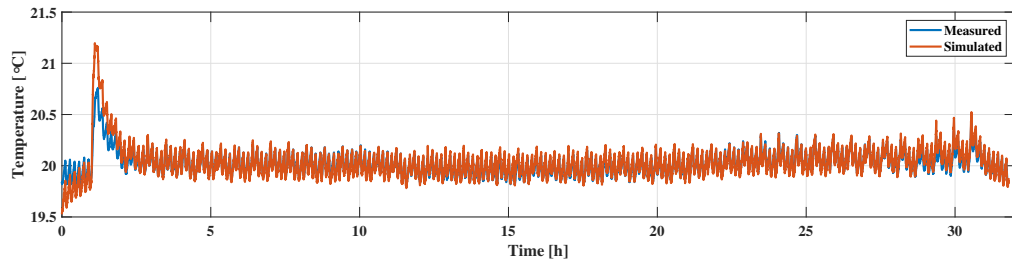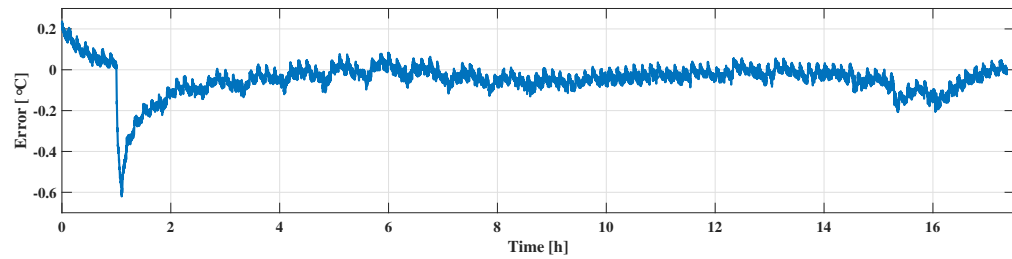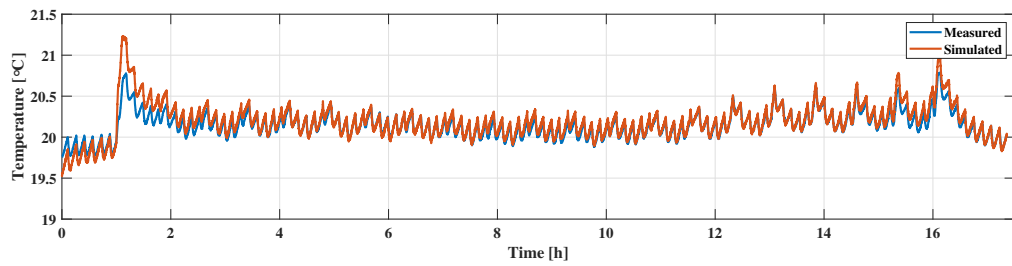
(a) NEDC test cycle



(b) WLTC test cycle

**Figure 4.46:** Thermal model performance for different drive cycles from 100-0% *SOC*.
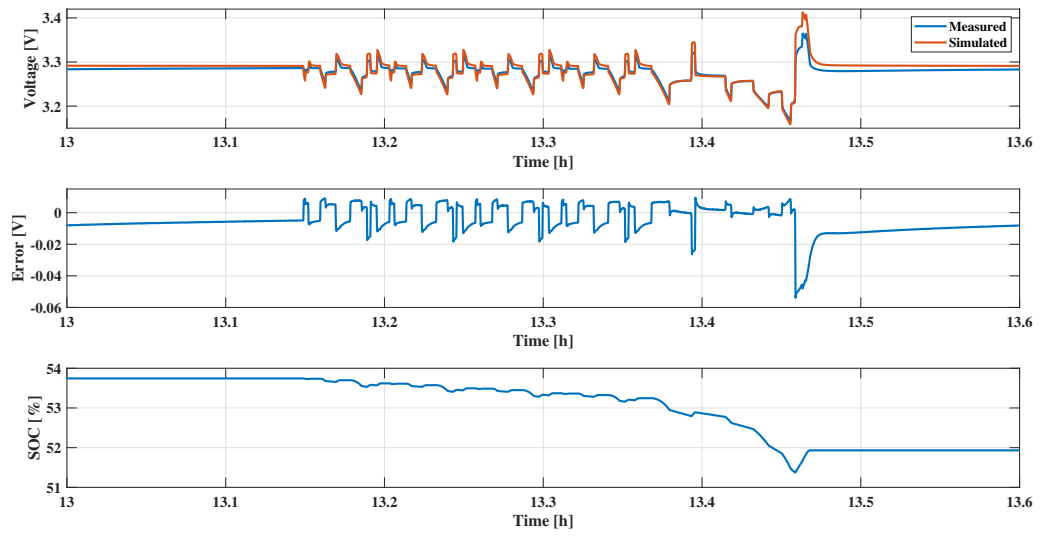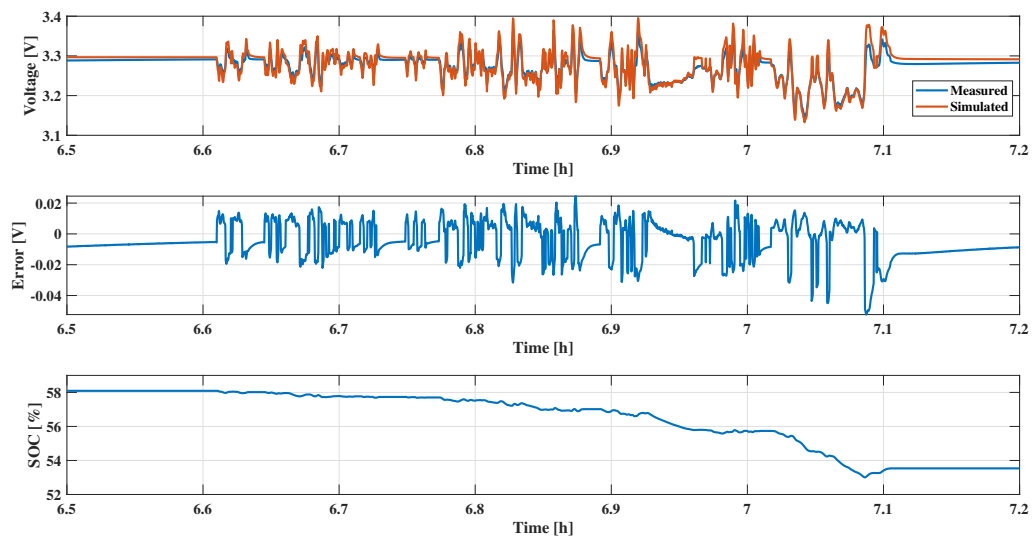
(a) NEDC test cycle



(b) WLTC test cycle

**Figure 4.47:** Electrical model performance. Magnified image
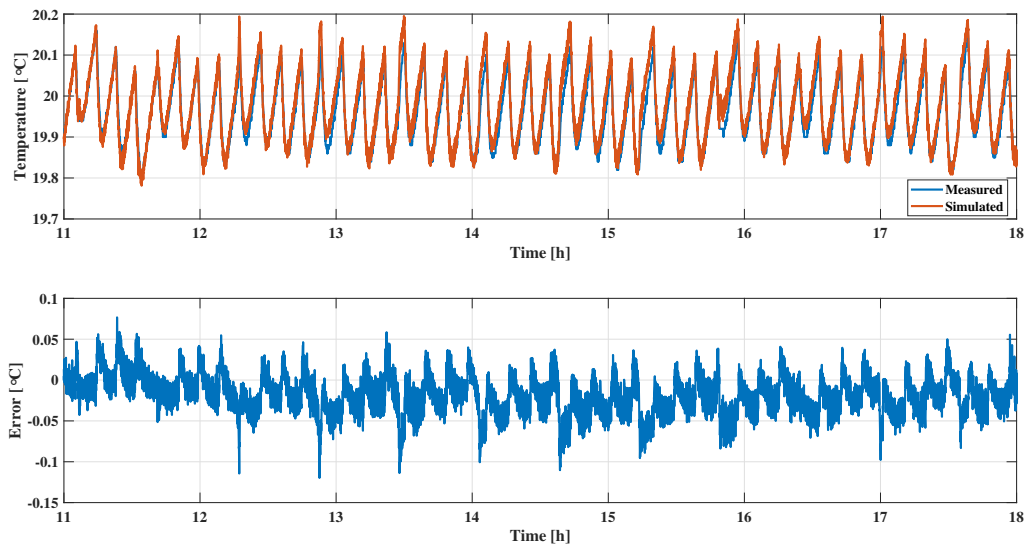
(a) NEDC test cycle
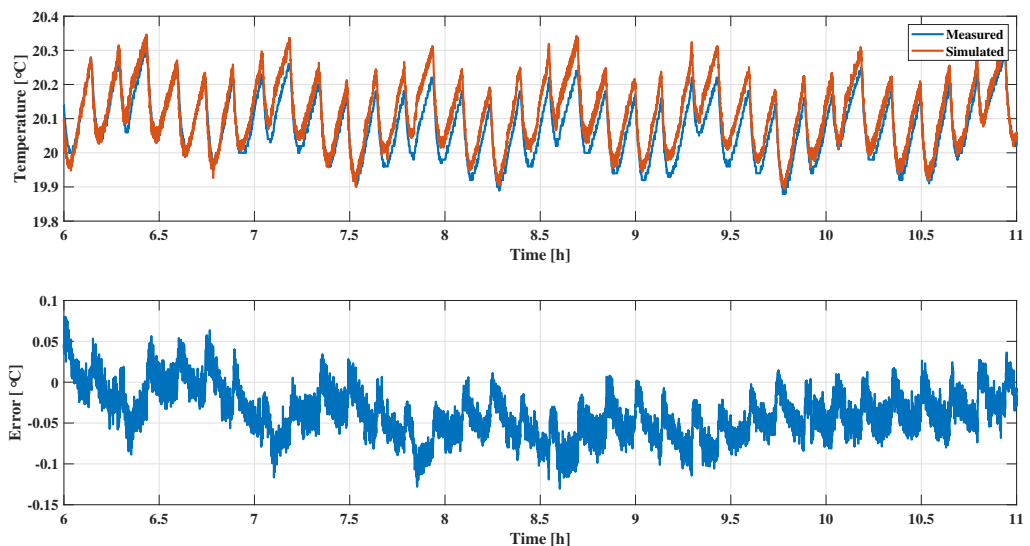


(b) WLTC test cycle

**Figure 4.48:** Electrical model performance. Magnified image

## 4.5 SOC estimation model results

In this section, two *SOC* estimation model performances based on the *EKF* and *UKF* will be discussed and its results are presented. The *SOC* estimation model is made according to the previous discussions made in section 3.7 and its model is represented as shown in figure 3.34. To verify the performance of the model WLTC current profile shown in figure 4.44(b) is fed to the cell model and *SOC* estimation model as discussed in an earlier section.

A wrong value of initial $SOC$ estimate is chosen in,

$$x_0 = \begin{bmatrix} 0 \\ 0 \\ 0 \\ \widehat{SOC_{init}} \end{bmatrix}$$

such that, to observe how good the estimation models can estimate $SOC$ or go back to the actual value of $SOC$ based on the voltage measurements. $\widehat{SOC_{init}}$ is varied from 0 to 0.95 with the steps of 0.05. Figure 4.49 shows the plot of maximum and RMSE error of $SOC$ estimates compared to the actual $SOC$ values.

Here we can easily notice that the maximum errors and RMSE is higher for $EKF-SOC$ estimation for $\widehat{SOC_{init}}$<0.25. This is due to the fact that there is higher non-linearity of the system, which $EKF$ is unable to linarize. Whereas the $EKF-SOC$ estimation performs well, and the maximum error and RMSE is well within 2% for $\widehat{SOC_{init}} > 0.25$. $UKF$ is designed for nonlinear systems and hence it is able to estimate the $SOC$ even when the $\widehat{SOC_{init}} = 0$ and as far away from the actual value of 1.

When $\widehat{SOC_{init}}$ is nearer to the actual value of 1, $EKF$ is having smaller errors than that of the $UKF$, but both the filters are having lesser than 1% error and hence using $UKF$ would be better in the $BMS$ instead of $EKF$ as it can estimate the $SOC$ irrespective of the initial guess of $\widehat{SOC_{init}}$.
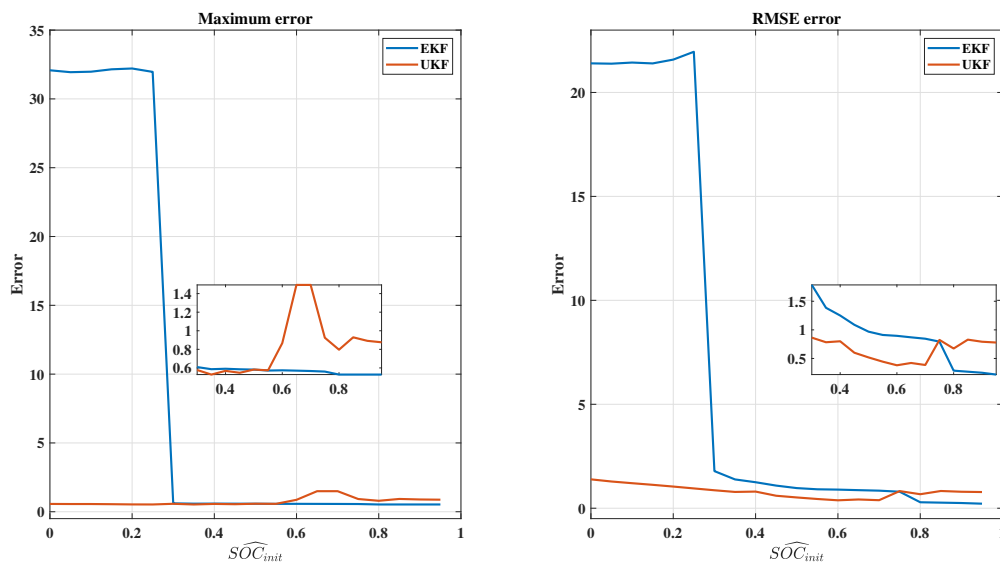


**Figure 4.49:** Plot of maximum and RMS error between the actual $SOC$ and estimated $SOC$ with respect to the different values of $\widehat{SOC_{init}}$

Both the $EKF$ and the $UKF$ is accurately estimating the $SOC$ and it is closely matching with the actual $SOC$ as shown in figure 4.50(a) at $\widehat{SOC_{init}} = 0.5$. One

other benefit of using $UKF$ is that it is fast in matching with the actual $SOC$ when compared to $EKF$ and it can be observed in high $SOC$ region, as shown in figure 4.50(b). Both the filters have higher errors at low $SOC$ region as it starts to approach 0% $SOC$.

SOC estimation model results $\widehat{SOC}_{init} = 0.5$
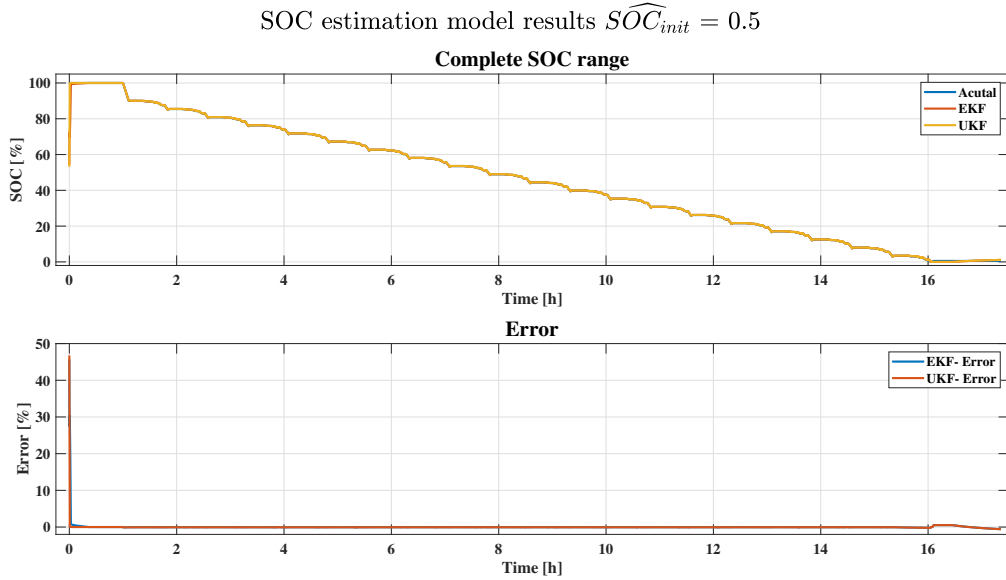


(a) Model results for the entire $SOC$ region.
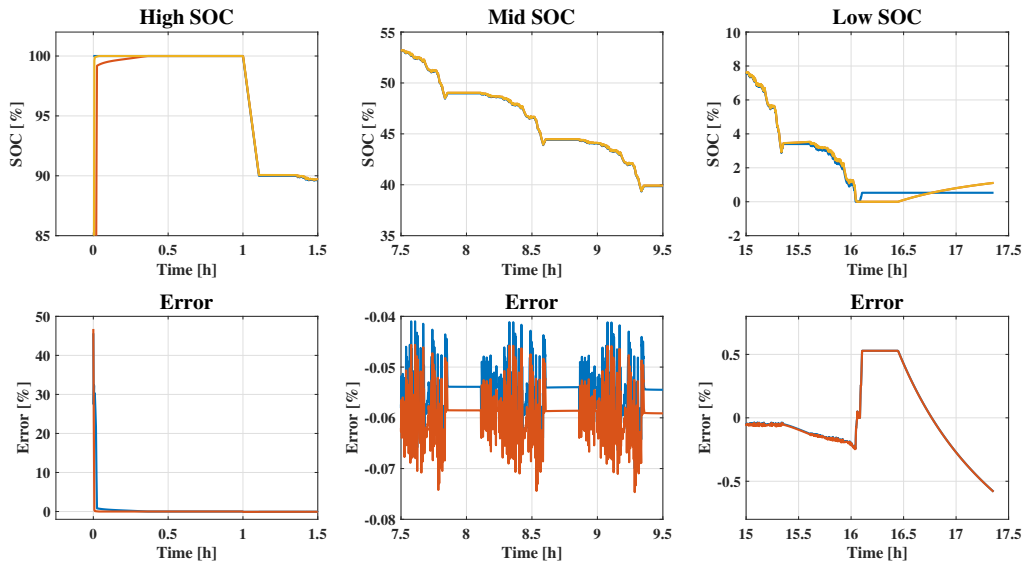


(b) Model results in different $SOC$ region.

**Figure 4.50:** $SOC$ estimation model results

# 5

# Discussion

In this section discussion on sustainability aspects, taken care in this thesis work will be done.

## 5.1 Results discussion

### Electrical characterisation

The equivalent circuit model using 3RC pair was selected to make the electrical model. The parameters were first extracted analytically according to [38], and then the extracted parameters were further optimised using the parameter estimation according to [39]. The RMSE error between the experiment and the simulation is reduced significantly after the optimisation step for the pulse discharge/charge tests as seen from tables 4.6 and 4.8.

From the results, it is evident that maximum errors are at high $SOC$ and at low $SOC$. Smaller current pulses can be chosen at high and low $SOC$ regions to lessen the errors. This increases the overall time of the test and increases the number of parameters to be optimised. To minimise further the error between the actual and estimated voltage for LFP cell, the relaxation time during the test can be increased for 2 hours as done in [39], but this would also increase the time of the test.

**Table 5.1:** Number of RC pairs used for different chemistries.

| Chemistry | RC pairs | Source |
|---|---|---|
| LCO/G | | |
| LMO/LTO | 2RC | [38] |
| NMO/LTO | | |
| NMO+LMO/G | | |
| LFP/G | 3RC | This study & [39] |

In table 5.1, the number of RC pairs used for electrical circuit models is shown. In [38], 2RC pairs were used as it was seen as sufficient and no major advantage to going for higher-order. But since LFP cells have higher hysteresis than the other

LIB[1] cells shown in the table, it has the slowest time constant it becomes important to represent it with an extra RC pair, hence in this study 3RC pairs are used. It is observed that in [39] for LFP cell, using 4RC was better than 3RC but due to computational cost 3RC was chosen in the end. So it is a trade-off between higher accuracy and computational cost. Higher-order RC networks influence the computational cost and are not suitable for embedded systems applications.

Even though analytically found parameters have a smaller error, further optimising it using parameter optimisation routine is giving much lesser errors. This step of optimising the parameters is beneficial in having a more robust electrical model since it helps to accurately 'mimic' the dynamic behaviour of the cell.

## Thermal Characterisation

A new simple and cost-effective methodology was proposed in this thesis to find specific heat capacity and thermal resistance of the cell. The methodology proposed can give both of these parameters in a single experiment having a smaller variation between different trials. The accuracy of the values obtained from the new methodology is unsure since it is yet to compare with the values got from a standard tests like from calorimeter. The value of specific heat capacity can vary due to both temperature and $SOC$, and these effects are not considered in this thesis.

In table 5.2, the specific heat capacity and thermal resistance found from different literature is compiled together. Even though the values do not have 'One to One 'comparison because of different size and capacity but have the same chemistry, the values found from the new methodology are in the same value-range as found from the different research works.

**Table 5.2:** Comparison of $C_{p_{cell}}$ and $R_{cell}$ of new methodology and with different literature for LFP chemistry.

| Chemistry | Format | $C_{p_{cell}}[\mathrm{Jkg^{-1}K^{-1}}]$ | k [$\mathrm{Wm^{-1}K}$] | $R_{cell}$ [K W$^{-1}$] | Source |
|---|---|---|---|---|---|
| LFP/G | Prismatic | $1035.67 \pm 10$ | $1.48 \pm 0.02$ | $0.79 \pm 0.1$ | This study |
| | | 1067 | 1.12 [2] | 0.88 | [59] [60] |
| | | $1087 \pm 29.35$ | x | x | [61] |
| | | 830 | x | 0.8 | [62] |

To compare the value of the thermal resistance found in the new methodology can be best done with that of the calorimetric test. Lumped thermal resistance through the thickness of the cell depends on the number of layers and thickness of the cathode, anode, separator and the metal casing, and thus it can vary between different cells. The calculated value of lumped thermal conductivity which includes the jelly role and metal casing from the data given in [60] is comparatively lower than the

---

[1]Lithium Ion Battery
[2]Calculated value from the literature

thermal conductivity found from the new methodology, but the thermal resistance is almost the same. This could be due to the thickness of the metal casing of both the cells. The thickness of the metal casing is not provided by the manufacturer of the cell used in this thesis. The cell used in [62] has double the mass and double the capacity when compared to the cell used in the thesis. But the cell dimensions are not mentioned, and therefore it is not possible to calculate the thermal conductivity in thru-plane. The thru plane conductivity was difficult to observe due to higher thermal conductivity due to the Aluminium casing, and hence the value is not available in [61].

The entropic coefficients were between $\pm 0.2 \text{mVK}^{-1}$ and it agrees with the range of entropic coefficients found in [59]. The trend of entropic coefficients is seen to be matching with that of [58]. The potentiometric test took around 200 hours, and the test was not repeated to check for consistency in the values due to time constraints. The other standard methods to find these coefficients is by the calorimetric method and the new method proposed by [29] which is simple and time-effective can be used.

## 5.2 Sustainability aspects

The fluctuation in fuel prices is a major problem for the emerging economies that import oil and whose economy is dependant on it. Using an electric vehicle instead of combustion vehicles would reduce the imports of oil, and this benefit is easily recognised. Even though the adaption of electric vehicles is met with uncertainty about the capital cost, availability of charging infrastructure, whether the sources of electricity generation are from renewable or from the coal power plant. But, optimism exists to overcome these issues in the near future. For adaption of electric vehicles from the consumer point of view, the vehicle performance must be as good as a combustion vehicle, if not better. Also, the price of the EV should be comparable to a combustion vehicle. To achieve this the development of EV's must be done at a much faster pace, and development cost must be lower. The cell model developed in this thesis helps the developer to take important decision for choosing various electrical loads in the vehicle, this helps in saving in development time and money. The model can also be used in the BMS application. Since the testing methods are simple and cost-effective it will not change the initial capital cost for setting up the lab and can be done with existing lab infrastructure.

In general, society resists change. To have good acceptance for adaption of EVs or even electric aeroplanes, it should overcome a few vital concerns. From a customer point of view, due to the large gap in the energy density of petrol/diesel to that of batteries range of the vehicle is a major concern. With present cell technologies, electric aeroplanes are still not commercialised. Another Major scepticism is with safety. After the infamous thermal runaway incident of Samsung phone Galaxy Note 7, the company had to recall the phones, and it gathered major media coverage and did a huge brand damage [63]. Recalling the product raises the question about its reliability. Being safe and reliable is vital for faster adaptation of EV's. The cell model developed can be modified and can be used to know how

good the cell behaves for different drive cycles and observation can be made regarding the temperature rise of the cell. Such models help in developing better thermal management strategies to keep the battery within optimum operating temperatures.

Even though there are no negative effects on the environment from this thesis, but its indirect benefits are discussed in the previous discussion. Mining for cobalt and political conditions in Democratic Republic of Congo (DRC) is a major concern ethically, economically, socially and environmentally [64]. Hence, this is one of the reasons for choosing LFP chemistry for this study to avoid cathode material with Cobalt. Faster adaptations of the electric vehicle and social change will lead to a positive impact on the environment by reducing pollution in noise, air etc.

# 6

# Conclusion

In this work, the goal was to make the electro-thermal model of the LFP prismatic cell. To develop the electrical model, EECM was made and pulse discharge/charge tests were done on the cell at four different temperatures. The parameters were initially extracted analytically for the model and later was further optimised using a parameter estimation routine. For the equivalent circuit model, 3RC pairs were used as they performed better than the lower order RC pairs. The error between the actual measured voltage and model voltage is found to be reduced by around 4 times at room temperature and having an optimisation routine is beneficial to make the model more accurate.

The three parameters important for developing thermal model are specific heat capacity, thermal resistance and entropic coefficients. In this thesis, a new methodology without using a calorimeter is proposed which uses a simple setup, and the test was conducted using many trials. It is observed that the variation of these two parameters are small and does not vary with respect to power, hence the new methodology can extract both of these two parameters in a single experiment. The specific heat capacity $C_{p_{cell}}$ is found to be $1035.67\,\mathrm{Jkg^{-1}K^{-1}}$ and the thru-plane thermal resistance is found to be $0.79\,\mathrm{KW^{-1}}$. The heat generated inside the cell is due to both irreversible losses and reversible losses. The parameters from the EECM model were used to calculate the irreversible losses and to calculate the reversible losses, entropic coefficients were extracted from potentiometric tests. Finally, a first-order thermal model using equivalent circuit analogy is made and verified separately. The model is found to be closely matching with the simple power pulse test where the temperature of the cell is increased and decreased.

The cell model was made after electrical and thermal characterisation and it was verified with the help of WLTC and NEDC drive cycles. The model was first calibrated using the experimental data of NEDC and later again verified for the WLTC drive cycle. The model was able to predict both surface temperature and terminal voltage very close to that of the experiment. Hence, the cell model can be used for load analysis and simulation purposes. To demonstrate one other application of the model in Battery management applications, a *SOC* estimation model was made using the Extended Kalman Filter and Unscented Kalman Filter.

Since all the tests done for characterisation uses simple setups and equipment that are easily found in the standard battery labs, it is possible to develop the model without additional investment on specialised equipment. Hence, it is cost-effective.

## 6.1 Future work

There are several aspects in which the modelling can be improved, and some are listed as follows:

- For even better accuracy, a shorter pulse width at high and low $SOC$ regions can be used during the pulse charge/discharge test to have more parameters in these regions and thus accurately estimate the voltage transient. Therefore having a higher fidelity model.

- LFP cell exhibits higher hysteresis compared to other cell chemistries, hence having a dedicated hysteresis model and incorporating it with the EECM can further enhance the accuracy of the electrical model.

- The new methodology proposed in the thesis is yet to be verified with the standard methods for its accuracy. The methodology can be further improved to accurately extract the two parameters. There are two main assumptions made in the new methodology and it is interesting to know how these two assumptions affect the parameter extraction.

- Since, the new methodology was only implemented on an LFP prismatic cell, it is interesting to check if the new method can extract parameters for different chemistries and different formats. If the results match close to that of the standard method, then it is easy to conclude that it could extract both the parameters effectively irrespective of chemistries and formats.

- The effect of temperature, $SOC$ and ageing on the thermal properties are not studied in this thesis, hence it would be interesting to observe these effects. The model is developed in the Matlab environment and hence it would be beneficial to understand the difficulties of implementing it on hardware. This information can help in optimising the model for the hardware application.

# Bibliography

[1] "Co2 emissions from cars: facts and figures (infographics)," European Parliament, Apr. 2019. [Online]. Available: https://www.europarl.europa.eu/news/en/headlines/priorities/climate-change/20180305STO99003/reducing-carbon-emissions-eu-targets-and-measures

[2] "Reducing co2 emissions from heavy-duty vehicles," European Parliament, 2019. [Online]. Available: https://ec.europa.eu/clima/policies/transport/vehicles/heavy_en

[3] E. Union, "setting co 2 emission performance standards for new heavy-duty vehicles and amending regulations (ec) no 595/2009 and (eu) 2018/956 of the european parliament and of the council and council directive 96/53/ec," Jun. 2019. [Online]. Available: https://eur-lex.europa.eu/eli/reg/2019/1242/oj

[4] "Reducing carbon emissions: Eu targets and measures," European Parliament, Apr. 2019. [Online]. Available: https://www.europarl.europa.eu/news/en/headlines/society/20190313STO31218/co2-emissions-from-cars-facts-and-figures-infographics

[5] D. V. Pelegov and J. Pontes, "Main drivers of battery industry changes: Electric vehicles—a market overview," *Batteries*, vol. 4, no. 4, p. 65, Dec. 2018.

[6] M. Ceraolo, T. Huria, G. Pede, and F. Vellucci, "Lithium-ion starting-lighting-ignition batteries: Examining the feasibility," in *2011 IEEE Vehicle Power and Propulsion Conference*, Sep. 2011, pp. 1–6.

[7] M. M. Thackeray, C. Wolverton, and E. D. Isaacs, "Electrical energy storage for transportation—approaching the limits of, and going beyond, lithium-ion batteries," *Energy & Environmental Science*, vol. 5, no. 7, pp. 7854–7863, 2012.

[8] L. H. Saw, Y. Ye, and A. A. Tay, "Integration issues of lithium-ion battery into electric vehicles battery pack," *Journal of Cleaner Production*, vol. 113, pp. 1032–1045, 2016.

[9] Z. Rao, S. Wang, and G. Zhang, "Simulation and experiment of thermal energy management with phase change material for ageing lifepo4 power battery," *Energy Conversion and Management*, vol. 52, no. 12, pp. 3408–3414, 2011.

[10] X. Lai, Y. Zheng, and T. Sun, "A comparative study of different equivalent circuit models for estimating state-of-charge of lithium-ion batteries," *Electrochimica Acta*, vol. 259, pp. 566–577, 2018.

[11] "Power electronics control design with simulink," Mathworks. [Online]. Available: https://www.mathworks.com/solutions/power-electronics-control/battery-models.html

[12] D. W. Dees, V. S. Battaglia, and A. Bélanger, "Electrochemical modeling of lithium polymer batteries," *Journal of power sources*, vol. 110, no. 2, pp. 310–320, 2002.

[13] J. Li, Q. Lai, L. Wang, C. Lyu, and H. Wang, "A method for soc estimation based on simplified mechanistic model for lifepo4 battery," *Energy*, vol. 114, pp. 1266–1276, 2016.

[14] C. Hametner and S. Jakubek, "State of charge estimation for lithium ion cells: Design of experiments, nonlinear identification and fuzzy observer design," *Journal of Power Sources*, vol. 238, pp. 413–421, 2013.

[15] H. Chaoui, C. C. Ibe-Ekeocha, A. El Mejdoubi, A. Oukaour, H. Gualous, and N. Omar, "State of charge estimation of lifepo 4 batteries with temperature variations using neural networks," in *2016 IEEE 25th International Symposium on Industrial Electronics (ISIE)*. IEEE, 2016, pp. 286–291.

[16] S. Nejad, D. Gladwin, and D. Stone, "A systematic review of lumped-parameter equivalent circuit models for real-time estimation of lithium-ion battery states," *Journal of Power Sources*, vol. 316, pp. 183–196, 2016.

[17] T. Bruen and J. Marco, "Modelling and experimental evaluation of parallel connected lithium ion cells for an electric vehicle battery system," *Journal of Power Sources*, vol. 310, pp. 91–101, 2016.

[18] S. Barsali and M. Ceraolo, "Dynamical models of lead-acid batteries: Implementation issues," *IEEE Transactions on energy conversion*, vol. 17, no. 1, pp. 16–23, 2002.

[19] M. Ceraolo, "New dynamical models of lead-acid batteries," *IEEE transactions on Power Systems*, vol. 15, no. 4, pp. 1184–1190, 2000.

[20] R. A. Jackey, "A simple, effective lead-acid battery modeling process for electrical system component selection," *SAE Transactions*, pp. 219–227, 2007.

[21] J. Chiew, C. Chin, W. Toh, Z. Gao, J. Jia, and C. Zhang, "A pseudo three-dimensional electrochemical-thermal model of a cylindrical lifepo4/graphite battery," *Applied Thermal Engineering*, vol. 147, pp. 450–463, 2019.

[22] M. Mastali, E. Foreman, A. Modjtahedi, E. Samadani, A. Amirfazli, S. Farhad, R. A. Fraser, and M. Fowler, "Electrochemical-thermal modeling and experimental validation of commercial graphite/lifepo4 pouch lithium-ion batteries," *International Journal of Thermal Sciences*, vol. 129, pp. 218–230, 2018.

[23] R. Benger, H. Wenzl, H.-P. Beck, M. Jiang, D. Ohms, and G. Schaedlich, "Electrochemical and thermal modeling of lithium-ion cells for use in hev or ev application," *World Electric Vehicle Journal*, vol. 3, no. 2, pp. 342–351, 2009.

[24] G.-H. Kim, A. Pesaran, and R. Spotnitz, "A three-dimensional thermal abuse model for lithium-ion cells," *Journal of Power Sources*, vol. 170, no. 2, pp. 476–489, 2007.

[25] P. J. Dunning, T. Mackin, R. Rozsnyo, and J. Stoudmann, "Heat generation modeling of a lithium battery: from the cell, to the pack on comsol multiphysics."

[26] M. Debert, G. Colin, G. Bloch, and Y. Chamaillard, "An observer looks at the cell temperature in automotive battery packs," *Control Engineering Practice*, vol. 21, no. 8, pp. 1035–1042, 2013.

[27] J. Sun, G. Wei, L. Pei, R. Lu, K. Song, C. Wu, and C. Zhu, "Online internal temperature estimation for lithium-ion batteries based on kalman filter," *Energies*, vol. 8, no. 5, pp. 4400–4415, 2015.

[28] T. S. Bryden, B. Dimitrov, G. Hilton, C. P. de León, P. Bugryniec, S. Brown, D. Cumming, and A. Cruden, "Methodology to determine the heat capacity of lithium-ion cells," *Journal of Power Sources*, vol. 395, pp. 369–378, 2018.

[29] Z. Geng, J. Groot, and T. Thiringer, "A time and cost effective method for entropic coefficient determination of a large commercial battery cell," *IEEE Transactions on Transportation Electrification*, pp. 1–1, 2020.

[30] W.-Y. Chang, "The state of charge estimating methods for battery: A review," *ISRN Applied Mathematics*, vol. 2013, 2013.

[31] A. Barai, W. D. Widanage, J. Marco, A. McGordon, and P. Jennings, "A study of the open circuit voltage characterization technique and hysteresis assessment of lithium-ion cells," *Journal of Power Sources*, vol. 295, pp. 99–107, 2015.

[32] M. A. Awadallah and B. Venkatesh, "Accuracy improvement of soc estimation in lithium-ion batteries," *Journal of Energy Storage*, vol. 6, pp. 95–104, 2016.

[33] A. A. Hussein *et al.*, "Kalman filters versus neural networks in battery state-of-charge estimation: A comparative study," *International Journal of Modern Nonlinear Theory and Application*, vol. 3, no. 05, p. 199, 2014.

[34] J. Lu, Z. Chen, Y. Yang, and M. Lv, "Online estimation of state of power for lithium-ion batteries in electric vehicles using genetic algorithm," *IEEE Access*, vol. 6, pp. 20 868–20 880, 2018.

[35] Y. Ma, P. Duan, Y. Sun, and H. Chen, "Equalization of lithium-ion battery pack based on fuzzy logic control in electric vehicle," *IEEE Transactions on Industrial Electronics*, vol. 65, no. 8, pp. 6762–6771, 2018.

[36] D. X. Yu and Y. X. Gao, "Soc estimation of lithium-ion battery based on kalman filter algorithm," in *Applied Mechanics and Materials*, vol. 347. Trans Tech Publ, 2013, pp. 1852–1855.

[37] Z. He, M. Gao, C. Wang, L. Wang, and Y. Liu, "Adaptive state of charge estimation for li-ion batteries based on an unscented kalman filter with an enhanced battery model," *Energies*, vol. 6, no. 8, pp. 4134–4151, 2013.

[38] S. Skoog, "Parameterization of equivalent circuit models for high power lithium-ion batteries in hev applications," in *2016 18th European Conference on Power Electronics and Applications (EPE'16 ECCE Europe)*. IEEE, 2016, pp. 1–10.

[39] T. Huria, M. Ceraolo, J. Gazzarri, and R. Jackey, "High fidelity electrical model with thermal dependence for characterization and simulation of high power lithium battery cells," in *2012 IEEE International Electric Vehicle Conference*. IEEE, 2012, pp. 1–8.

[40] H. Berg, *Batteries for electric vehicles: materials and electrochemistry*. Cambridge university press, 2015.

[41] M. E. vehicle team, "A guide to understanding battery specifications," Dec. 2008.

[42] M. Schwartz, "Deposition from aqueous solutions: an overview," *Handbook of Deposition Technologies for Films and Coatings—Science, Technology and Applications*, vol. 506, 1994.

[43] A. Dinger, R. Martin, X. Mosquet, M. Rabl, D. Rizoulis, M. Russo, and G. Sticher, "Batteries for electric cars: Challenges, opportunities, and the outlook to 2020," *The Boston Consulting Group*, vol. 7, p. 2017, 2010.

[44] C. T. Love, O. A. Baturina, and K. E. Swider-Lyons, "Observation of lithium dendrites at ambient temperature and below," *ECS Electrochemistry Letters*, vol. 4, no. 2, p. A24, 2015.

[45] D. Bernardi, E. Pawlikowski, and J. Newman, "A general energy balance for battery systems," *Journal of the electrochemical society*, vol. 132, no. 1, p. 5, 1985.

[46] E. Ramírez-Laboreo, C. Sagüés, and S. Llorente, "Thermal modeling, analysis and control using an electrical analogy," in *22nd Mediterranean Conference on Control and Automation.* IEEE, 2014, pp. 505–510.

[47] Mathworks, "Curve fitting toolbox." [Online]. Available: https://www.mathworks.com/products/optimization.html

[48] H. J. Motulsky and L. A. Ransnas, "Fitting curves to data using nonlinear regression: a practical and nonmathematical review," *The FASEB journal*, vol. 1, no. 5, pp. 365–374, 1987.

[49] T. Glad and L. Ljung, *Control theory.* CRC press, 2018.

[50] S. J. Julier and J. K. Uhlmann, "New extension of the kalman filter to nonlinear systems," in *Signal processing, sensor fusion, and target recognition VI*, vol. 3068. International Society for Optics and Photonics, 1997, pp. 182–193.

[51] E. A. Wan and R. Van Der Merwe, "The unscented kalman filter for nonlinear estimation," in *Proceedings of the IEEE 2000 Adaptive Systems for Signal Processing, Communications, and Control Symposium (Cat. No. 00EX373).* Ieee, 2000, pp. 153–158.

[52] L. Guzzella, A. Sciarretta *et al.*, *Vehicle propulsion systems.* Springer, 2007, vol. 1.

[53] M. Ceraolo, G. Lutzemberger, and T. Huria, "Experimentally-determined models for high-power lithium batteries," SAE Technical Paper, Tech. Rep., 2011.

[54] Mathworks, "Optimization toolbox." [Online]. Available: https://www.mathworks.com/products/optimization.html

[55] O. Almanza, M. Rodríguez-Pérez, and J. De Saja, "Measurement of the thermal diffusivity and specific heat capacity of polyethylene foams using the transient plane source technique," *Polymer international*, vol. 53, no. 12, pp. 2038–2044, 2004.

[56] "Second order overdamped equation," Aug. 2020. [Online]. Available: https://apmonitor.com/pdc/index.php/Main/SecondOrderSystems

[57] M. Tutuianu, A. Marotta, H. Steven, E. Ericsson, T. Haniu, N. Ichikawa, and H. Ishii, "Development of a world-wide worldwide harmonized light duty driving test cycle (wltc)," *Technical Report*, 2013.

[58] S. Bazinski and X. Wang, "The influence of cell temperature on the entropic coefficient of a lithium iron phosphate (lfp) pouch cell," *Journal of The Electrochemical Society*, vol. 161, no. 1, p. A168, 2013.

[59] C. Lin, S. Xu, Z. Li, B. Li, G. Chang, and J. Liu, "Thermal analysis of large-capacity lifepo4 power batteries for electric vehicles," *Journal of power sources*, vol. 294, pp. 633–642, 2015.

[60] H. Lundgren, P. Svens, H. Ekström, C. Tengstedt, J. Lindström, M. Behm, and G. Lindbergh, "Thermal management of large-format prismatic lithium-ion battery in phev application," *Journal of The Electrochemical Society*, vol. 163, no. 2, p. A309, 2015.

[61] A. Lidbeck and K. R. Syed, "Experimental characterization of li-ion battery cells for thermal management in heavy duty hybrid applications," *Gothonburg, Sweden*, 2017.

[62] N. Damay, C. Forgez, M.-P. Bichat, and G. Friedrich, "Thermal modeling of large prismatic lifepo4/graphite battery. coupled thermal and heat generation models for characterization and simulation," *Journal of Power Sources*, vol. 283, pp. 37–45, 2015.

[63] S. Kang, K. Shim, and J. Kim, "Social media posts on samsung galaxy note 7 explosion: A comparative analysis of crisis framing and sentiments in three nations," *Journal of International Crisis and Risk Communication Research*, vol. 2, no. 2, p. 4, 2019.

[64] J. Gordon, "Cobalt: the dark side of a clean future," Jun. 2019. [Online]. Available: https://www.raconteur.net/business-innovation/responsible-business-2019/cobalt-mining-human-rights

Bibliography

# A

# Appendix 1 - Vehicle parameters

The general vehicle parameters for the mid-sized Battery Electric vehicle is given in the table

Table A.1: Vehicle parameters of mid-sized Battery Electric Vehicle

| Parameters | Values |
|---|---|
| Drag coefficient, $C_d$ | 0.23[1] |
| Rolling resistance coefficient, $C_r$ | 0.01[1] |
| Front area, $A_f$ | 2.22 m² [1] |
| Mass of the vehicle including battery, $m_{veh}$ | 1726 kg |

---

[1]https://insideevs.com/news/406163/engineering-explained-how-efficient-tesla-is/